ADVANCED TIME-DOMAIN NUMERICAL METHODS FOR ELECTROMAGNETIC MODELING AND SIMULATION

by

Shunchuan Yang

Submitted in partial fulfilment of the requirements
for the degree of Doctor of Philosophy

at

Dalhousie University
Halifax, Nova Scotia
August 2015

Dedication

I dedicate this thesis to my parents, Heshou & Chuanbi, and my sister Shunlan, for their continuous support no matter where I am. Especially, I dedicate this thesis to my beloved wife Jin for her endless love and encouragement when I studied abroad.

Table of Contents

List of Tables

List of Figures

Abstract

In this thesis, systematic investigations on divergence property of the divergence preserved alternatively-direction-implicit finite-difference time-domain (ADI-FDTD) method and the meshless method are carried out.

It is found that divergence preserved ADI-FDTD method maintains the unconditional stability and the same numerical dispersion as that of the traditional ADI-FDTD method, while preserving electromagnetic divergence properties. To further improve its efficiency, an efficiency improved version is proposed. Theoretical proof of both the unconditional stability and the divergence property is provided. Almost 41.7% less count of floating-point operations than the original one is obtained.

Investigations on the meshless method lead to the following results.

(1) A meshless method for the wave equation is proposed to improve the efficiency based on the mathematical equivalence of the Maxwell's equations and wave equation. Since the proposed method only requires to solve electrical field, computational efficiency of the proposed method is largely improved.

(2) A divergence preserved meshless method based on the vector radial basis function (RBF) is proposed to solve the Maxwell's equations. The conventional meshless method using Gaussian RBF cannot preserve the divergence property of electric and magnetic fields. The proposed method is theoretically proven to be divergence free and will not introduce the artificial charges in its numerical solutions. Numerical results show that the proposed method can accurately model the charge distribution in the simulations.

(3) A stable meshless method based on QR-decomposition method is proposed to overcome the spatial stability issue of the conventional meshless method. The source of the spatial instability is removed from the Gaussian RBF through the QR-decomposition method. A new stable basis function, which share the same function space as that of the Gaussian RBF, is obtained.

(4) The relationship between the meshless method and the FDTD method is theoretically investigated in terms of numerical dispersion. When node distribution and field component location is the same as that of the FDTD method, numerical dispersion of the meshless method can become the same as that of the FDTD method. It implies that the meshless method is a general method which includes the FDTD method as its special case.

List of Abbreviations and Symbols Used

ADI	Alternatively-direction-implicit
ADI-FDTD	Alternatively-direction-implicit finite-difference time-domain
CEM	Computational electromagnetics
FEM	Finite element method
MOM	Method of moment
FD	Finite-difference
GUI	Graphical user interface
CFL	Courant-Friedrichs-Lewy
LOD	Locally-one-dimensional
SFDTD	Split finite-difference time-domain
CN	Crank Nicolson
RBF	Radial basis function
PML	Perfectly matched layer
RPIM	Radial point interpolation meshless
MQ	Multiquadric
PIM	Point interpolation method
PEC	Perfect electrical conductor
MHD	Magneto-hydrodynamics
PPW	Points per wavelength
NPE	Numerical phase error
ε	Material permittivity
μ	Material permeability
$\mathbf{E}$	Electrical field
$\mathbf{H}$	Magnetic field
Z_0	Impedance of free space
$\partial\zeta$	Differential operators in the ζ direction
Δt	Discretized time step
$\mathbf{P}$	Matrix of partial differential operators
$\mathbf{M}$	Matrix of partial differential operators
$\mathbf{V}$	Field vector

M	Pre-defined order of differential operator
α_m	Coefficient associated with M order differential operator
k_x	Spatial frequency along the x direction
k_y	Spatial frequency along the y direction
k_z	Spatial frequency along the z direction
Λ	Amplification matrix
$\det\{\mathbf{A}\}$	Determinant of matrix **A**
q	Electrical charge
∇_f	Delta operator
$r=\|\mathbf{R}-\mathbf{R}_i\|$	Euclidean distance between **R** and $\mathbf{R}_i$
$\rho(\mathbf{T})$	Spectral radius of **T**
∇	Differential operator
Δ	Laplace operator
B	Interpolation matrix
k_{num}	Numerical wave number
c	Speed of light in the continuous medium
$c_{num}=\omega/k_{num}$	Speed of numerical waves
ω	Angular frequency.

Acknowledgements

I would like to express my appreciation to my supervisor Dr. Zhizhang (David) Chen, who brought me into fascinating computational electromagnetic fields and guide me with continuous patience in my research. This thesis would not have been completed without his expert advice and unfailing patience.

I appreciate my co-supervisor Dr. Sergey Ponomarenko for his guidance and support for my PhD study.

I would also extend my special appreciation to Dr. Mohamed Bakr of McMaster University, who served as the external examiner of my thesis and gave valuable comments and suggestions for my thesis. I also wish to thank the rest of my thesis committee: Dr. Kamal EI-Sankary and Dr. William Philips, for their useful suggestions and comments for modification of this thesis.

I would express my special appreciation to Dr. Yiqiang Yu, who gave me the support and guidance in the last five years. Without his patient guidance, I cannot finish this thesis. I also want to thank my colleagues, Dr. Farid Jolani, Dr. Wei Fan and other group members for their kind help during my Ph. D study.

Finally, I am grateful to my friends in Halifax, for your help, understanding and encouragement during my stay in Halifax. I cannot list all your names here, but you are all in my mind.

Chapter 1 Introduction

1.1 Preface

This thesis mainly focuses on investigation of the properties of the divergence-preserved alternatively-direction-implicit finite-difference time-domain (ADI-FDTD) method and development of the meshless method for the computational electromagnetics (CEM). This chapter introduces the research background of the thesis, and then reviews the state-of-art of the FDTD methods and meshless methods. Research objectives, contributions, and organization of this thesis are also presented.

1.2 Research Background

There are two possible ways to seek solutions of mathematical models. One is the analytical approach, which is the most preferred if it is applicable and can be easily derived. We can then obtain analytical solutions which can be easily computed. However, they are only obtainable for problems of certain regular shapes with simple boundaries. In many situations, most of the analytical solutions are found with certain assumptions and simplifications of the practical problems [1] [2]. Therefore, analytical approach is limited to solving a few problems such as a dipole, a circular cavity and an infinite ground plane [3]. Another way to solve mathematic models is to resort to numerical methods with modern computer technologies to obtain approximate solutions. In a numerical method, an original continuous model is first discretized in space and/or time and then transformed into a discrete model of a finite matrix system. By solving the discrete system, numerical approximate solutions are then obtained. The most common seen numerical methods are finite-difference (FD) method, finite element method (FEM), and method of moment (MOM). There are at least two conditions required to ensure that the numerical results obtained are valid: (1) when all discretized parameters in both space and time domain approach to zero, approximate solutions converge; and (2) the conservation laws, which are governed by the original continuous models, are satisfied in the discrete model.

Nowadays, numerical methods have been widely developed in engineering, leading to different branches such as computational electromagnetics, computational chemistry and computational physics. Many numerical methods have been commercialized, resulting in

many software packages. Equipped with modern Graphical User Interface (GUI), they are used to solve many problems that were not solved before or to design engineering components and systems that are difficult to do before.

In computational electromagnetics (which is the scope of this thesis), the finite-difference time-domain (FDTD) method is very popular due to its simplicity, easy implementation and strong capability of handling complex materials. A newly developed method, named split-step Fourier method, become more and more popular in solving the nonlinear optics[4, 5]. It can keep the carrier frequency and is faster than the finite difference method. However, it is less accurate than the FD methods. In this thesis, the FDTD method is considered for the computational electromagnetics. For the FDTD method, maximum time step is constrained by the Courant-Friedrichs-Lewy (CFL) condition [6], which is related to the smallest cell size in a discretized spatial domain. As a result, when multi-scale structures or geometry fine devices are presented in a solution domain, discretized cell sizes are inevitable small to capture the geometry details, which in turn make time step very small. As a result, computational time may become prohibitively long. To overcome the problem, the unconditionally stable alternatively-direction-implicit (ADI) FDTD method was developed [7-10]. With implicit method, the time step can be independent of cell sizes. Therefore, an arbitrarily large time step can be used; the only constraint is modeling accuracy. With a relatively large time step, the simulation time can be greatly reduced and computational efficiency is significantly improved. Other forms of the unconditionally stable FDTD methods have also been developed in the past decades; they include the locally-one-dimensional (LOD) FDTD methods [11-13], the multi-stage split FDTD (SFDTD) [14, 15], the one-step leapfrog ADI-FDTD method [16] and Crank Nicolson (CN) FDTD methods [17-20].

In recent years, however, it was found that the most traditional unconditionally stable FDTD methods have divergence issues [21-23]. That means the conservation laws for electrical charges and magnetic fields are not satisfied. Artificial charges or non-existent magnetic charges may be present in computational solutions and even leads to failures of simulations [24]. For the applications like particle-in-cell (PIC) simulations, those unconditionally stable methods cannot obtain valid results [25]. To address the issue, in [25], a divergence preserved ADI-FDTD method is proposed. Besides its unconditional

stability, the divergence properties of the Maxwell's equations are also satisfied. In [26], another divergence preserved LOD-FDTD method is proposed based on the fundamental formulations of the unconditionally implicit FDTD methods.

The above-mentioned FDTD methods are mesh- or grid-based because certain types of geometry elements, such as triangles in two dimension domains, tetrahedrons in three dimensions, are used to discretize original continuous problem domains. For these mesh-based methods, re-mesh has to be applied when structures or devices are partially modified or changed; connection information among elements, such as edge length, face area and volume of elements, is required to solve these problems. It needs to be updated during the re-meshing process. Such a process is quite time-consuming and may even take more time than that of a solution process.

To mitigate the above problem, meshless methods are introduced. In the conventional non-meshless grid-based method, in a discrete element, edges of spatial elements intersect and the intersection becomes a spatial node. When the edges, which connect two spatial nodes in an element, are removed, the nodes are left, forming a discrete space of nodes representing the solution domain. If the fields are solved in respect to those nodes, we obtain the so-called meshless methods. Since they are node based meshless methods can easily be self-adapted and geometrically conformal, only node location information is required. Various meshless methods have been proposed in recent years [27-32]. However, most of them use Gaussian radial basis function (RBF) and their solutions are found not meeting the conservation law and not divergence free in charge free regions [33]. In frequency domain, it is presented as several zero eigenvalues. To resolve the issue, in [34], a matrix-valued, or named as the vector-valued, RBF, which is theoretical divergence free, is proposed. It has been extensively investigated in [35]. In addition, as meshless methods are based on interpolation methods, inversion of interpolation matrix is inevitable. Various reports show that such inversion is problematic because the interpolation matrix may be severely ill-conditioned [33, 36-38]. Based on the interpolation theory, we can obtain accurate results when we choose extremely small shape parameters or employ more nodes in the support domain [38]. However, when the shape parameter, which controls the decay rate of Gaussian RBF, becomes extremely small or the number of scattering nodes in the support domain is large, the condition number of the interpolation matrix may become

extremely large, which leads to failure of matrix inversion. Therefore, we have to make a tradeoff between accuracy and the conditional number of the interpolation matrix or to find the optimal value for the shape parameter. There are several methods proposed to search such an optimal trade-off value [39]. Unfortunately, those optimal values are usually case dependent and we have to repeat such process even when we modify or change models or structures partially. In [38], a stable meshless method based on the QR decomposition method is proposed. When the shape parameter is extremely small, it is still able to get accurate results. Therefore, highly accurate solutions at the machine precision can be obtained.

1.3 Objectives

The goal of this thesis is to solve the above-mentioned problems present in the divergence preserved ADI-FDTD method and the meshless method. More specifically, the objectives are

1) to analytically verify the stability, numerical dispersion, and divergence properties of the divergence preserved ADI-FDTD method and to develop a technique to improve its computational efficiency;
2) to improve the computational efficiency by developing a new meshless method for solving electromagnetic vector wave equation;
3) to develop a new meshless method for the electromagnetic problems, which preserves the divergence properties of the electrical and magnetic fields;
4) to solve the ill-conditioning problems and the stability problems in the meshless method when the shape parameter is extremely small;
5) to study the relationship of the meshless method and the FDTD method.

1.4 Contributions of this Thesis

This thesis explores the divergence properties and computational efficiency of the unconditionally stable ADI-FDTD method and the meshless methods. The detailed implementation of the divergence-preserved ADI-FDTD method and its efficiency improved counterpart is systematically investigated. Theoretical proofs of its divergence properties are also provided. To improve the efficiency of the meshless for the Maxwell's

equations, a meshless method for the wave equation is proposed and applied to solving the resonant problems. Detailed studies is made to assess the improvement of the efficiency compared with that of the conventional meshless method for Maxwell's equations. A vector-based meshless method based on the vector RBF is then proposed to resolve the divergence issue. Detailed properties of the vector RBF is also addressed. Then, a stable meshless method based on the QR-decomposition method is proposed to solve the ill-condition problem in the meshless method. Finally, the relationship between the meshless method and the FDTD method is theoretically investigated.

In summary, the original contributions of this thesis are as follows:

1) Theoretical study on the divergence-preserved ADI-FDTD method is performed and it shows that the method is unconditionally stable and shares the same numerical dispersion of the ADI-FDTD method, the LOD-FDTD method, and the leapfrog ADI-FDTD method. Based on the fundamental formulations, an efficiency-improved divergence preserved ADI-FDTD method is proposed to enhance the performance in terms of the computational efficiency. Analytical and numerical results demonstrate that the proposed method preserves the divergence properties.

2) A new meshless method for the wave equation based on the local RBF is proposed to improve the efficiency of the meshless method for solving Maxwell's equations. With the proposed method, only one set of unknowns, either electrical fields or magnetic fields, is required. Therefore, compared with the conventional meshless method, which needs to solve the electrical and magnetic fields, simultaneously, this method can improve computational efficiency and reduce memory consumption.

3) Since the conventional meshless method based on the local Gaussian RBF is not divergence free, a new vector-based meshless method, which is theoretically divergence free, is proposed to solve Maxwell's equations and the wave equation. Detailed properties of the proposed method are investigated.

4) The reason for the ill-conditioning problem in the meshless method is studied. It is found that all the elements of the interpolation matrix approach one when the shape parameter is extremely small. It implies that all columns or rows become linearly dependent on each other. The QR-decomposition method is applied in this thesis and the terms of the shape parameter are analytically separated from the Gaussian RBF and a new

stable basis function is formed. Its stability is also verified by the numerical results.

5) The study on the relationship between the meshless method and the conventional FDTD method is conducted. It is found that when the node distribution and field component location of the meshless method is the same as that of the FDTD method, meshless method becomes the FDTD method. In other words, the FDTD method is a specific case of the meshless method. This means that the meshless method is a general method which contains the traditional FDTD method.

We have published our above original work in [40-47].

1.5 Organization of this Thesis

Since most of our original work has been published in the recent years, remaining part of this thesis will be mainly composed of the papers we published. This is in accordance with the Dalhousie Ph. D. thesis requirements.

Chapter 2 is basically our paper [40, 41]. There, a divergence preserved ADI-FDTD method is introduced to solve the Maxwell's equations. Its detailed implementation, theoretical proof of stability and dispersion properties is presented. In addition, an efficiency improved counterpart is also shown and its divergence properties are theoretically proved.

Chapter 3 is based on our paper [42]. There, a new meshless method for the wave equation is proposed. Its stability condition is also shown. The conformal ability and capability of handling multi-scale structures and efficiency are validated through numerical examples.

Chapter 4 is based on our paper [44]. There, the properties of a vector RBF are systematically analyzed. Based on this vector RBF, the meshless method is then applied to solving the Maxwell's equations and wave equation in the time domain. The divergence properties and accuracy are verified through numerical examples.

Chapter 5 is based on our paper [47]. There, in order to mitigate the ill-condition problem upon the interpolation matrix in the meshless method, QR decomposition method is proposed to separate the shape parameter from the Gaussian function and a stable meshless method is developed.

Chapter 6 is based on our paper [45]. There, the relationship between the meshless

method based on local Gaussian RBF and the FDTD method is explored in terms of their numerical dispersions. Theoretical analysis is performed on the numerical relationship of the two methods and conclusions are made about the two methods.

In chapter 7, conclusions are drawn and future work is presented.

Chapter 2 The Divergence-Preserved ADI-FDTD Method

This chapter is mainly based on our two published paper [40, 41]. One is Shunchuan Yang, Zhizhang (David) Chen, Yiqiang Yu, and Sergey Ponomarenko, "Efficient implementation of the divergence-preserved ADI-FDTD method," published in IEEE Antennas and Wireless Propagation Letters, vol. 11, pp. 1560-1563, 2012. Another is Shunchuan Yang, Zhizhang (David) Chen, Yiqiang Yu, and Sergey Ponomarenko, "On the divergence properties of the new efficiency-improved divergence preserved ADI-FDTD method," published in IEEE International Microwave Symposium, 2013, pp. 1-3.

2.1 Study on the Divergence-preserved ADI-FDTD Method

2.1.1 Abstract

The conventional ADI-FDTD method, although unconditionally stable, may not be divergence-free in a source-free region. In this section, a divergence-preserved ADI-FDTD method is presented. Its time-marching formulations are derived and analytical analysis of the stability is shown. It is found that the proposed ADI-FDTD method still retains the unconditional stability and its numerical dispersion is the same as the conventional ADI-FDTD method and the LOD-FDTD developed so far. However, like the conventional FDTD method, it is divergence-free in a source-free region; and unlike other unconditionally stable methods which do not preserve the divergence properties, it has no spurious charges introduced into numerical grids. Numerical results are presented to verify the claims and compared with the conventional FDTD method and the conventional ADI-FDTD methods.

2.1.2 Introduction

The FDTD method is widely applied in electromagnetic modeling due to its easy implementation and strong handling capability of complex materials [6]. However, to achieve convergence and obtain accurate results, the CFL stability condition that limits time step must be satisfied in practical simulations. As a result, computational time can be prohibitively high for modeling electrically fine and multi-scale structures. Fortunately, unconditionally stable FDTD methods, such as the ADI-FDTD method [10], the LOD-FDTD method [48] and the one-step leapfrog ADI-FDTD method [16], have been

developed to overcome the CFL condition; thus a large time step may be taken, leaving the only constraint of the numerical methods to be just modeling accuracy. However, recent research indicated that these unconditionally stable methods are not divergence-free in a source-free region [22]. That is, nonphysical spurious charges are introduced by these numerical methods, leading to nonphysical divergence accumulation that may cause eventual simulation failures [49]. Specifically, divergence property of the conventional ADI-FDTD method was investigated in [21] and it was found not divergence-free like the FDTD method. The newly proposed one-step leapfrog ADI-FDTD method was also studied and found not to be divergence-free either [22].

To overcome the above problem, a new divergence preserved ADI-FDTD method was proposed and the related theoretical work was presented in [25]. In addition, the perfectly matched layer (PML) was introduced into the newly developed two-dimensional divergence preserved ADI-FDTD method in [50].

In this section, detailed formulations for advancing fields, rigorous proof of the stability, and analysis of numerical dispersion are presented. First, the generalized formulations of the divergence preserved ADI-FDTD method are derived. Then, proof of stability and analysis of numerical dispersion are presented. Finally, the divergence-free property and unconditional stability with numerical examples are verified.

2.1.3 Detailed Formulations

In this section, formulations of the divergence preserved ADI-FDTD method are developed in detail.

For simplicity without losing generality, consider a linear, lossless, isotropic and non-dispersive medium with permittivity ε and permeability μ. The time-dependent Maxwell's curl equations can then be rewritten in the following form [25]:

$$\frac{1}{c}\frac{\partial \mathbf{E}}{\partial t} = \nabla \times (Z_o \mathbf{H}), \tag{2.1a}$$

$$\frac{\partial (Z_o \mathbf{H})}{\partial t} = -c\nabla \times \mathbf{E}, \tag{2.1b}$$

where $\mathbf{E} = \left[E_x \; E_y \; E_z \right]^T$, $\mathbf{H} = \left[H_x \; H_y \; H_z \right]^T$, $Z_0 = \sqrt{\mu / \varepsilon}$.

Two matrices of partial differential operators, **P** and **M,** are introduced to define the curl operation so that the Maxwell equations can be simply written as:

$$\frac{\partial \mathbf{V}}{\partial t} = c\left(\mathbf{P}+\mathbf{M}\right)\cdot \mathbf{V}, \tag{2.2}$$

where $\mathbf{V}=\left[E_x, E_y, E_z, Z_0 H_x, Z_0 H_y, Z_0 H_z\right]^T$,

$$\mathbf{P} = \begin{bmatrix} 0 & 0 & 0 & 0 & 0 & \frac{\partial}{\partial y} \\ 0 & 0 & 0 & \frac{\partial}{\partial z} & 0 & 0 \\ 0 & 0 & 0 & 0 & \frac{\partial}{\partial x} & 0 \\ 0 & \frac{\partial}{\partial z} & 0 & 0 & 0 & 0 \\ 0 & 0 & \frac{\partial}{\partial x} & 0 & 0 & 0 \\ \frac{\partial}{\partial y} & 0 & 0 & 0 & 0 & 0 \end{bmatrix} \tag{2.3a}$$

and

$$\mathbf{M} = \begin{bmatrix} 0 & 0 & 0 & 0 & -\frac{\partial}{\partial z} & 0 \\ 0 & 0 & 0 & 0 & 0 & -\frac{\partial}{\partial x} \\ 0 & 0 & 0 & -\frac{\partial}{\partial y} & 0 & 0 \\ 0 & 0 & -\frac{\partial}{\partial y} & 0 & 0 & 0 \\ -\frac{\partial}{\partial z} & 0 & 0 & 0 & 0 & 0 \\ 0 & -\frac{\partial}{\partial x} & 0 & 0 & 0 & 0 \end{bmatrix}. \tag{2.3b}$$

Note that $\mathbf{P}^{\mathrm{T}} = \mathbf{P}$, $\mathbf{M}^{\mathrm{T}} = \mathbf{M}$ and $\mathbf{PM} \neq \mathbf{MP}$.

The exact solution to (2.2) can be obtained as

$$\mathbf{V}^{n+1} = e^{c(\mathbf{P}+\mathbf{M})\Delta t}\cdot \mathbf{V}^{n}. \tag{2.4}$$

Here the superscript n is added; it denotes the field value at $t = n\Delta t$. Δt is the time step selected by a user.

The following approximation is now applied to the matrix exponential:

$$e^{c(\mathbf{P}+\mathbf{M})\Delta t} \approx e^{\frac{c\Delta t}{2}\mathbf{M}} e^{\frac{c\Delta t}{2}\mathbf{P}} e^{\frac{c\Delta t}{2}\mathbf{P}} e^{\frac{c\Delta t}{2}\mathbf{M}}. \tag{2.5}$$

By applying Taylor series to the first and third factors and Padé approximation [51] to the second and fourth factors, (2.5) can be rewritten as

$$e^{c(\mathbf{P}+\mathbf{M})\Delta t} \approx \left(\mathbf{I}+\frac{c\Delta t}{2}\mathbf{M}\right)\left(\mathbf{I}-\frac{c\Delta t}{2}\mathbf{P}\right)^{-1}\left(\mathbf{I}+\frac{c\Delta t}{2}\mathbf{P}\right)\left(\mathbf{I}-\frac{c\Delta t}{2}\mathbf{M}\right)^{-1}. \tag{2.6}$$

With (2.6), the approximate solution to (2.2) can be obtained as

$$\left(\mathbf{I}-\frac{c\Delta t}{2}\mathbf{P}\right)\left(\mathbf{I}+\frac{c\Delta t}{2}\mathbf{M}\right)^{-1}\mathbf{V}^{n+1} \approx \left(\mathbf{I}+\frac{c\Delta t}{2}\mathbf{P}\right)\left(\mathbf{I}-\frac{c\Delta t}{2}\mathbf{M}\right)^{-1}\mathbf{V}^{n}. \tag{2.7}$$

Eq. (2.7) is the divergence preserved ADI-FDTD method which turns out to be exactly the same as that presented in [25]. Its divergence-preserved property has been proven analytically in [25]. Note that in deriving the divergence preserved ADI-FDTD method, two approximations of (2.5) and (2.6) are taken; this is not explicitly indicated in [25].

By replacing the differential operators, $\partial\zeta$ in (2.7) (ζ=x, y, or z), with their corresponding central finite difference counterparts, the time marching divergence-preserved ADI-FDTD formulation is obtained as described below.

With Strang splitting, (2.7) can be broken up into two updating equations and each of them can be solved separately. The resulting time-marching equations are obtained with the introduction of intermediate term $\mathbf{V}^{n+1/2}$:

$$\mathbf{V}^{n+1/2} = \left(\mathbf{I}+\frac{c\Delta t}{2}\mathbf{P}\right)\left(\mathbf{I}-\frac{c\Delta t}{2}\mathbf{M}\right)^{-1}\mathbf{V}^{n}, \tag{2.8a}$$

$$\mathbf{V}^{n+1} = \left(\mathbf{I}+\frac{c\Delta t}{2}\mathbf{M}\right)\left(\mathbf{I}-\frac{c\Delta t}{2}\mathbf{P}\right)^{-1}\mathbf{V}^{n+1/2}. \tag{2.8b}$$

To facilitate operation of the inverse of the partial differential operators in (2.8), we introduce another intermediate term $\mathbf{Q}$, where $\mathbf{Q}=\left[Q_{ex},Q_{ey},Q_{ez},Q_{hx},Q_{hy},Q_{hz}\right]^T$. Q_{ex}, Q_{ey} and Q_{ez}

are related to electrical components and Q_{hx}, Q_{hy} and Q_{hz} are related to magnetic fields. The field location of **Q** is defined on the Yee's cell and have the same field distribution of **V**. It leads to the divergence-preserved ADI-FDTD formulations:

For the first sub-step:

$$\left(\mathbf{I} - \frac{c\Delta t}{2}\mathbf{M}\right)\mathbf{Q}^{n+1/2} = \mathbf{V}^{n} \tag{2.9a}$$

$$\mathbf{V}^{n+1/2} = \left(\mathbf{I} + \frac{c\Delta t}{2}\mathbf{P}\right)\mathbf{Q}^{n+1/2}. \tag{2.9b}$$

For the second sub-step:

$$\left(\mathbf{I} - \frac{c\Delta t}{2}\mathbf{P}\right)\mathbf{Q}^{n+1} = \mathbf{V}^{n+1/2} \tag{2.10a}$$

$$\mathbf{V}^{n+1} = \left(\mathbf{I} + \frac{c\Delta t}{2}\mathbf{M}\right)\mathbf{Q}^{n+1} \tag{2.10b}$$

More specifically, let's take the *x*-directed field components as an example.

For the first sub-step, from (2.9a), we have:

$$Q_{ex}^{n+1/2} = E_x^n - \frac{c\Delta t}{2}\partial z Q_{hy}^{n+1/2}, \tag{2.11a}$$

$$Q_{hx}^{n+1/2} = \mathrm{Z}_0 H_x^n - \frac{c\Delta t}{2}\partial y Q_{ez}^{n+1/2}. \tag{2.11b}$$

On substitute (2.3) into (2.9b), we have the following updating equations:

$$E_x^{n+1/2} = Q_{ex}^{n+1/2} + \frac{c\Delta t}{2}\partial y Q_{hz}^{n+1/2}, \tag{2.12a}$$

$$H_x^{n+1/2} = \frac{1}{\mathrm{Z}_0}Q_{hx}^{n+1/2} + \frac{c\Delta t}{2\mathrm{Z}_0}\partial z Q_{ey}^{n+1/2}. \tag{2.12b}$$

Similarly, for the second sub-step,

$$Q_{ex}^{n+1} = E_x^{n+1/2} + \frac{c\Delta t}{2}\partial y Q_{hz}^{n+1}, \tag{2.13a}$$

$$Q_{hx}^{n+1} = \mathrm{Z}_0 H_x^{n+1/2} + \frac{c\Delta t}{2}\partial z Q_{ey}^{n+1}, \tag{2.13b}$$

and

$$E_x^{n+1} = Q_{ex}^{n+1} - \frac{c\Delta t}{2}\partial z Q_{hy}^{n+1}, \tag{2.14a}$$

$$H_x^{n+1} = \frac{1}{Z_0} Q_{hx}^{n+1} - \frac{c\Delta t}{2Z_0}\partial y Q_{ez}^{n+1}. \tag{2.14b}$$

Equations for other field components can be found in a similar manner or by cyclic permutation of the indices in the subscripts in (2.11)-(2.14). Detailed formulations can be found in Appendix A.

Next, finite-difference approximations are used to replace the differential operators in the above equations. The finite differences used can be of a chosen order; the expression can be written as follows [52]

$$\frac{\partial \phi}{\partial \zeta} \approx \delta_\zeta \phi\Big|_{\zeta = i_\zeta \Delta\zeta}^{n} = \frac{1}{\Delta\zeta}\sum_{m=0}^{L/2-1} a_m \left(\phi\Big|_{i_\zeta + m + \frac{1}{2}}^{n} - \phi\Big|_{i_\zeta - m - \frac{1}{2}}^{n} \right), \ (\zeta = x, y, \text{ or } z) \tag{2.15}$$

where L is the pre-defined order of the central finite-difference and ϕ is any of the electric or magnetic field component; α_m are the coefficients associated with the user-selected order and they can be found in Table I of [52].

Eqs. (2.11) and (2.13) are implicit equations with different field quantities to be solved on the two sides of the equations. They can be further manipulated for easy computation by combining it with the equations for other field components. After some tedious derivations (which can be found in Appendix A), we can obtain:

$$\begin{aligned} &\left[1 + \frac{\Delta t^2}{2\mu\varepsilon\Delta z^2}\right] Q_{ex(i+1/2,j,k)}^{n+1/2} - \frac{\Delta t^2}{4\mu\varepsilon\Delta z^2} Q_{ex(i+1/2,j,k+1)}^{n+1/2} - \frac{\Delta t^2}{4\mu\varepsilon\Delta z^2} Q_{ex(i+1/2,j,k-1)}^{n+1/2} = E_{x(i+1/2,j,k)}^{n} \\ &- \frac{\Delta t}{2\varepsilon\Delta z}\left(H_{y(i+1/2,j,k+1/2)}^{n} - H_{y(i+1/2,j,k-1/2)}^{n} \right) \end{aligned}, \tag{2.16a}$$

$$Q_{hx(i,j+1/2,k+1/2)}^{n+1/2} = Z_0 H_{x(i,j+1/2,k+1/2)}^{n} - \frac{c\Delta t}{2\Delta y}\left(Q_{ez(i,j+1,k+1/2)}^{n+1/2} - Q_{ez(i,j,k+1/2)}^{n+1/2} \right), \tag{2.16b}$$

and

$$E_{x(i+1/2,j,k)}^{n+1/2} = Q_{ex(i+1/2,j,k)}^{n+1/2} + \frac{c\Delta t}{2\Delta y}\left(Q_{hz(i+1/2,j+1/2,k)}^{n+1/2} - Q_{hz(i+1/2,j-1/2,k)}^{n+1/2} \right), \tag{2.17a}$$

$$H_{x(i,j+1/2,k+1/2)}^{n+1/2}=\frac{1}{Z_0}Q_{hx(i,j+1/2,k+1/2)}^{n+1/2}+\frac{\Delta t}{2\mu\Delta z}\left(Q_{ey(i,j+1/2,k+1)}^{n+1/2}-Q_{ey(i,j+1/2,k)}^{n+1/2}\right), \tag{2.17b}$$

and

$$\left[1+\frac{\Delta t^2}{2\mu\varepsilon\Delta y^2}\right]Q_{ex(i+1/2,j,k)}^{n+1}-\frac{\Delta t^2}{4\mu\varepsilon\Delta y^2}Q_{ex(i+1/2,j+1,k)}^{n+1}-\frac{\Delta t^2}{4\mu\varepsilon\Delta y^2}Q_{ex(i+1/2,j-1,k)}^{n+1}=E_{x(i+1/2,j,k)}^{n+1/2}$$
$$+\frac{\Delta t}{2\varepsilon\Delta y}\left(H_{z(i+1/2,j+1/2,k)}^{n+1/2}-H_{z(i+1/2,j-1/2,k)}^{n+1/2}\right) \quad , \tag{2.18a}$$

$$Q_{hx(i,j+1/2,k+1/2)}^{n+1}=Z_0H_{x(i,j+1/2,k+1/2)}^{n+1/2}+\frac{c\Delta t}{2\Delta z}\left(Q_{ey(i,j+1/2,k+1)}^{n+1}-Q_{ey(i,j+1/2,k)}^{n+1}\right), \tag{2.18b}$$

and

$$E_{x(i+1/2,j,k)}^{n+1}=Q_{ex(i+1/2,j,k)}^{n+1}-\frac{c\Delta t}{2\Delta z}\left(Q_{hy(i+1/2,j,k+1/2)}^{n+1}-Q_{hy(i+1/2,j,k-1/2)}^{n+1}\right), \tag{2.19a}$$

$$H_{x(i,j+1/2,k+1/2)}^{n+1}=\frac{1}{Z_0}Q_{hx(i,j+1/2,k+1/2)}^{n+1}-\frac{\Delta t}{2\mu\Delta y}\left(Q_{ez(i,j+1,k+1/2)}^{n+1}-Q_{ez(i,j,k+1/2)}^{n+1}\right). \tag{2.19b}$$

(2.16a) and (2.18a) are the linear systems of equations with the diagonally banded coefficient matrix; they can be solved efficiently for each field component with special mathematical solvers such as Thomas algorithm [53].

It is worth mentioning that in developing the above divergence-preserved ADI-FDTD method, three approximations have been applied: i) matrix exponential expansion (2.5), ii) Taylor's series and Padé approximation (2.6), and iii) finite-difference replacement of the spatial differential operators (2.15).

2.1.4 Stability Analysis

The von Neumann method [54] is used to analyze the stability property of the presented divergence preserved ADI-FDTD method in this chapter. After projection of each field component into the spectral domain, the amplification matrix of the presented method is obtained. The magnitudes of all the eigenvalues of the amplification matrix are then examined analytically: if all of them are not larger than unity in magnitude in any situation, the method is considered unconditionally stable.

Suppose that k_x, k_y and k_z are the spatial frequencies along the x, y and z directions, respectively. Then, any field component in the spectral domain can be described as:

$$\phi\big|^{n}_{x=i_x\Delta x,y=i_y\Delta y,z=i_z\Delta z} = \phi^n \cdot e^{-j(k_x i_x\Delta x+k_y i_y\Delta y+k_z i_z\Delta z)}, \tag{2.20}$$

where ϕ^n is the amplitude at the nth time step.

The central finite-difference (2.20) of order M in the spectral domain can be written as:

$$\frac{c\Delta t}{2}\partial\zeta\phi\,|^{n}_{\zeta=i_\zeta\Delta\zeta} \approx \frac{c\Delta t}{2}\delta_\zeta\phi\,|^{n}_{\zeta=i_\zeta\Delta\zeta} = R_\zeta e^{-jk_\zeta i_\zeta\Delta\zeta}\phi^n, \tag{2.21}$$

where $\zeta = x, y$ or z , and

$$R_\zeta = -j\frac{c\Delta t\sum_{m=0}^{M/2-1} a_m \sin\left[\frac{(2m+1)}{2}k_\zeta\Delta\zeta\right]}{\Delta\zeta}. \tag{2.22}$$

Substitution of (2.21) into each field component leads to:

$$\mathbf{U}^{n+1} = \Lambda\mathbf{U}^n, \tag{2.23}$$

where $\mathbf{U}^n = \left[E_x^n, E_y^n, E_z^n, H_x^n, H_y^n, H_z^n\right]^T$ and Λ is the amplification matrix defined as:

$$\mathbf{\Lambda} = \mathbf{T}^{-1}\left(\mathbf{M}_{L2}\mathbf{M}_{R2}^{-1}\right)\left(\mathbf{M}_{L1}\mathbf{M}_{R1}^{-1}\right)\mathbf{T} \tag{2.24}$$

with

$$\mathbf{T} = \begin{bmatrix} 1 & 0 & 0 & 0 & 0 & 0 \\ 0 & 1 & 0 & 0 & 0 & 0 \\ 0 & 0 & 1 & 0 & 0 & 0 \\ 0 & 0 & 0 & Z_0 & 0 & 0 \\ 0 & 0 & 0 & 0 & Z_0 & 0 \\ 0 & 0 & 0 & 0 & 0 & Z_0 \end{bmatrix}, \tag{2.25}$$

$$\mathbf{M}_{R1}=\begin{bmatrix} 1 & 0 & 0 & 0 & R_z & 0 \\ 0 & 1 & 0 & 0 & 0 & R_x \\ 0 & 0 & 1 & R_y & 0 & 0 \\ 0 & 0 & R_y & 1 & 0 & 0 \\ R_z & 0 & 0 & 0 & 1 & 0 \\ 0 & R_x & 0 & 0 & 0 & 1 \end{bmatrix}, \tag{2.26a}$$

$$\mathbf{M}_{L1}=\begin{bmatrix} 1 & 0 & 0 & 0 & 0 & R_y \\ 0 & 1 & 0 & R_z & 0 & 0 \\ 0 & 0 & 1 & 0 & R_x & 0 \\ 0 & R_z & 0 & 1 & 0 & 0 \\ 0 & 0 & R_x & 0 & 1 & 0 \\ R_y & 0 & 0 & 0 & 0 & 1 \end{bmatrix}, \tag{2.26b}$$

$$\mathbf{M}_{R2}=\begin{bmatrix} 1 & 0 & 0 & 0 & 0 & -R_y \\ 0 & 1 & 0 & -R_z & 0 & 0 \\ 0 & 0 & 1 & 0 & -R_x & 0 \\ 0 & -R_z & 0 & 1 & 0 & 0 \\ 0 & 0 & -R_x & 0 & 1 & 0 \\ -R_y & 0 & 0 & 0 & 0 & 1 \end{bmatrix}, \tag{2.26c}$$

and

$$\mathbf{M}_{L2}=\begin{bmatrix} 1 & 0 & 0 & 0 & -R_z & 0 \\ 0 & 1 & 0 & 0 & 0 & -R_x \\ 0 & 0 & 1 & -R_y & 0 & 0 \\ 0 & 0 & -R_y & 1 & 0 & 0 \\ -R_z & 0 & 0 & 0 & 1 & 0 \\ 0 & -R_x & 0 & 0 & 0 & 1 \end{bmatrix}. \tag{2.26d}$$

The eigenvalues of Λ can be obtained, with the help of MAPLE, as

$$\lambda_1=\lambda_2=1, \tag{2.27a}$$

$$\lambda_3=\lambda_4=-\frac{B+2j\sqrt{D}}{A}, \tag{2.27b}$$

$$\lambda_5=\lambda_6=-\frac{B-2j\sqrt{D}}{A}, \tag{2.27c}$$

where $A=A_1+A_3-A_2-1$, $B=1+A_3-A_2-A_1$, and $D=A_2-A_3+A_3A_1-A_1A_2$ with $A_1=R_x^2R_y^2R_z^2$, $A_2=R_x^2R_y^2+R_x^2R_z^2+R_y^2R_z^2$ and $A_3=R_x^2+R_y^2+R_z^2$.

Obviously, the magnitudes of the first two eigenvalues are unity. For the rest of

eigenvalues, $|\lambda_3| = |\lambda_4| = |\lambda_5| = |\lambda_6| \le 1.0$ can be easily found by substitution of R_ζ into (2.27). Consequently, all the eigenvalues are not larger than unity in their magnitudes. Thus, the divergence preserved ADI-FDTD method is considered unconditionally stable. Numerical verification of the unconditional stability will be presented in the later section.

2.1.5 Numerical Dispersion

To obtain the numerical dispersion formulation, the time harmonic fields are considered in (2.23); it reads

$$\mathbf{U}^{n+1} = e^{j\omega\Delta t}\mathbf{U}^{n}. \tag{2.28}$$

By substitution of the above equation into (2.23), we can obtain:

$$\left(e^{j\omega\Delta t}\mathbf{I} - \Lambda\right)\mathbf{U}^{n} = 0. \tag{2.29}$$

For (2.29) to have a non-trivial solution, the determinant of the coefficient matrix of (2.29) should be zero. The zero-valued determinant forms the dispersion relationship of the presented divergence preserved ADI-FDTD method:

$$\det\{e^{j\omega\Delta t}\mathbf{I} - \Lambda\} = 0. \tag{2.30}$$

After some mathematical manipulations, (2.30) can be simplified and rewritten as:

$$\sin^2(\omega\Delta t) = \frac{4D}{A^2}. \tag{2.31}$$

Based on the work presented in [16, 55], we can easily find that (2.31) is the same as that of the conventional ADI-FDTD, the one-step leapfrog ADI-FDTD and the LOD-FDTD methods. In other words, the numerical dispersion of the method presented in this section is the same as the ones previously proposed in [16]. However, the method proposed here is divergence-preserved while other methods are not.

2.1.6 Current Source Implementation

This section shows the current source implementation of the divergence preserved ADI-FDTD method.

The time-marching formulations along with the current sources can be written as follows:

$$\mathbf{V}^{n+1/2} = \left(\mathbf{I} + \frac{c\Delta t}{2}\mathbf{P}\right)\left(\mathbf{I} - \frac{c\Delta t}{2}\mathbf{M}\right)^{-1}\mathbf{V}^{n} + c\Delta t\mathbf{S}^{n+1/2}, \tag{2.32}$$

where $\mathbf{S}^{n+1/2} = -\left[Z_0 J_x^{n+1/2} \quad Z_0 J_y^{n+1/2} \quad Z_0 J_z^{n+1/2} \quad J_{mx}^{n+1/2} \Big/ Z_0 \quad J_{my}^{n+1/2} \Big/ Z_0 \quad J_{mz}^{n+1/2} \Big/ Z_0 \right]^T$, $J_x^{n+1/2}$, $J_y^{n+1/2}$ and $J_z^{n+1/2}$ are the electric current densities in the x, y, and z directions at the n+1/2 time step, respectively, and $J_{mx}^{n+1/2}$, $J_{my}^{n+1/2}$ and $J_{mz}^{n+1/2}$ are the equivalent magnetic current densities in the x, y, and z directions at the n+1/2 time step, respectively.

With Strang splitting, we can obtain the final updating equations for (2.32) that include the current source:

$$\left(\mathbf{I} - \frac{c\Delta t}{2} \mathbf{M} \right) \mathbf{Q}^{n+1/2} = \mathbf{V}^n , \tag{2.33a}$$

$$\mathbf{V}^{n+1/2} = \left(\mathbf{I} + \frac{c\Delta t}{2} \mathbf{P} \right) \mathbf{Q}^{n+1/2} + c\Delta t \mathbf{S}^{n+1/2} . \tag{2.33b}$$

In [56], we can find that the source terms of the conventional ADI-FDTD method are applied in two sub-steps. However, in the presented ADI-FDTD method, the current source only needs to be applied at the first sub-time step; that is to say that a compact and simple approach is adopted with the presented method here.

2.1.7 Numerical Examples and Discussion

In this section, accuracy and unconditional stability of the proposed ADI-FDTD method are first verified numerically. Then, divergence preservation is shown numerically compared with that of the conventional ADI-FDTD method.

A. Accuracy verification

To verify the accuracy and unconditional stability of the proposed ADI-FDTD method, an air cavity with dimensions of 50 × 50 × 50 cells was considered like the one used in [16]. The uniform cell size ($\Delta x = \Delta y = \Delta z = 2$ *mm*) was chosen. A current line source J_{mz} was located at the center of the cavity from the bottom to the top. The observation point was also placed at the center.

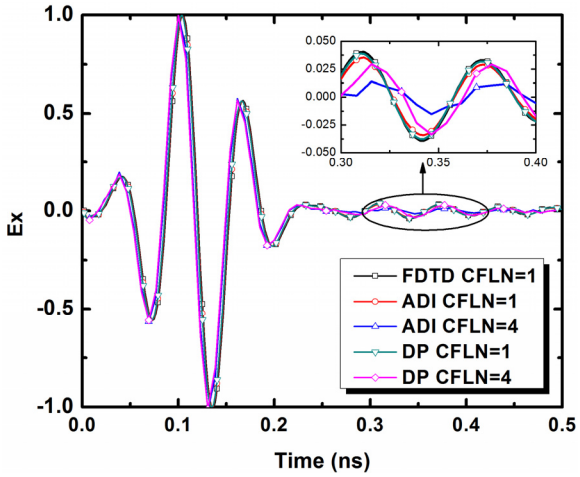

Figure 2.1 Normalized E_x computed with the second order explicit FDTD method, the conventional ADI-FDTD method and the proposed divergence preserved ADI-FDTD method, which are presented as FDTD, ADI and DP, respectively, of $CFLN = 1$ and $CFLN = 4$.

Figure 2.1 shows the normalized E_x obtained with the conventional FDTD method, the conventional ADI-FDTD method and the presented divergence-preserved ADI-FDTD method with $CFLN = 1$ and $CFLN = 4$, where $CFLN$ is defined as the ratio of the time step used to the CFL limit. It can be easily found that E_x obtained with the conventional ADI-FDTD method has a larger difference from that that obtained the FDTD method than the present method especially when $CFLN = 4$. In other words, the result obtained with the presented method agrees better with that of the conventional FDTD method than the conventional ADI-FDTD with large $CFLN$.

Table 2-1 Comparison of computational expenditures used by the FDTD method, the conventional ADI-FDTD method and the divergence preserved ADI-FDTD method.

	FDTD	Conventional ADI		Presented method	
CFLN	1	1	4	1	4
Overall cells	125000	125000		125000	
Number of iterations	259	259	64	259	64
Time(s)	8.20	25.47	6.34	27.42	6.76
Memory(Mb)	6.52	9.56	9.56	12.52	12.52

Table 2.1 shows the computational time and memory used by the conventional FDTD, the conventional ADI-FDTD method and the divergence preserved ADI-FDTD method. It is found that the divergence preserved ADI-FDTD method consumes slightly more time

and about 31% more memory in comparison with the conventional ADI-FDTD method. This is because the method has 24 For-loops for one time step. That is, the computational efficiency of the presented method is decreased by a larger count of For-loops operations. In addition, since additional intermediate variables are used, the memory consumption is higher. On the other hand, the presented method used 18% less CPU time with $CFLN = 4$ than the conventional FDTD.

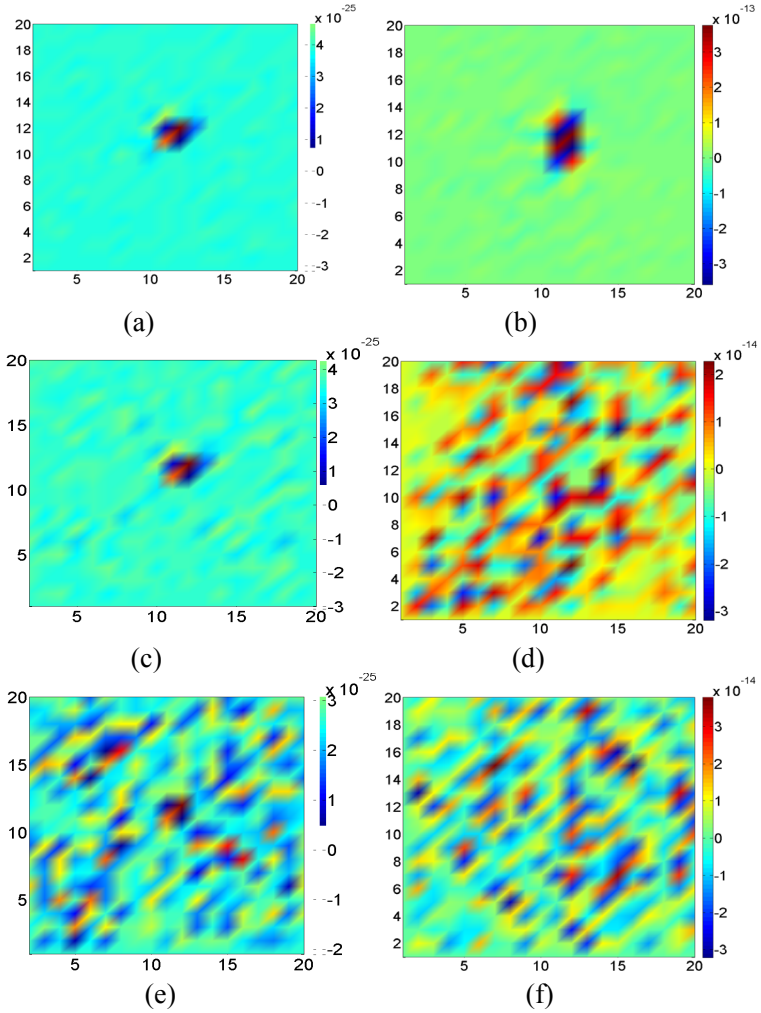

Figure 2.2 Charge distribution computed with the presented method, the conventional ADI-FDTD method with $CFLN = 1$; Figures on the left are the electric charges with the presented method at $t = 0.23$ *ns*, 1 *ns*, and 10 *ns*, respectively; Figures on the right are the electric charges with the conventional ADI-FDTD method at $t = 0.23$ *ns*, 1 *ns*, and 10 *ns*, respectively.

B. Divergence verification

To examine divergence property of the presented method, an air-filled PEC cavity is considered with dimension of uniform $20 \times 20 \times 20$ cells and spatial step is $\Delta x = \Delta y = \Delta z = \lambda/20$. A sinusoidal modulated Gaussian pulse excitation is placed at (10, 10, 10) with:

$$J_{mz} = \sin\left[2\pi f_0 \left(t - t_0\right)\right] e^{-(\frac{t-t_0}{\tau})^2}, \quad (2.34)$$

with $f_0 = 15\ GHz, \tau = 60\ ps$ and $t_0 = 2\tau$ [22].

Electric charges were numerically computed with $\frac{q}{\varepsilon_0} = \oint_S \mathbf{E} \bullet d\mathbf{s}$, in which the integral surface S is each Yee's cell. Figure 2.2 shows the distribution of the computed electric charge $\frac{q}{\varepsilon_0}$ in the *xy*-plane at *z* = 10 for *CFLN* = 1 at time instant *t* = 0.23 *ns*, 1 *ns*, and 10 *ns*, obtained with the presented ADI-FDTD method and the conventional ADI-FDTD method. The results obtained with the leapfrog Yee's FDTD method are not shown because they are divergence-preserved and are zeros at any time.

As shown in Figure 2.2, electric charges with the conventional ADI-FDTD method reach the order of 10^{-14}. However, electric charges computed with the presented method are in the order of 10^{-25}. It implies that the divergence preserved ADI-FDTD method has great improvement in terms of charge accumulation. This verifies that the divergence preserved ADI-FDTD method is basically divergence free.

2.2 Efficiency Improved Divergence Preserved ADI-FDTD Method

2.2.1 Abstract

In this section, a newly formulated divergence preserved ADI-FDTD method is proposed and its divergence property is theoretically and numerically analyzed. It takes about 41.7% less count of floating-point operations than the original divergence-preserved ADI-FDTD method without sacrificing accuracy. Detailed analysis of computational efficiency and divergence property are shown. Numerical experiments, which illustrates the divergence property, efficiency and memory cost, are presented to verify the improvement of computational efficiency.

2.2.2 Formulations of the Proposed Efficiency Improved Divergence Preserved ADI-FDTD Method

Eqns. (2.9) and (2.10) form the original divergence-preserved ADI-FDTD method.

Now we substitute (2.9b) into (2.10a):

$$\left(\mathbf{I}-\frac{c\Delta t}{2}\mathbf{P}\right)\mathbf{Q}^{n+1}=\left(\mathbf{I}+\frac{c\Delta t}{2}\mathbf{P}\right)\mathbf{Q}^{n+1/2}=2\mathbf{Q}^{n+1/2}-\left(\mathbf{I}-\frac{c\Delta t}{2}\mathbf{P}\right)\mathbf{Q}^{n+1/2}. \tag{2.35}$$

Then,

$$\left(\frac{\mathbf{I}}{2}-\frac{c\Delta t}{4}\mathbf{P}\right)\left(\mathbf{Q}^{n+1}+\mathbf{Q}^{n+1/2}\right)=\mathbf{Q}^{n+1/2} \tag{2.36}$$

Eqn. (2.36) can be reformulated with the introduction of intermediate **U** such that

$$\left(\frac{\mathbf{I}}{2}-\frac{c\Delta t}{4}\mathbf{P}\right)\mathbf{U}^{n+1/2}=\mathbf{Q}^{n+1/2}, \tag{2.37a}$$

$$\mathbf{Q}^{n+1}=\mathbf{U}^{n+1/2}-\mathbf{Q}^{n+1/2}, \tag{2.37b}$$

where $\mathbf{U}^{n+1/2}=\left[U_{ex}^{n+1/2},U_{ey}^{n+1/2},U_{ez}^{n+1/2},U_{hx}^{n+1/2},U_{hy}^{n+1/2},U_{hz}^{n+1/2}\right]^{T}$.

For the second sub time step, we advance (2.9a) by one time step and have:

$$\left(\mathbf{I}-\frac{c\Delta t}{2}\mathbf{M}\right)\mathbf{Q}^{n+3/2}=\mathbf{V}^{n+1}. \tag{2.38}$$

By substituting (2.38) into (2.10b), we obtain:

$$\left(\mathbf{I}-\frac{c\Delta t}{2}\mathbf{M}\right)\mathbf{Q}^{n+3/2}=\left(\mathbf{I}+\frac{c\Delta t}{2}\mathbf{M}\right)\mathbf{Q}^{n+1}=2\mathbf{Q}^{n+1}-\left(\mathbf{I}-\frac{c\Delta t}{2}\mathbf{M}\right)\mathbf{Q}^{n+1}, \tag{2.39a}$$

$$\left(\frac{\mathbf{I}}{2}-\frac{c\Delta t}{4}\mathbf{M}\right)\left(\mathbf{Q}^{n+3/2}+\mathbf{Q}^{n+1}\right)=\mathbf{Q}^{n+1}. \tag{2.39b}$$

Then, (2.39b) can be rewritten as

$$\left(\frac{\mathbf{I}}{2}-\frac{c\Delta t}{4}\mathbf{M}\right)\mathbf{U}^{n+1}=\mathbf{Q}^{n+1}, \tag{2.40a}$$

$$\mathbf{Q}^{n+3/2}=\mathbf{U}^{n+1}-\mathbf{Q}^{n+1}. \tag{2.40b}$$

Eqns. (2.37) and (2.40) forms the basic field updating equations of the proposed efficiency-improved divergence-preserved ADI-FDTD methods. Unlike (2.9b) and (2.10b) of the original divergence-preserved ADI-FDTD method, (2.37b) and (2.37b) of the proposed method involve only simple matrix subtractions and do not require matrix multiplications, the proposed divergence-preserved method is more computationally efficiency as will be shown in more detail in next section.

Moreover, when expanded into component fields, (2.37) and (2.40) of the proposed method can be further simplified. Take the components in the *x* direction of *U* and *Q* for example; for field march from the *n*th time step to the (*n+1/2*)th time step, after some mathematic manipulations, we have:

$$\frac{1}{2}U_{ex}^{n+1/2}-\frac{c^2\Delta t^2}{8}\partial_y^2 U_{ex}^{n+1/2}=Q_{ex}^{n+1/2}+\frac{c\Delta t}{2}\partial y Q_{hz}^{n+1/2}, \tag{2.41a}$$

$$Q_{ex}^{n+1}=U_{ex}^{n+1/2}-Q_{ex}^{n+1/2}, \tag{2.41b}$$

$$Q_{hx}^{n+1}=Q_{hx}^{n+1/2}+\frac{c\Delta t}{2}\partial z U_{ey}^{n+1/2} \quad . \tag{2.41c}$$

For field march from the (*n+1/2*)th time step to the (*n+1*)th sub-time step, we have

$$\frac{1}{2}U_{ex}^{n+1}-\frac{c^2\Delta t^2}{8}\partial_z^2 U_{ex}^{n+1}=Q_{ex}^{n+1}-\frac{c\Delta t}{2}\partial z Q_{hy}^{n+1} \quad , \tag{2.42a}$$

$$Q_{ex}^{n+3/2}=U_{ex}^{n+1}-Q_{ex}^{n+1}, \tag{2.42b}$$

$$Q_{hx}^{n+3/2}=Q_{hx}^{n+1}-\frac{c\Delta t}{2}\partial y U_{ez}^{n+1}. \tag{2.42c}$$

As seen from the above equations, U_{hx}, U_{hy}, and U_{hz} are not required to be computed. In other words, for **U** vector, only U_{ex}, U_{ey}, U_{ez} components needs to be updated in each time step; as a result, memory consumption and CPU time of the proposed method is further saved.

In the above field updating equations of (2.37), (2.40), (2.41) and (2.42), field components are not computed directly. Rather, they are related to **Q** through the following

equation:

$$\mathbf{V}^{n+1} = \left(\mathbf{I} + \frac{c\Delta t}{2} \mathbf{M} \right) \mathbf{Q}^{n+1} \quad , \tag{2.43}$$

with the initial condition

$$\left(\mathbf{I} - \frac{c\Delta t}{2} \mathbf{M} \right) \mathbf{Q}^{1/2} = \mathbf{V}^{0} . \tag{2.44}$$

The computing process for the proposed method is shown as follows:

Calculate the coefficients based on (2.37a) and (2.40a)
Intial updating $Q^{1/2}$ based on intial condition (2.44)

for i = 0 to the n+1th timestep
updating Uex, Qex in one loop based on (2.41a) and (2.41b) at n+1/2 time step;
updating Uey, Qey in one loop at n+1/2 time step;
updating Uez, Qez in one loop at n+1/2 time step;

updating Qhx at n+1/2 time step based on (2.41c);
updating Qhy at n+1/2 time step;
updating Qhz at n+1/2 time step;

updating Uex, Qex in one loop based on (2.42a) and (2.42b) at n+1 time step;
updating Uey, Qey in one loop at n+1 time step;
updating Uez, Qez in one loop at n+1 time step;

updating Qhx at n+1 time step based on (2.42c);
updating Qhy at n+1 time step;
updating Qhz at n+1 time step;

end

Extract electrical and magnetic fields based on (2.43)

The efficiency of the proposed method is further discussed in next section.

2.2.3 Efficiency Comparison between the Proposed Method and the Other ADI-FDTD Methods

In this section, the floating-point operation counts of the proposed divergence-preserved ADI-FDTD method are compared with those of other ADI-FDTD methods. Table 2-2 shows the counts of floating-point operations of the conventional non-divergence-preserved ADI-FDTD method and its improved variation, the original divergence-preserved ADI-FDTD method and the proposed efficiency-improved divergence-preserved method. In Table 2-2, "M/D" means multiplication/division and A/S addition/subtraction operations on the right hand sides of the field updating equations used in each method for field to advance for a complete full time step. "Implicit" refers to implicit updating equations. "Explicit" refers to explicit updating equations. The numbers of For-loops are for updating of all components in the x, y, and z directions.

Table 2-2 Floating-point operation counts of different implicit schemes with second-order central difference

Scheme		Non-divergence-preserved ADI		Divergence preservation ADI	
Algorithm		Convent.	Improved	Original	Proposed
Implicit	M/D	18	6	6	6
	A/S	48	18	12	12
Explicit	M/D	12	6	18	6
	A/S	24	12	36	18
Total		102	42	72	42
For-loops		12	12	24	12

As can be seen from Table 2.2, the count of total floating-point operations of the proposed method is about 58.8% less than that of the conventional non-divergence-preserved ADI-FDTD method and is same as that of its improved variation [57]; however, the proposed method preserves the correct divergence property. Therefore, the proposed

method should be more accurate than the original ADI-FDTD method in applications such as electromagnetic PIC simulations [49] where charges are involved. In comparison with the original divergence-preserved ADI-FDTD method [25], the count is 41.7% less. It should be mentioned that in comparison with the most recently developed efficient one-step leapfrog ADI-FDTD method [16], the proposed method has a higher count of floating-point operations, but the one-step method is not divergence preserved [22].

In terms of the memory consumption, the proposed method is similar to the conventional non-divergence-preserved ADI-FDTD method. As presented in (2.37) and (2.40), **U** and **Q** which store the intermediate field values are needed to be computed. More specifically, only U_{ex}, U_{ey}, and U_{ez} need to be computed in every full time step. In comparison with the one-step leap-frog ADI-FDTD method [58], the proposed method uses more memory since the one-step method does not require the computation of intermediate values. However, the proposed method is divergence-preserved while the other methods are not.

For the numbers of For-loops, with careful arrangements of the position of the field components, (2.41a) and (2.41b) can be combined into one For-loop so that increasing the number of For-loops is avoided. This is, only half number of the For-loops of the original divergence-preserved ADI-FDTD method [25] (i.e., half of the 24 For-loops) is computed in the proposed method.

2.2.4 Analytical Proof of Divergence-free Properties of the Improved ADI-FDTD Method

In this part, the theoretical study of divergence properties of (2.37) and (2.40) is presented. In order to test their divergence, charge accumulation is evaluated analytically with the Gaussian law at every time step of the new efficiency-improved method of (2.37) and (2.40). If increase of the charge is zero, the method can be considered to be divergence free in a source free region.

For the first sub time step, from (2.37a), we have:

$$\mathbf{U}^{n+1/2} = \left(\frac{\mathbf{I}}{2} - \frac{c\Delta t}{4}\mathbf{P}\right)^{-1} \mathbf{Q}^{n+1/2}, \tag{2.45}$$

Substitution of (2.45) into (2.37b) reads:

$$\mathbf{Q}^{n+1} = \left(\left(\frac{\mathbf{I}}{2} - \frac{c\Delta t}{4}\mathbf{P} \right)^{-1} - \mathbf{I} \right) \mathbf{Q}^{n+1/2} . \tag{2.46}$$

For the second sub-time step, the updating equation can be obtained in a similar manner by taking one time step backward.

$$\left(\mathbf{I} + \frac{c\Delta t}{2}\mathbf{M} \right) \mathbf{Q}^{n} = \left(\mathbf{I} - \frac{c\Delta t}{2}\mathbf{M} \right) \mathbf{Q}^{n+1/2} . \tag{2.47}$$

The increase of the fields at every time step is then:

$$\begin{aligned} \mathbf{V}^{n+1} - \mathbf{V}^{n} &= \left(\left(\mathbf{I} + \frac{c\Delta t}{2}\mathbf{M} \right) \left(\left(\frac{\mathbf{I}}{2} - \frac{c\Delta t}{4}\mathbf{P} \right)^{-1} - \mathbf{I} \right) - \left(\mathbf{I} - \frac{c\Delta t}{2}\mathbf{M} \right) \right) \mathbf{Q}^{n+1/2} \\ &= \left(\left(\mathbf{I} + \frac{c\Delta t}{2}\mathbf{M} \right) \left(\frac{\mathbf{I}}{2} - \frac{c\Delta t}{4}\mathbf{P} \right)^{-1} - \left(\mathbf{I} + \frac{c\Delta t}{2}\mathbf{M} \right) - \left(\mathbf{I} - \frac{c\Delta t}{2}\mathbf{M} \right) \right) \mathbf{Q}^{n+1/2} \\ &= 2 \left(\left(\mathbf{I} + \frac{c\Delta t}{2}\mathbf{M} \right) \left(\mathbf{I} - \frac{c\Delta t}{2}\mathbf{P} \right)^{-1} - \mathbf{I} \right) \mathbf{Q}^{n+1/2} \end{aligned} \tag{2.48}$$

Since

$$\begin{aligned} &\left(\mathbf{I} + \frac{c\Delta t}{2}\mathbf{M} \right) \left(\mathbf{I} - \frac{c\Delta t}{2}\mathbf{P} \right)^{-1} \\ &= \left(\mathbf{I} - \frac{c\Delta t}{2}\mathbf{P} + \frac{c\Delta t}{2}\mathbf{P} + \frac{c\Delta t}{2}\mathbf{M} \right) \left(\mathbf{I} - \frac{c\Delta t}{2}\mathbf{P} \right)^{-1} , \\ &= \mathbf{I} + \frac{c\Delta t}{2}\left(\mathbf{P} + \mathbf{M} \right) \left(\mathbf{I} - \frac{c\Delta t}{2}\mathbf{P} \right)^{-1} \end{aligned} \tag{2.49}$$

We then have:

$$\mathbf{V}^{n+1} - \mathbf{V}^{n} = c\Delta t \left(\mathbf{P} + \mathbf{M} \right) \left(\mathbf{I} - \frac{c\Delta t}{2}\mathbf{P} \right)^{-1} \mathbf{Q}^{n+1/2} \quad . \tag{2.50}$$

P+**M** represents the curl operator in Maxwell equations [25]. Based on the fact that the divergence of curl operation of any fields is always zero, we have:

$$\nabla_f \bullet (\mathbf{P}+\mathbf{M})\mathbf{X}=0 \tag{2.51}$$

where ∇_f is the Delta operator.

As a result,

$$\nabla_f \bullet \left(\mathbf{V}^{n+1}-\mathbf{V}^{n}\right)=c\Delta t\nabla_f \bullet (\mathbf{P}+\mathbf{M})\left(\mathbf{I}-\frac{c\Delta t}{2}\mathbf{P}\right)^{-1}\mathbf{Q}^{n+1/2}=0 \tag{2.52}$$

In other words, no charges accumulate in advance of time steps if initial charges are zero. That is to say the new efficiency-improved divergence-preserved ADI-FDTD method remains divergence free in a source free region.

2.2.5 Numerical Examples and Discussion

A cavity filled with air was selected [58] to verify the accuracy and efficiency of the proposed method. A grid of 250 × 150 × 45 (= 1.6875 millions) cells with a uniform cell size of $\Delta x = \Delta y = \Delta z = 0.4$ mm was employed. The source function is $e^{-(t-\tau)^2/t_w^2}$ with t_w = 150 *ps* and τ = 450 *ps*. A current plane source J_z was placed at y = 75 and the observation point was located at (125, 80, 23).

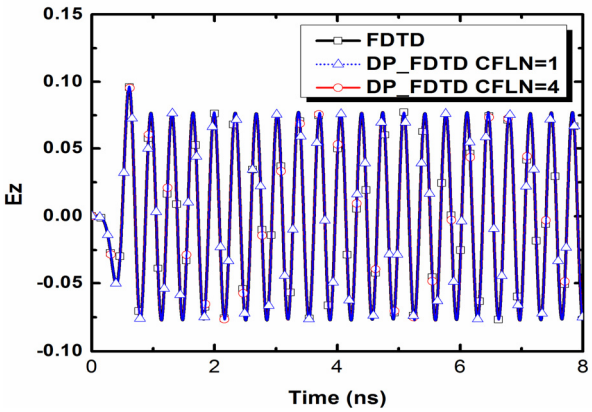

Figure 2.3 E_z computed with the second order explicit FDTD method with *CFLN* = 1, and the proposed divergence preservation ADI-FDTD method with *CFLN* = 1 and 4 and with uniform mesh.

The results were obtained with the conventional FDTD method with *CFLN*=1 and the proposed method with *CFLN* = 1 and 4, respectively. Figure 2.3 shows the E_z obtained with the two methods and Figure 2.4 presents the relative absolute error of E_z computed with the proposed method in reference to the results obtained with the conventional FDTD method. The reason for the large relative error in the time domain when *CFLN* = 4 is time delay of E_z from two methods which leads to large absolute error at each time instant. However, we can observe that the wave form almost the same but with some time delay. The results obtained with the two methods are visibly indistinguishable. That is, that the proposed efficiency-improved divergence-preserved FDTD method has good modeling accuracy.

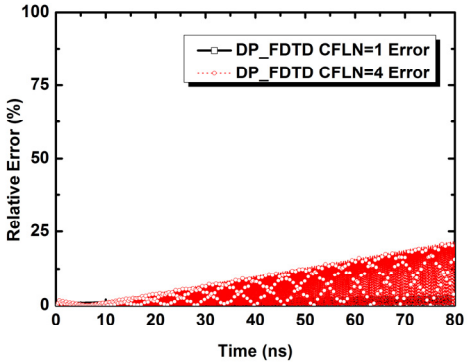

Figure 2.4 Absolute relative error of E_z computed with the proposed divergence preservation ADI-FDTD method of *CFLN* = 1, 4.

Table 2-3 Comparison of results with conventional FDTD method and the proposed method

Analytical (GHz)	FDTD *CFLN*=1(GHz)	Proposed *CFLN*=1(GHz)	Proposed *CFLN*=4(GHz)
2.915	2.914	2.911	2.912
5.220	5.213	5.212	5.210
6.727	6.720	6.722	6.716
7.648	7.642	7.640	7.630

Table 2.3 presents resonance frequencies obtained from analytical method, the conventional FDTD method and the proposed efficiency-improved divergence-preserved ADI-FDTD methods with *CFLN* = 1 and 4. It is easy to find that the errors of the proposed method are slightly larger than the conventional FDTD method and they increase with *CFLN*.

Table 2.4 shows the usages of time and memory by the FDTD method, the original divergence-preserved ADI-FDTD method, and the proposed method. Compared with the original divergence preserved ADI-FDTD method, the proposed method took about 14% less CPU time with *CFLN*=4 and 25% less memory at the same accuracy. In comparison with the conventional FDTD method, the proposed method used 49% more memory due to the introduction of the intermediate values of U_{ex}, U_{ey}, U_{ez} but 73% less CPU time with *CFLN*=4.

Table 2-4 Comparison of the time and memory used by the Yee's FDTD method, the original divergence preserved ADI-FDTD method and the proposed method

	Yee's FDTD	Original Divergence-Preserved ADI-FDTD Method		Proposed Method	
CFLN	1	1	4	1	4
Number of cells	1687500	1687500		1687500	
Number of iterations	10385	10385	2596	10385	2596
Time(s)	2206	2735	689	2396	592
Memory(Mb)	80.5	159.4	159.4	119.9	119.9

To numerically evaluate the divergence properties of the improved ADI-FDTD method, charge distribution was calculated through a numerical example. The charge computed was normalized to an electron *e*:

$$Q^{'} = \frac{Q}{e} = \frac{\int \vec{\mathrm{D}} \bullet d\mathbf{s}}{e}. \tag{2.53}$$

An example is an air-filled PEC cavity with dimension of uniform 50 × 50 × 50 cells and each is with $\Delta x = \Delta y = \Delta z = \lambda/20$ [22]. A simusoidal modulated Gaussian pulse excitation was placed at the centre of the cavity:

$$J_z = \sin\left[2\pi f_0 \left(t - t_0\right)\right] e^{-\left(\frac{t-t_0}{\tau}\right)^2} \tag{2.59}$$

with $f_0 = 15\,GHz, \tau = 60\,ps, t_0 = 2\tau.$

Figure 2.5 shows the normalized charge distribution in the *xy*-plane at $z = 25$ and at time instant $t = 0.13ns$ with the original ADI-FDTD method, the original divergence preserved ADI-FDTD method, and the efficiency-improved ADI-FDTD method. We can easily see

from Figure 2.5(a) and Figure 2.5(b) that amount of the normalized charge, which is normalized to the unit charge, can reach 1.5 with *CFLN* =1 and 4 with the original ADI-FDTD method. It implies that the normalized charge will increase with increase of the time steps. However, for the divergence preserved ADI-FDTD method and the new efficiency-improved method, values of the normalized charges are around the order of 10^{-14}, which are basically negligible numerical noises (see Figure 2.5(c) – Figure 2.5(f)). This means that the new efficiency-improved method behaves like the conventional explicit FDTD method as well as the original divergence preserved ADI-FDTD method and produces no charge-accumulating divergent fields.

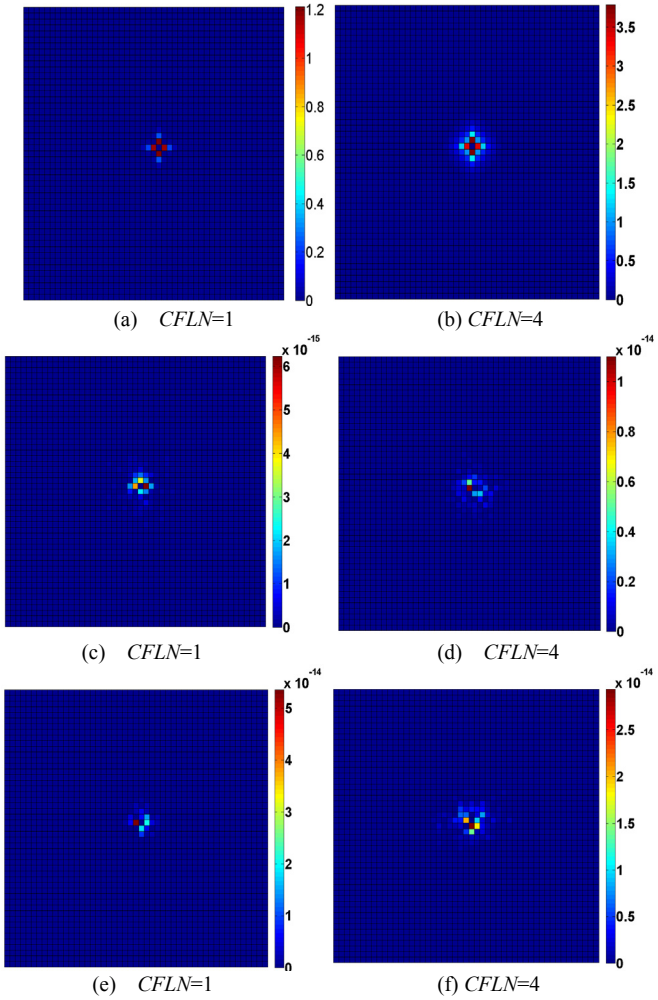

Figure 2.5 Normalized charge distributions computed (a) and (b) with the original ADI-FDTD method, (c) and (d) with the original divergence preserved ADI-FDTD method and, (e) and (f) with the efficiency-improved divergence preserved ADI-FDTD method.

2.3 Conclusion

In this chapter, a divergence preserved ADI-FDTD method is presented and formulated. The method is analytically proven and numerically verified to be unconditionally stable. Compared with other unconditionally implicit methods, such as the conventional ADI-FDTD method, the one-step leapfrog ADI-FDTD method and the LOD-FDTD method, the divergence preserved ADI-FDTD method has the same numerical dispersion characteristics but preserve divergence property like the explicit FDTD method. In other words, the presented ADI-FDTD method is the most accurate among the unconditionally stable implicit methods when charge particles have to be included in simulations. The improvement in accuracy comes at the cost of higher computational expenditures.

In addition, a new efficiency-improved divergence-preserved ADI-FDTD formulation has been proposed and its efficiency comparisons with other FDTD methods are presented. The divergence property of the new method has been investigated. Analytical proof shows that the efficiency-improved method retains the divergence-free property in source free regions like the original divergence-preserved method but with higher computational efficiency. It is found that the proposed method is more efficient than the original divergence-preserved ADI-FDTD method in both memory and CPU time. In comparison with the FDTD, it uses about 50% more memory but less CPU time if time step is chosen to be adequately large. Therefore, due to its divergence property and high efficiency, the proposed divergence preserved ADI-FDTD method is recommended as an FDTD based alternative technique if unconditional stability is required for modeling (e.g. highly resolved fields).

Chapter 3 The Time Domain Meshless Method for Solving Electromagnetics Problems

This chapter is mainly based on our published paper [42], which is Shunchuan Yang, Yiqiang Yu, Zhizhang (David) Chen, and Sergey Ponomarenko, "A Time-Domain Collocation Meshless Method with Local Radial Basis Functions for Transient Analysis," published in IEEE Transactions on Antennas and Propagation, vol. 62, pp. 5334 - 5338, 2014.

3.1 Abstract

A meshless method with local radial basis functions is proposed for solving the electromagnetic wave equations. In comparison with the conventional RPIM method that employs and positions dual sets of nodes of both electric and magnetic field nodes, the proposed method uses only one set of the nodes, where electric fields are collocated at those nodes in space. With this feature, implementation complexity of the RPIM method is significantly reduced, and conformal modeling and muti-scale capabilities of the RPIM method can now be further explored with higher efficiency. The time-marching formulations of the proposed method are derived and stability analysis of the method is presented. Comparisons of the proposed method with the conventional meshless method are also presented. The accuracy and efficiency of the proposed method are demonstrated through simulation of an H-shaped cavity and a quarter ring resonator.

3.2 Introduction

Conventional numerical methods, such as the FDTD method [6], the FEM [59] and the MOM [60] are grid or mesh-based techniques. In those methods, a solution domain is discretized with finite cells or elements such as cuboids, tetrahedra, rectangles, or triangles. Edges of the cells or elements lead to grid or mesh lines and intersections of the grid or mesh lines form grid points or nodes. As a result, connection relationships among the nodes are pre-defined due to placements of the cells or elements. And adaptive gridding or mesh refining in a sub-region of the solution can become difficult and time-consuming since the relationship among the nodes has to be addressed or redefined through rearrangement of the cells or elements.

To mitigate the above problem, meshless methods, such as the element-free Galerkin method [61], the moving least square reproducing kernel method [62], the smoothed particle electromagnetic method [29] and the RPIM method [28] were successfully developed to solve electromagnetic problems. In particular, a three dimensional RPIM method for transient electromagnetics was recently developed in [31] and an unconditionally stable version of RPIM method was proposed in [32]. However, in these methods, dual sets of nodes (*E*-nodes for electric fields and *H*-nodes for magnetic fields) are needed and which are spatially interlaced due to coupling nature of the electric and magnetic fields. Such an interlaced placement of the *E*- and *H*-nodes poses a challenge in implementation of the meshless methods. This is because they have to be properly positioned to correctly reflect the coupling relationship between electric and magnetic fields. Usually, the *E*-nodes are first placed in a structure to be modeled and then the *H*-nodes are generated through Voronoi tessellation [63]. For large and complex structures, this node generation process can become quite time-consuming.

In this chapter, a node collocating time-domain three-dimensional RPIM method for transient analysis of EM problems is proposed. Here, instead of solving coupled Maxwell's equations directly, the wave equations are solved with only the *E*-nodes at which all three electric fields can be collocated. The point interpolation based on the local RBF is employed. As only one set of nodes is dealt with for solutions of the wave equations, the proposed collocated time-domain RPIM method not only reduces implementation complexity but also improves modeling efficiency, in comparison to other meshless methods [28, 29, 31, 32, 61, 62]. Several aspects of the proposed method are then discussed in this chapter.

3.3 The Proposed Meshless Method for the Wave Equation

A linear, non-dispersive and isotropic media with permittivity ε and permeability μ, in a homogenous source free region is considered. The time-domain vector wave equation for the electrical field is

$$c^2\nabla^2\mathbf{E}-\frac{\partial^2\mathbf{E}}{\partial t^2}=0\,, \tag{3.1}$$

where $c^2 = \frac{1}{\mu\varepsilon}$. They may be expanded into three scalar wave equations with respect to each electric field component. Take E_x field as an example, we have

$$\frac{\partial^2 E_x}{\partial t^2} = c^2\left(\frac{\partial^2 E_x}{\partial x^2} + \frac{\partial^2 E_x}{\partial y^2} + \frac{\partial^2 E_x}{\partial z^2}\right). \tag{3.2}$$

Since only E_x component is the quantity to be solved in (3.2), one set of the electric field nodes (*E*-nodes) is required to be spatially defined in the solution domain. In this work, the *E*-nodes are defined in the way similar to that used in the point-matched time-domain finite-element method [64].

To obtain the numerical solutions of equation (3.2), the electric fields are approximated in terms of the shape functions,

$$E_\xi = \mathbf{\Phi}\mathbf{E}_{\mathbf{s}\xi}, \tag{3.3}$$

where ξ=*x, y* and *z*, and $\mathbf{\Phi}$ is the shape function vector associated with the nodes in a local support domain with the dimension of $1\times N$ (where N is the number of *E*-nodes in a local support domain). $\mathbf{E}_{\mathbf{s}\xi}$ are the unknown field value vector at each scattering nodes to be found with dimension $N\times 1$. The shape function vector can be expressed as $\mathbf{\Phi} = [\varphi_1 \quad \varphi_2 \quad \cdots \quad \varphi_n]$, where $\mathbf{\Phi} = \mathbf{B}\mathbf{A}^{-1}$ with

$$\mathbf{A} = \begin{bmatrix} \phi(\|\mathbf{R}_1 - \mathbf{R}_1\|) & \phi(\|\mathbf{R}_1 - \mathbf{R}_2\|) & \cdots & \phi(\|\mathbf{R}_1 - \mathbf{R}_n\|) \\ \phi(\|\mathbf{R}_2 - \mathbf{R}_1\|) & \phi(\|\mathbf{R}_2 - \mathbf{R}_2\|) & \cdots & \phi(\|\mathbf{R}_2 - \mathbf{R}_n\|) \\ \vdots & \vdots & & \vdots \\ \phi(\|\mathbf{R}_n - \mathbf{R}_1\|) & \phi(\|\mathbf{R}_n - \mathbf{R}_2\|) & \cdots & \phi(\|\mathbf{R}_n - \mathbf{R}_n\|) \end{bmatrix} \tag{3.4}$$

and $\mathbf{B}$ is the vector of radial basis functions, where $\mathbf{B} = \left[B_1(\|\mathbf{R} - \mathbf{R}_1\|) \quad \cdots \quad B_n(\|\mathbf{R} - \mathbf{R}_n\|)\right]$. Gaussian function is selected as the radial basis function $\phi(\|\mathbf{R} - \mathbf{R}_i\|)$ since it is claimed

to have better performance than other types of functions, such as multiquadric (MQ) function, for derivative involved interpolation [65]. $\phi\left(\|\mathbf{R}-\mathbf{R}_i\|\right)$ is expressed in general as

$$\phi\left(\|\mathbf{R}-\mathbf{R}_i\|\right)=e^{-pr^2}, \tag{3.5}$$

where $r=\|\mathbf{R}-\mathbf{R}_i\|=\sqrt{(x-x_i)^2+(y-y_i)^2+(z-z_i)^2}$ is the Euclidean distance between point $\mathbf{R(x,y,z)}$ and $\mathbf{R}_i$ is the center of the ith node position and p is the shape parameter that controls the decaying rate of Gaussian function.

Figure 3.1 shows the normalized interpolation error through MQ and Gaussian function to interpolate the first order of $f=x^2/\left(8+x^5\right)$. For MQ, q equal to 0.5. It is found that for the Gaussian indeed have better accuracy than MQ function.

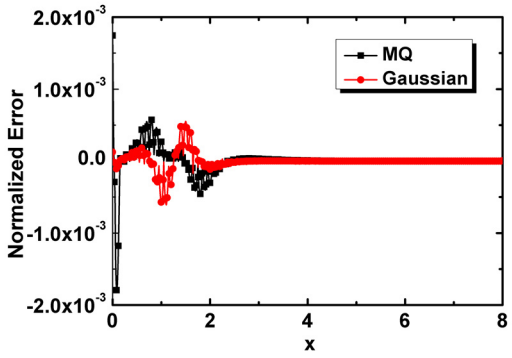

Figure 3.1Normalized error for MQ and Gaussian function.

Once the shape function is defined, the second order partial derivatives can be analytically found as

$$\frac{\partial^2\mathbf{\Phi}}{\partial\kappa^2}=\frac{\partial^2\mathbf{B}}{\partial\kappa^2}\mathbf{A}^{-1}. \tag{3.6}$$

With the time derivatives approximated by its second-order central finite-difference counterpart, the wave equation (3.2) can then be reformulated and solved for E_x with the following node-based time-marching meshless formulation:

$$E_x^{n+1} = 2E_x^n - E_x^{n-1} + \Delta t^2 c^2 \left(\sum \frac{\partial^2 \varphi_k}{\partial x^2} + \sum \frac{\partial^2 \varphi_k}{\partial y^2} + \sum \frac{\partial^2 \varphi_k}{\partial z^2} \right) E_x^n . \tag{3.7a}$$

By applying the similar procedure to the other two electric field components, we can obtain:

$$E_y^{n+1} = 2E_y^n - E_y^{n-1} + \Delta t^2 c^2 \left(\sum \frac{\partial^2 \varphi_k}{\partial x^2} + \sum \frac{\partial^2 \varphi_k}{\partial y^2} + \sum \frac{\partial^2 \varphi_k}{\partial z^2} \right) E_y^n \tag{3.8b}$$

$$E_z^{n+1} = 2E_z^n - E_z^{n-1} + \Delta t^2 c^2 \left(\sum \frac{\partial^2 \varphi_k}{\partial x^2} + \sum \frac{\partial^2 \varphi_k}{\partial y^2} + \sum \frac{\partial^2 \varphi_k}{\partial z^2} \right) E_z^n . \tag{3.8c}$$

The above equations form the time-marching formulations of the proposed meshless method. Δt is the time step. Note that the three electric field components, E_x^{n+1}, E_y^{n+1} and E_z^{n+1}, can be collocated at every node.

3.4 Implementation of Source and Boundary Conditions

The time-marching formulations (3.8) are for the source-free regions. For a region with current sources, additional terms will be present on the right-hand side of (3.8) as described below. After that, we will indicate how boundary conditions are implemented.

A. Sources Implementation

When current sources or excitations are present, the vector wave equations can be found as:

$$\frac{\partial^2 \mathbf{E}}{c^2 \partial t^2} = \nabla^2 \mathbf{E} - \nabla \left(\nabla \cdot \mathbf{E} \right) - \mu_0 \partial_t \mathbf{J} , \tag{3.9}$$

where **J** is the current density.

It can be seen that (3.9) cannot be expanded into a decoupled wave equation like (3.2) due to the nonzero divergence of the electric field on the right hand side of (3.9). There are two additional terms on the right hand side of (3.9) in comparison with (3.2) (this is for a source-free region). Fortunately, if we apply the central finite-difference scheme to the left hand side of (3.9) at the *n*th time step, these two additional terms are of the *n*th time step which are known. In fact, all the terms on the right hand side of (3.9) are of the *n*th time step which are known. Take the E_x as an example. Application of the finite difference to (3.9) leads to:

$$\begin{aligned} E_x^{n+1} &= 2E_x^n - E_x^{n-1} \\ &\quad + \Delta t^2 c^2 \left(\sum \frac{\partial^2 \varphi_k}{\partial x^2} + \sum \frac{\partial^2 \varphi_k}{\partial y^2} + \sum \frac{\partial^2 \varphi_k}{\partial z^2} \right) E_x^n \\ &\quad - \Delta t^2 c^2 \left(\sum \frac{\partial^2 \varphi_k}{\partial x^2} E_x^n + \sum \frac{\partial^2 \varphi_k}{\partial x \partial y} E_y^n + \sum \frac{\partial^2 \varphi_k}{\partial x \partial z} E_z^n \right) \\ &\quad - \Delta t^2 c^2 \left(\partial_t J_x \right)^n \end{aligned} . \tag{3.10}$$

As seen, all the terms on the right hand side of (3.10) are the known values of the *n*th and (*n-1*)th time steps and they can be computed and used to predict the new E_x of the (n+1)th time step. In other words, the proposed method can be simply applied to either a source region or a source-free region with or without the known additional terms, respectively.

B. Boundary Conditions Implementations

Since three electric components are co-located at every node, boundary conditions need to be carefully handled. In this chapter, the application of boundary conditions is simplified by only considering 3D cavity and resonator structures of regular geometry. In addition, only the E_z component is excited with the current source. For more general applications of the boundary conditions, the approach presented in [66] for the treatment of dielectric interfaces may be adapted.

3.5 Stability Analysis

Since the proposed meshless method is an explicit time-marching scheme, it is conditionally stable. To derive its stability condition, the Z transform technique [67] is applied to (3.7), and the marching equation in the **Z**-domain is obtained:

$$c^2\Delta t^2\mathbf{T}\cdot\mathbf{E} = z^{-1}\left(z-1\right)^2\mathbf{E}\,, \tag{3.11}$$

where $T_{ij} = \nabla^2\sum\Phi_{E_{ij}}$ and **E** is the unknown coefficient vector of interest in the **z**-domain.

Suppose λ is the eigenvalue of matrix $c_0^2\Delta t^2\mathbf{T}$ which embodies node location information and material properties. Then from (3.11), we have

$$\left(z-1\right)^2 - \lambda z = 0\,, \tag{3.12}$$

where (3.12) is the characteristic equation [67]. To ensure the stability of the proposed meshless method, all the root of (3.12) should be located on or within the unit circle. In other words, the absolute upper bound of λ (denoted as $|\lambda_{\max}|$), will lead to a relation between the spatial discretization and maximum time step that has to be satisfied to ensure the stability.

Mathematically, the following condition can be derived from (3.11):

$$\Delta t \le \frac{\sqrt{|\lambda_{\max}|}}{c\sqrt{\rho(\mathbf{T})}}\,, \tag{3.13}$$

where $\rho(\mathbf{T})$ is the spectral radius of **T**.

For homogeneous media, $|\lambda_{\max}| = 4$ can be found from (3.12). Therefore, all temporal steps in the proposed meshless method should satisfy the following condition:

$$\Delta t \le \frac{2}{c\sqrt{\rho(\mathbf{T})}}. \tag{3.14}$$

3.6 Numerical Examples and Discussion

In this section, two numerical experiments are presented to evaluate the accuracy and efficiency of the proposed meshless method. The conformal and multi-scale modeling

capabilities of method are also demonstrated.

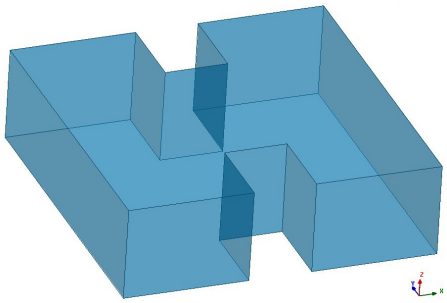

Figure 3.2 Geometry of the H-shaped cavity

A. H-Shaped Cavity

The first numerical example is an air-filled H-shaped cavity with perfect electric conducting walls. The computational domain is of 1 λ × 1 λ × 0.3 λ (scaled at 3 GHz) as shown in Figure 3.2. The cavity was discretized with non-uniformly distributed *E*-nodes as depicted in Figure 3.3. The node density in the central region is 1.5 times of that of the remaining region where the smallest distance between the nodes is $\lambda/20$. The shape parameter p was chosen as 10. The cavity was excited with a modulated differential Gaussian pulse with function of $\left((t-t_c)/t_w\right)e^{-\left((t-t_c)/t_w\right)^2}\sin\left[2\pi f\left(t-t_c\right)\right]$ where t_c = 0.33 *ns*, t_w = 1.33 *ns* and f = 3.5 GHz. It is placed at one end of the cavity. Thus, the bandwidth of the excitation (or source) is 6 GHz. The observation point is placed at the other end as shown Figure 3.3 (a). Only E_z component was excited and the modes having the E_z component were simulated.

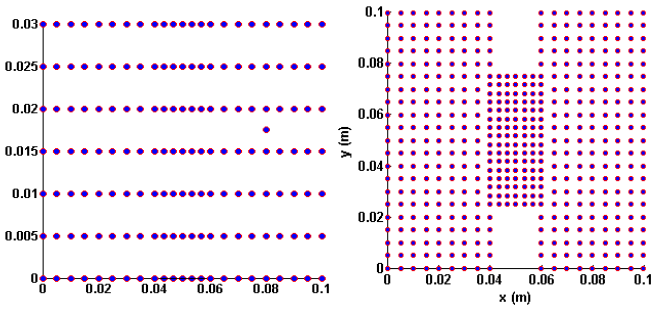

(a) (b)

Figure 3.3 Non-uniform nodal distribution within the H-shaped cavity resonator with the smallest distance between two nodes being $\lambda/20$

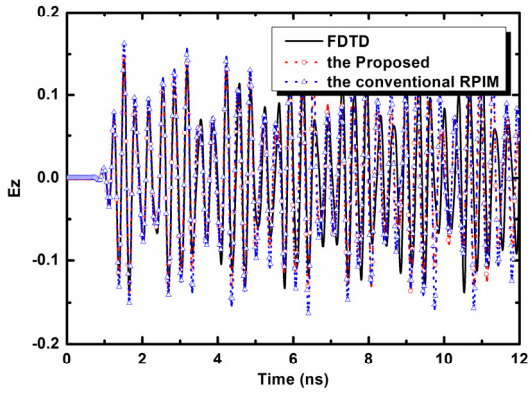

Figure 3.4 The E_z component in the time domain obtained with the proposed meshless method for the wave equation and the conventional RPIM method for the first order Maxwell's equation with non-uniform nodal distribution and the FDTD method with the uniform fine grid size of $\lambda/40$.

The simulated electric fields recorded at the observation point in the time and frequency domain with a time step equal to the maximum FDTD time step of 7.18 *ps* are plotted in Figure 3.4 and Figure 3.5. The results obtained from the conventional RPIM method (solving Maxwell's equations and using the same E-node distribution) and the results obtained with the conventional FDTD method (using a grid size of λ/40) are also shown for comparisons. It can be seen that the results obtained with the proposed meshless method agree well with the conventional FDTD method with some small differences in the late time of the simulation. For the conventional RPIM method, it has larger differences from the FDTD results than the proposed method. In the frequency domain, the resonant frequencies obtained from the conventional RPIM method show a small frequency shift towards higher frequency regions. However, the results from the proposed method are not visibly distinguishable from those of the FDTD method (as shown Figure 3.5). In other words, the above-mentioned differences of the time-domain results between the proposed method and the FDTD method are those of high-frequency components that fall outside the frequency range of interest. The reason for this differences is that modelling accuracy of three methods are different. At high frequency region the current discretization is not accurate enough to capture electromagnetic behaviors and they shows different level of errors. The proposed meshless method has a similar level of accuracy to the FDTD method but uses coarser grids.

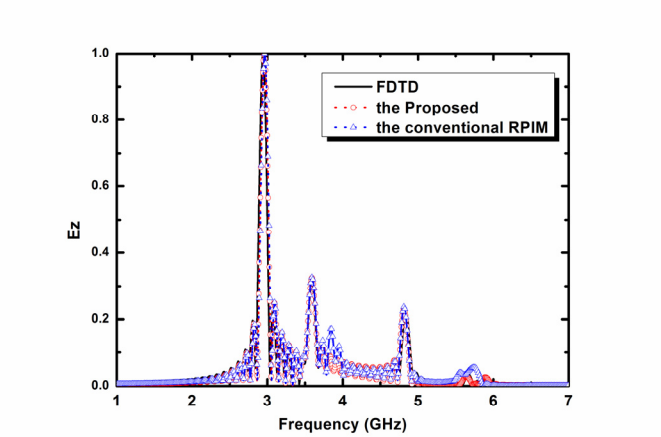

Figure 3.5 The E_z component in the frequency domain obtained with the proposed meshless method and the FDTD method with the uniform fine grid size of $\lambda/40$.

Table 3.1 lists the total number of unknowns and computational time with the proposed meshless method, the FDTD method and the conventional RPIM method. Note that the computational time for the meshless method includes that for constructing the shape functions. We find that number of unknowns with the proposed method is only 1/4.6 that of the conventional RPIM method. The computation time is only 1/8.3 that of the conventional RPIM method. We can also see that the proposed method can achieve the same accuracy with higher efficiency compared with the conventional RPIM method.

Table 3-1 Comparison of the time and memory used by the proposed meshless method, the FDTD method and the conventional RPIM method

Method	Discretization	unknowns	Preprocessing time (s)	Total time (s)
Proposed Meshless Method	Nodal spacing of λ/20 (min) λ/30 (max)	3722	0.79	0.90
RPIM	Nodal spacing of λ/20 (min) λ/30 (max)	17211	6.31	7.50
FDTD	Uniform Grid size: λ/20	14996	1.19	1.59
	Uniform Grid size: λ/40	111712	35.64	38.79
Ratio	To FDTD Grid size λ/20	4	1.5	1.8
	To FDTD Grid size λ/40	30	45	43
	To RPIM	4.6	8	8.3

In reference to the FDTD simulations with $\lambda/40$ and $\lambda/20$, respectively, the number of unknowns required with the proposed method is about 1/30 and 1/4 of that of the FDTD method, respectively. There are two reasons for it: (a) *E*-field nodes are collocated at the same point in the proposed method due to the decoupled nature of the wave equations, and (b) the conformal modeling and multi-scale capabilities of the meshless method allow easy or adaptive discretization refinement of a structure. Due to the smallest number of unknowns of the proposed method compared with the FDTD method and the RPIM method, the efficiency of the proposed method is the highest among the three methods.

Table 3-2 Comparison of the computational error of the FDTD method with different discretization and the proposed method

Method	Discretization	First resonance frequency (GHz)	Error (%)
FDTD	λ/20	2.960	0.78
	λ/40	2.943	0.20
	λ/80	2.937	0.00 (ref.)
Proposed Meshless Method	Nodal spacing of λ/20, λ/30	2.945	0.27

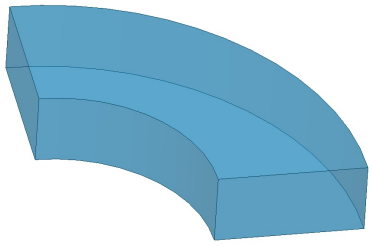

Figure 3.6 Geometry of the quarter ring resonator

Table 3.2 shows the errors of the first resonant frequency calculated by the FDTD method with $\lambda/20$, $\lambda/40$ and $\lambda/80$ and the proposed meshless method with non-uniform node distribution. In the Table, the result from the FDTD method with $\lambda/80$ is selected as the reference solution. It is found that all errors are quite small for both the FDTD method with different discretization and the proposed method. However, the errors of both the proposed method and the FDTD method $\lambda/40$ are around 0.2%. In other words, the proposed method can achieve the same accuracy level as the FDTD method with $\lambda/40$ but with less dense node distribution. That is the main reason that we have chosen the FDTD method with $\lambda/40$ for comparisons with the proposed method.

B. Quarter Ring Resonator

An air-filled quarter ring resonator was simulated to further demonstrate the conformal and multiscale modeling capabilities of the proposed meshless method. The inner and outer radii are 0.6 λ and 1.2 λ and the height of the resonator is 0.3 λ (scaled at 3 GHz). Figure 3.6 shows the geometry of the quarter ring resonator. The nodal distribution is depicted in Figure 3.7. As can be seen, a radial node distribution pattern is applied here: the nodes are denser close to the inner conducting wall and coarser towards the outer conducting wall. The cavity is excited with a Gaussian pulse of $E_z = e^{-((t-t_c)/t_w)^2} \sin\left[2\pi f\left(t-t_c\right)\right]$ where t_c = 0.33 *ns*, t_w = 1.33 *ns* and f = 3 GHz. The excitation is located at the center of the cavity with the band width of 6 G*Hz*.

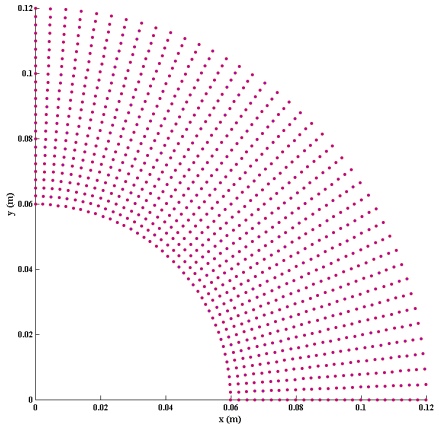

Figure 3.7 Node distribution of the quarter ring resonator cavity

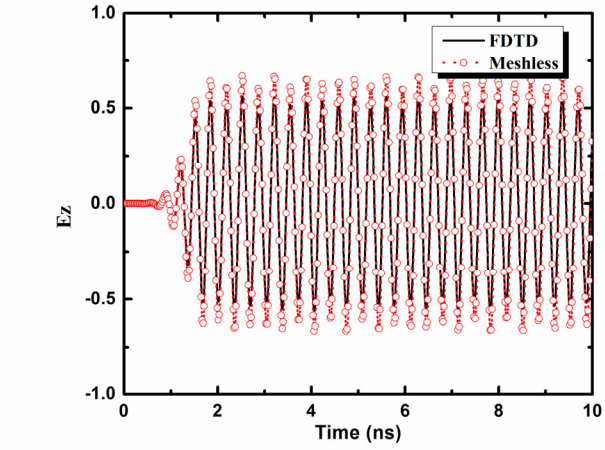

Figure 3.8 E_z component in the time domain obtained with the proposed meshless method and the FDTD method with the fine grid size of λ/40.

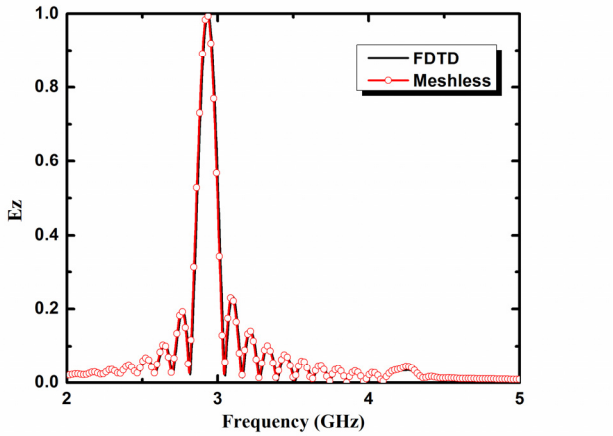

Figure 3.9 E_z component in the frequency domain obtained with the proposed meshless method and the FDTD method with the fine grid size of $\lambda/40$.

The electric fields obtained from the proposed meshless method and the FDTD method in both time and frequency domains at the observation point are plotted in Figure 3.8 and Figure 3.9. The number of the unknowns and the computational time for both methods are shown in Table 3.3. Again, good agreements between the results obtained with the proposed method and the FDTD method are observed.

Table 3-3 Comparison of the time and memory used by the proposed meshless method and the FDTD method

Method	Discretization	Unknowns	Preprocessing time (s)	Total time(s)
Proposed Meshless Method	Nodal spacing of $\lambda/40$ in the radial direction	13325	9.64	10.09
FDTD	Uniform Grid size: $\lambda/40$	128067	45.97	48.80
Ratio	to FDTD Grid size $\lambda/40$	9.6	4.8	4.8

3.7 Conclusion

In this chapter, a time-domain meshless collocation-RPIM method based on the local radial basis function is formulated and presented for solutions of time-domain electromagnetic wave equations. As all the electric (and magnetic) field can be collocated at every node, the proposed method is easy to implement and has high computational

efficiency. The stability analysis shows the proposed method is computationally stable under the same criterion of the conventional RPIM method. With the ease of nodal distribution, the conformal and multi-scale modeling capabilities of meshless methods can now be further exploited.

Chapter 4 The Divergence Free Meshless Methods for Electromagnetics Analysis

This chapter is mainly based on our published paper [44], which is Shunchuan Yang, Zhizhang (David) Chen, Yiqiang Yu, and Sergey Ponomarenko, "A divergence-free meshless method based on the vector basis function for transient electromagnetic analysis," published in IEEE Transactions on Microwave Theory and Techniques, vol. 62, pp. 1409 - 1416, 2014.

4.1 A Divergence Free Meshless Method for the Maxwell's Equations

4.1.1 Abstract

Although meshless methods, in particularly those with scalar RBFs, have been applied effectively to solve electromagnetic problems, their solutions may not be always divergence free in source-free regions, resulting in possibly large errors. In this section, a new vector RBF based meshless method, which is divergence free, is proposed for solving transient electromagnetic problems. Its divergence properties are investigated and compared with those of scalar RBFs; and they are further verified with numerical examples that present good accuracy.

4.1.2 Introduction

Many meshless methods are proposed to solve the electromagnetic problems due to their multi-scale and conformal modelling capability. They include the scalar RBF method [27], the RPIM [28], the smoothed particle meshless method [29], and the edge-based smoothed PIM [30]. Especially, a three dimensional RPIM was proposed in [31] and an unconditionally stable RPIM was presented in [32]. For most of these meshless methods, only spatial node information is needed to formulate electromagnetic problems. No connection information or grid lines among nodes are required. As a result, no re-arrangements of grid lines are required when a structure is modified partially. However, [33] demonstrates the existence of spurious modes in the traditional RPIM.

In a continuous domain, electromagnetic fields observe the divergence property: magnetic fields are always divergence free and so are electrical fields in charge free regions. When numerical methods are developed for solving electromagnetic problems, this

divergence property may not be preserved numerically and spurious numerical solutions may emerge [24]. Indeed, it has been found that the original meshless method does not always have this divergence-free property; spurious solutions exist in the solutions obtained.

On the other hand, divergence-free RBFs were developed for non-electromagnetic applications. A matrix-valued RBF, which is termed as the vector RBF in difference from the scalar RBF, was proposed and proven theoretically divergence free [68]. More work along this line was presented in [34, 35, 68]. In particular, the divergence-free vector RBF was successfully applied to Navier-Stokes equation [68] and astrophysical magneto-hydrodynamics (MHD) [69]. However, to the best knowledge of the authors, no reports were seen to apply the vector RBFs to computational electromagnetics and little has been addressed on divergence properties of numerical methods that solve electromagnetic problems.

In this section, we propose a meshless method incorporated with the above vector RBF for transient electromagnetic analysis. The proposed meshless method is theoretically proven to be divergence free in a source free region. Therefore, no artificial charges or spurious solutions will be present in the solutions of the meshless methods, making them more accurate.

4.1.3 The Original Scalar RBF Meshless Method

In order to better understand the vector RBFs, we first give a brief introduction to the conventional scalar RBF meshless method in this section.

The scalar RBF method was introduced to solve partial differential equations by Ed Kansa [70, 71]. Consider an unknown function $f(\mathbf{R})$ that is interpolated with the function values at the discretized scattering points of $\mathbf{R}_j$ in a solution domain. $f(\mathbf{R})$ can then be approximated by the RBF as follows:

$$f(\mathbf{x}) = \sum_{j=1}^{N} \phi\left(\left\|\mathbf{R}-\mathbf{R}_j\right\|\right) a_j \tag{4.1}$$

where $\phi\left(\left\|\mathbf{R}-\mathbf{R}_j\right\|\right)$ is the radial basis function, $\mathbf{R}=(x,y,z)$ is the location of the point of

interest, $\mathbf{R}_j = (x_j, y_j, z_j)$ is the location of node *j*, *N* is the number of nodes in a local support domain and a_j are the unknown expansion coefficients. Several different types of RBFs can be used in (4.1). We select Gaussian function as the scalar RBF in this section. Its formulation can be expressed as

$$\phi_j = \phi(\|\mathbf{R} - \mathbf{R}_j\|) = e^{-pr^2} \tag{4.2}$$

where $r = \|\mathbf{R} - \mathbf{R}_j\|$ is the Euclidean distance between the point of interest and node *j*, and *p* is the shape parameter that controls the decaying rate of the basis function.

To find the unknown expansion coefficients, (4.1) is enforced to pass through all the nodes within a local support domain. Then, a set of linear equations corresponding to the nodes is obtained and it can be rewritten in the compact matrix form below:

$$\mathbf{A} \cdot \mathbf{a} = \mathbf{f} \tag{4.3}$$

where $f_s = [f_1 \quad f_2 \quad \cdots \quad f_N]^T$ with f_i being the value of function f at node i. $a = [a_1 \quad a_2 \quad \cdots \quad a_N]^T$ and

$$\mathbf{A} = \begin{bmatrix} \phi(\|\mathbf{R}_1 - \mathbf{R}_1\|) & \phi(\|\mathbf{R}_1 - \mathbf{R}_2\|) & \cdots & \phi(\|\mathbf{R}_1 - \mathbf{R}_N\|) \\ \phi(\|\mathbf{R}_2 - \mathbf{R}_1\|) & \phi(\|\mathbf{R}_2 - \mathbf{R}_2\|) & \cdots & \phi(\|\mathbf{R}_2 - \mathbf{R}_N\|) \\ \vdots & \vdots & & \vdots \\ \phi(\|\mathbf{R}_N - \mathbf{R}_1\|) & \phi(\|\mathbf{R}_N - \mathbf{R}_2\|) & \cdots & \phi(\|\mathbf{R}_N - \mathbf{R}_N\|) \end{bmatrix} \tag{4.4}$$

Since **A** is always invertible (as (4.2) is selected as the RBF [72]), expansion coefficients q_i can be obtained by inverting **A**. Substitution of q_i into (4.1) leads to

$$f = \mathbf{B}\mathbf{A}^{-1}\mathbf{f}_s = \mathbf{\Phi}\mathbf{f}_s \tag{4.5}$$

where $\mathbf{B} = \mathbf{B}\left(\|\mathbf{R} - \mathbf{R}_j\|\right)$ contains the RBFs, $\mathbf{\Phi} = \left[\Phi_1 \quad \Phi_2 \quad \cdots \quad \Phi_N\right] = \mathbf{B}\mathbf{A}^{-1}$ and $\Phi_i = \Phi_i\left(\|\mathbf{R} - \mathbf{R}_j\|\right)$ is the shape function associated with spatial node *i* (*i*= 1,2,…,*N*).

Since the shape function is a continuous function, its first order partial derivatives can be analytically obtained as

$$\frac{\partial \mathbf{\Phi}}{\partial \kappa} = \frac{\partial \mathbf{B}\left(\|\mathbf{R} - \mathbf{R}_i\|\right)}{\partial \kappa}\mathbf{A}^{-1}. \tag{4.6}$$

4.1.4 The Proposed Vector RBF Meshless Method

In this section, we propose the divergence-preserved meshless method with the vector RBFs presented in [34, 68] and then analytically prove the divergence properties of the method. We also examine other properties of the method.

A. The Proposed Vector-based RBF

Mathematically, a divergence free field, denoted as **u**, can always be expressed as the curl of another vector field, say **w**, as follows:

$$\mathbf{u} = \nabla \times \mathbf{w} \tag{4.7}$$

where $\nabla = \left[\frac{\partial}{\partial x}, \frac{\partial}{\partial y}, \frac{\partial}{\partial z}\right]^T$.

w is not unique in (4.7). Therefore, additional conditions are needed. One common choice is Coulomb gauge, $\nabla \bullet \mathbf{w} = 0$, which means that we can let **w** be the curl of a third vector function. In our case, we select the following form:

$$\mathbf{w}(\mathbf{x}) = \nabla \times \sum_{j=1}^{N} \phi\left(\mathbf{R} - \mathbf{R}_\mathbf{j}\right)\mathbf{A}_j \tag{4.8}$$

where ϕ is a preselected scalar basis function and $\mathbf{A}_j = \left(A_{jx}, A_{jy}, A_{jz}\right)^T$ is the unknown vector expansion coefficient to be determined. (4.8) forms the basis function expansion of the vector field **u**, and consequently, vector field **u** can be expressed as

$$\begin{aligned}\mathbf{u} &= \nabla \times \nabla \times \sum_{j=1}^{N} \phi\left(\mathbf{R}-\mathbf{R}_{\mathbf{j}}\right)\mathbf{A}_j \\ &= \left(-\Delta\mathbf{I}+\nabla\nabla^T\right)\sum_{j=1}^{N} \phi\left(\mathbf{R}-\mathbf{R}_{\mathbf{j}}\right)\mathbf{A}_j\end{aligned} \tag{4.9}$$

where **I** is the 3×3 identity matrix, and Δ is the Laplace operator which can be expressed as

$$\Delta = \begin{bmatrix} \frac{\partial^2}{\partial x^2}+\frac{\partial^2}{\partial y^2}+\frac{\partial^2}{\partial z^2} & & \\ & \frac{\partial^2}{\partial x^2}+\frac{\partial^2}{\partial y^2}+\frac{\partial^2}{\partial z^2} & \\ & & \frac{\partial^2}{\partial x^2}+\frac{\partial^2}{\partial y^2}+\frac{\partial^2}{\partial z^2} \end{bmatrix}. \tag{4.10}$$

Based on (4.9), we can then define the vector RBF $\mathbf{\Psi}_j$ related to node *j* and shape function $\mathbf{\Phi}$ as:

$$\mathbf{\Psi}_j = \left(-\Delta\mathbf{I}+\nabla\nabla^T\right)\phi_j, \tag{4.11a}$$

$$\mathbf{\Phi} = \mathbf{B}_v\mathbf{A}_v^{-1}\mathbf{u}_s \tag{4.11b}$$

and $\mathbf{u} = \sum_{j=1}^{N} \mathbf{\Phi}_j\mathbf{u}_j$ (4.11c)

where $\mathbf{B}_v$ contains the vector RBFs, $\mathbf{u}_s = \begin{bmatrix} .... & u_{jx} & u_{jy} & u_{jz} & \cdots \end{bmatrix}^T$, $\mathbf{u}_j = \begin{bmatrix} u_{jx} & u_{jy} & u_{jz} \end{bmatrix}^T$ and

$$\mathbf{A}_v = \begin{bmatrix} \mathbf{\Psi}\left(\|\mathbf{R}_1-\mathbf{R}_1\|\right) & \mathbf{\Psi}\left(\|\mathbf{R}_1-\mathbf{R}_2\|\right) & \cdots & \mathbf{\Psi}\left(\|\mathbf{R}_1-\mathbf{R}_N\|\right) \\ \mathbf{\Psi}\left(\|\mathbf{R}_2-\mathbf{R}_1\|\right) & \mathbf{\Psi}\left(\|\mathbf{R}_2-\mathbf{R}_2\|\right) & \cdots & \mathbf{\Psi}\left(\|\mathbf{R}_2-\mathbf{R}_N\|\right) \\ \vdots & \vdots & & \vdots \\ \mathbf{\Psi}\left(\|\mathbf{R}_N-\mathbf{R}_1\|\right) & \mathbf{\Psi}\left(\|\mathbf{R}_N-\mathbf{R}_2\|\right) & \cdots & \mathbf{\Psi}\left(\|\mathbf{R}_N-\mathbf{R}_N\|\right) \end{bmatrix}.$$

The dimension of $\mathbf{A}_v$ is $3N \times 3N$, where *N* is the number of the scattering nodes in a local support domain. Since the number of the nodes, *N,* in a local support domain is small, inversion of $\mathbf{A}_v$ can be done without much difficulty with modern computers.

Several observations can be made on the vector basis function of (4.11):

(a) The vector basis function can be constructed from the scalar RBF, ϕ_j, with a 3×3 matrix transform for each node *j* through (4.11a),

(b) ϕ_j can be any kind of basis function including RBF or Gaussian function;

(c) The shape function $\mathbf{\Phi}_j$ satisfies Kronecker's delta property; that is:

$$\mathbf{\Phi}_j = \begin{cases} \mathbf{I}, & \mathbf{R} = \mathbf{R}_j \\ \mathbf{0}, & \textit{at other nodes} \end{cases} \tag{4.12}$$

(d) Each row of $\mathbf{\Psi}_j$ is a vectorized basis function: the first row of $\mathbf{\Psi}_j$, or the first vector in the vector RBF, represents the *x* component, the second vector (row) the *y* component and the third vector the *z* component, respectively.

Expansion of (4.11) for each node reads:

$$\mathbf{\Psi}_j = \begin{bmatrix} -\partial_y^2 - \partial_z^2 & \partial_x \partial_y & \partial_x \partial_z \\ \partial_y \partial_x & -\partial_x^2 - \partial_z^2 & \partial_y \partial_z \\ \partial_z \partial_x & \partial_z \partial_y & -\partial_x^2 - \partial_y^2 \end{bmatrix} \phi_j . \tag{4.13}$$

The curl of $\mathbf{\Psi}_j$ can be found as:

$$\nabla \times \mathbf{\Psi}_j = \begin{bmatrix} 0 & -\partial_x^2 \partial_z - \partial_z^3 - \partial_y^2 \partial_z & \partial_x^2 \partial_y + \partial_y^3 + \partial_z^2 \partial_y \\ \partial_x^2 \partial_z + \partial_z^3 + \partial_y^2 \partial_z & 0 & -\partial_z^2 \partial_x - \partial_x^3 - \partial_y^2 \partial_x \\ -\partial_x^2 \partial_y - \partial_y^3 - \partial_z^2 \partial_y & \partial_z^2 \partial_x + \partial_x^3 + \partial_y^2 \partial_x & 0 \end{bmatrix} \phi_j . \tag{4.14}$$

For a two dimensional problem, fields are assumed constant in the *z* direction; therefore $\partial_z = 0$. The vector RBFs and their curl operation are much simplified. More specifically, we have:

$$\mathbf{\Psi}_j = \begin{bmatrix} -\partial_y^2 & \partial_x \partial_y & 0 \\ \partial_x \partial_y & -\partial_x^2 & 0 \\ 0 & 0 & -\partial_y^2 - \partial_x^2 \end{bmatrix} \phi_j \tag{4.15}$$

and

$$\nabla \times \boldsymbol{\Psi}_j = \begin{bmatrix} 0 & 0 & \partial_x^2 \partial_y + \partial_y^3 \\ 0 & 0 & -\partial_y^2 \partial_x - \partial_x^3 \\ -\partial_x^2 \partial_y - \partial_y^3 & \partial_y^2 \partial_x + \partial_x^3 & 0 \end{bmatrix} \phi. \tag{4.16}$$

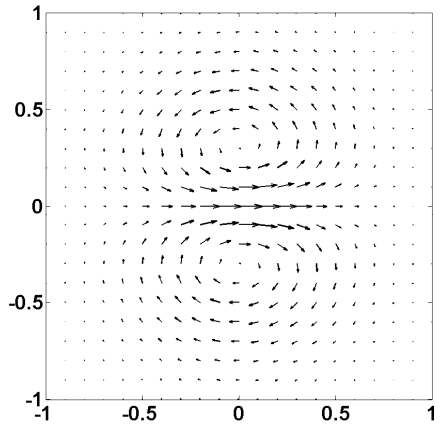

(a) The first vector

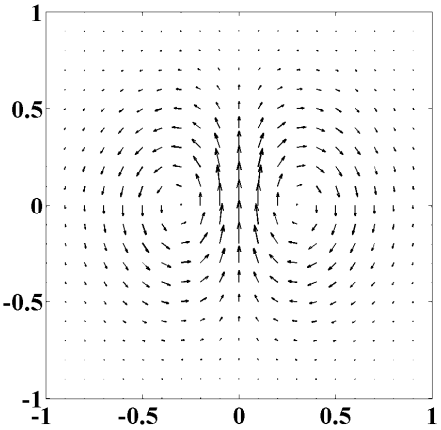

(b) The second vector

Figure 4.1 Plots of the vector RBF modes with $p = 5$.

Here the scalar radial basis function is chosen to be $\phi_j = \frac{1}{2p} e^{-p[(x-x_j)^2+(y-y_j)^2]}$, which results in

$$\Psi_{j11} = \left[2p\left(x - x_j\right)^2 - 1 \right] e^{-p\left[\left(x-x_j\right)^2+\left(y-y_j\right)^2\right]} \tag{4.17a}$$

$$\Psi_{j12} = 2p\left(x - x_j\right)\left(y - y_j\right) e^{-p\left[\left(x-x_j\right)^2+\left(y-y_j\right)^2\right]} \tag{4.17b}$$

$$\Psi_{j21} = \Psi_{j12} \tag{4.17c}$$

$$\Psi_{j22} = \left[2p\left(y - y_j\right)^2 - 1 \right] e^{-p\left[\left(x-x_j\right)^2+\left(y-y_j\right)^2\right]} \tag{4.17d}$$

$$\Psi_{j33} = \left[2p\left(x - x_j\right)^2 + 2p\left(y - y_j\right)^2 - 2 \right] e^{-p\left[\left(x-x_j\right)^2 + \left(y-y_j\right)^2\right]} \tag{4.17e}$$

To better understand the vector basis function, we plot a two dimensional vector RBF at $\boldsymbol{R}_j = [0\ 0]^T$ using (4.2) as the scalar basis function with p = 5 [16]. Figure 4.1 shows the vector RBF in the two dimensions. The first vector is the first row of (4.15) and the second vector is the second row of (4.15). It is easy to see that the two rows of the vector radial basis function present two mutually orthogonal dipole modes: Figure 4.1 (a) is the horizontal dipole mode and Figure 4.1(b) is the vertical dipole mode; rotation of one dipole leads to another. Obviously, both dipole modes are divergence free. Thus, the field expanded by them should be divergence free.

B. Divergence of the Proposed Vector RBF

Because $\boldsymbol{\Psi}$ is constructed from (4.7) and (4.8), its divergence should be zero as implied by (4.8). We can verify it by directly taking the divergence of the mth row of $\boldsymbol{\Psi}$:

$$\begin{aligned} \nabla \bullet \left(\boldsymbol{\Psi}_j \right)_m &= \nabla \bullet \left\{ \left(-\Delta \mathbf{I} + \nabla \nabla^T \right) \phi_j \right\}_m = \nabla \bullet \left\{ -\delta_{mn} \sum_{p=x,y,z} \frac{\partial^2}{\partial p^2} + \frac{\partial}{\partial k} \frac{\partial}{\partial l} \right\} \phi_j \\ &= \left\{ -\sum_{p=x,y,z} \frac{\partial^2}{\partial p^2} \frac{\partial}{\partial k} + \sum_{p=x,y,z} \frac{\partial^2}{\partial p^2} \frac{\partial}{\partial k} \right\} \phi_j \\ &= 0 \end{aligned} \tag{4.18}$$

where k and l stand for the other two directions in a Cartesian coordinate system rather than p, and m and n represents the mth row and nth column of $\boldsymbol{\Psi}_j$.

C. Divergence Properties of the Scalar RBF

In this section, we examine the divergence properties of the original meshless method that uses the scalar RBF. The field in the conventional meshless method is approximated as

$$u = \sum_{j=1}^{N} \phi_j \alpha_j = \sum_{j=1}^{N} \phi\left(\mathbf{R} - \mathbf{R}_\mathbf{j}\right) \alpha_j \tag{4.19}$$

at each node. Assume that Gaussian function of (4.2) is used as the basis function ϕ. Then the divergence of the approximated field (4.19) can be found as

$$\nabla \bullet \mathbf{u} = -2pe^{-pr^2} \sum_{j=1}^{N} \left(x + y + z - x_j - y_j - z_j \right) a_j \,. \tag{4.20}$$

It is seen from (4.20) that the divergence of **u** is dependent on the position of the point of interest, the nodes, and the expansion coefficients. There is no guarantee that it will always be zero except for the certain point of interest and node distributions that make (4.20) zero. In other words, the divergence-free property is not warranted for the scalar RBF meshless method. This is not the case for the proposed vector RBFs since they constructed through (4.8) that ensures the divergence property.

4.1.5 The Proposed Meshless Formulations with the Vector RBF for Solving Electromagnetic Problems

With the definition of the vector basis function and vector shape function, electrical and magnetic vector field can be approximated as

$$\mathbf{E} = \sum_{i}^{NA} \mathbf{\Phi}_i \mathbf{E}_i \tag{4.21a}$$

$$\mathbf{H} = \sum_{i}^{NB} \mathbf{\Phi}_i \mathbf{H}_i . \tag{4.21b}$$

Consider Maxwell's equations in a linear, isotropic, non-dispersive, and lossless media of permittivity ε and permeability μ without sources,

$$\frac{\partial \mathbf{H}}{\partial t} = -\frac{1}{\mu} \nabla \times \mathbf{E} \tag{4.22a}$$

$$\frac{\partial \mathbf{E}}{\partial t} = \frac{1}{\varepsilon} \nabla \times \mathbf{H} . \tag{4.22b}$$

By substitution of (4.21) into (4.22), we have the following equations:

$$\frac{\partial \sum_{i}^{NB} \mathbf{\Phi}_i \mathbf{H}_i}{\partial t} = -\frac{1}{\mu} \nabla \times \sum_{j}^{NA} \mathbf{\Phi}_j \mathbf{E}_j \tag{4.23a}$$

$$\frac{\partial \sum_{i}^{NA} \mathbf{\Phi}_i \mathbf{E}_i}{\partial t} = \frac{1}{\varepsilon} \nabla \times \sum_{j}^{NB} \mathbf{\Phi}_j \mathbf{H}_j \tag{4.23b}$$

Now we choose the collocation method and apply it to the above equation; that is, we choose Dirac Delta function for the error testing or minimization [73]: test (4.23a) with Delta functions at magnetic field nodes and (4.23b) with Delta functions at electric field nodes. Because the Kronecker's Delta property of the vector shape function, we can then obtain the following equations:

$$\frac{\partial \mathbf{H_i}}{\partial t} = -\frac{1}{\mu} \nabla \times \sum_{j}^{NA} \mathbf{\Phi}_j \mathbf{E_j} \tag{4.24a}$$

$$\frac{\partial \mathbf{E_i}}{\partial t} = \frac{1}{\varepsilon} \nabla \times \sum_{j}^{NB} \mathbf{\Phi}_j \mathbf{H_j} \tag{4.24b}$$

When the central finite difference scheme is applied to (4.24) in time, the time-marching equation can be obtained:

$$\mathbf{H}_i^{n+1/2} = \mathbf{H}_i^{n-1/2} - \frac{\Delta t}{\mu} \sum_{j}^{NA} \nabla \times \mathbf{\Phi}_j \mathbf{E}_j^n \tag{4.25a}$$

$$\mathbf{E}_i^{n+1} = \mathbf{E}_i^n + \frac{\Delta t}{\varepsilon} \sum_{j}^{NB} \nabla \times \mathbf{\Phi}_j \mathbf{H}_j^{n+1/2} \tag{4.25b}$$

Note that the shape functions in the above equations are naturally divergence-free.

4.1.6 Numerical Examples and Discussion

In this section, a few numerical examples are presented to verify the divergence properties and accuracy of the proposed vector RBFs based divergence-free meshless method. They are elaborated below.

A. One Dimensional Resonator

One dimensional resonator with the perfect electrical conductor (PEC) walls at both ends was constructed. The length of the one dimensional cavity is 1 meter. The current source is located at the center and is specified as:

$$J_z = \cos(2\pi ft)\exp\left(-\left(\frac{t_c - t}{t_w}\right)^2\right) \tag{4.26}$$

where f = 1.5 GHz, t_w = 40 ns and t_c = 120 ns.

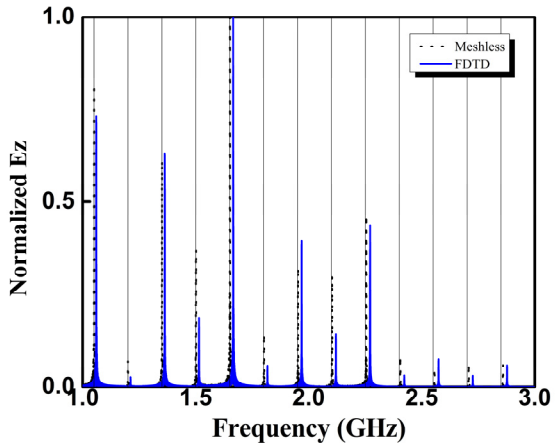

Figure 4.2 Resonance frequencies obtained with the proposed meshless method and the FDTD method. The vertical grey lines represent the analytical resonant frequencies.

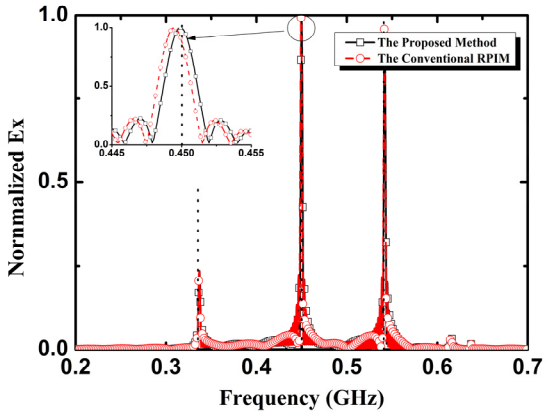

Figure 4.3 Resonance frequencies obtained with the proposed meshless method and the conventional RPIM. The vertical grey lines represent the analytical resonant frequencies.

Figure 4.2 shows the resonator frequencies obtained with the proposed meshless method and FDTD method. Both the uniform grid size for the FDTD method and the uniform node distance for the meshless method are 0.01 meter; it amounts to 10 cells or 10 spatial sampling points per wavelength at 3 GHz across the whole computation domain. The theoretical resonance frequencies are represented with the vertical lines in the figure. It can

be seen that the results obtained with the FDTD method have frequency shift towards higher frequency region even when 10 cells per wavelength is used at 3 GHz. However, the frequencies obtained with the proposed meshless method agree well with the theoretical results. In other words, the proposed meshless method has better accuracy than the FDTD method under the same discretization conditions. This may be attributed to the fact that the meshless method is essentially a high order method while the FDTD method expands the field quantity with the roof-top function [73].

B. The Cavity Without and With a Fin

A two dimensional cavity with dimensions of 100 cm by 100 cm is considered. A uniform node distance is taken to be 5 cm. Figure 4.3 shows the resonance frequencies obtained from the conventional RPIM and the proposed meshless method. The vertical dot lines indicate the theoretical results. Although the same node distribution was employed with the RPIM and the proposed meshless method, a small frequency difference from the theoretical results is observed at 0.45 GHz with the results obtained with the conventional RPIM. For the proposed meshless method, the results agree well with the theoretical results.

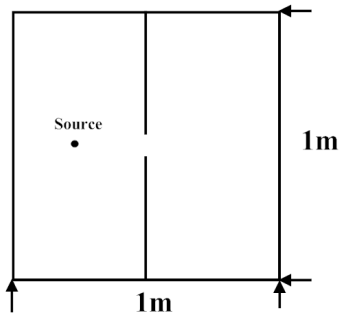

Figure 4.4 The geometry of the cavity with PEC screen located at the middle.

To verify the divergence properties of the proposed meshless method based on the vector RBFs, we considered an air-filled finned cavity with the dimensions of 100 cm by 100 cm as shown in Figure 4.4. It was then discretized with a uniform grid of 20 cells by 20 cells with the cell size of 5cm. Such a discretization arrangement amounts to 15 sampling points per wavelength at 0.4 GHz. The reason we chose the finned structure is that there should be strong charge accumulation at the edges of the fins and no charges are accumulated elsewhere. We can then evaluate the divergence property of the numerical methods in an effective way.

A point source of Gaussian pulse below was excited inside the cavity:

$$J_x = \cos(2\pi ft)\exp\left(-\left(\frac{t_c - t}{t_w}\right)^2\right) \tag{4.27}$$

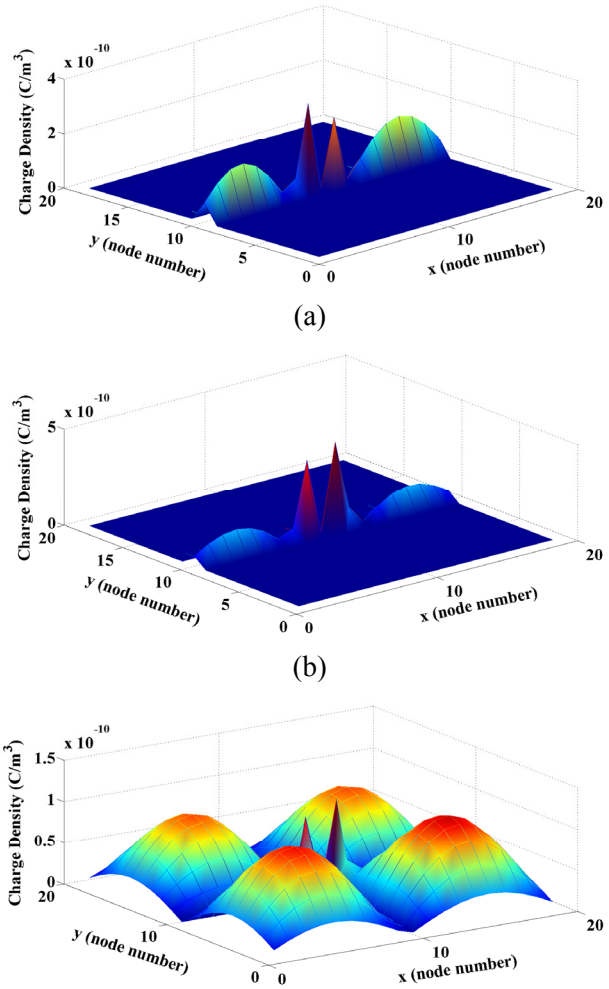

Figure 4.5 Charge density distribution obtained with the conventional FDTD method (a), the proposed meshless method based on vector RBFs (b) and the conventional meshless method based on the scalar RBFs (c) at time t = 50 *ns*.

where f = 0.4 GHz, t_w = 4 ns and t_c = 12 ns. The divergence of electric flux density, i.e, the charge density, was computed with the following formulas:

$$\rho = \nabla \cdot \varepsilon \mathbf{E} = \frac{\partial(\varepsilon E_x)}{\partial x} + \frac{\partial(\varepsilon E_y)}{\partial y}. \tag{4.28}$$

Figure 4.5 shows the charge densities computed with the FDTD method, the proposed vector RBF based meshless method and the conventional (or original) scalar RBF meshless method. We can find that the conventional RPIM does not retain the divergence-free condition. In the source free region, numerical spurious charges are introduced as shown Figure 4.5 (c) and they inevitably lead to inaccurate or even totally wrong simulation results. However, the charge distribution computed with the proposed RBF meshless method is similar to that computed with the FDTD method: at the PEC fins only, we can see the charge distribution which is expected due to the fin structure.

To further examine the divergence properties of the proposed method and the conventional RPIM, we also ran the simulations when the node distribution is not placed regularly for the finned structure (equivalent to a non-uniform situation): we slightly move the H-nodes off their original centers on the left side of the fin while the right side remains unchanged. The off-central displacement distance is 0.01 meter and the off-central direction can be randomly chosen in the positive or negative x axis. The node distributions are shown in Figure 4.6.

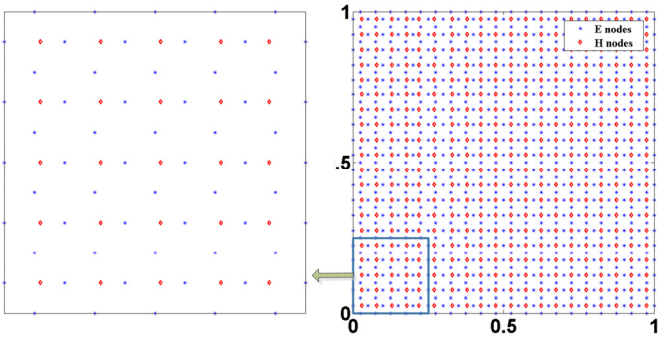

Figure 4.6 The node distribution: the left side of the central axis is nonuniform and the right side is uniform.

The charge density obtained with the conventional RPIM and the proposed method is presented in Figure 4.7. It is easy to find that the charge density obtained from the conventional RPIM does not maintain the divergence-free property in the source free region while the proposed method does. Another interesting observation is that in the left region, numerical spurious charge density is larger than that in the right region with the conventional RPIM. This is due to the fact that the nonuniform node distribution induces larger spurious charges as implied by (4.20). However, with the proposed method, spurious

charges are not present. It shows that the proposed method indeed guarantees divergence properties. In other words, numerical examples verify the theoretical analysis presented before.

It should be mentioned that the above results appear not in agreement with the numerical results presented in [33] on the stability issue. In our simulations, no monomial basis functions were used and p was chosen to be 10. They correspond to small values of $\alpha_c (= p \cdot d_c^2)$ which caused unstable solutions in the cases studied in [33]. However, we did run the simulations up to 1 million iterations and no instability of our solutions was observed. We can attribute the disagreement to the fact that the Gaussian RBF, in our cases, is not directly applied to interpolate or expand the field components but through the curl operation of (4.9) in order to achieve the divergence-free property. As a result, the numerical findings of [33] may not be the same as those presented in this section as they tend to be problem-dependent. Nevertheless, [33] does present valid and useful results in their cases, and we are currently investigating the stability issue and finding its solutions in an analytical way for meshless methods in general.

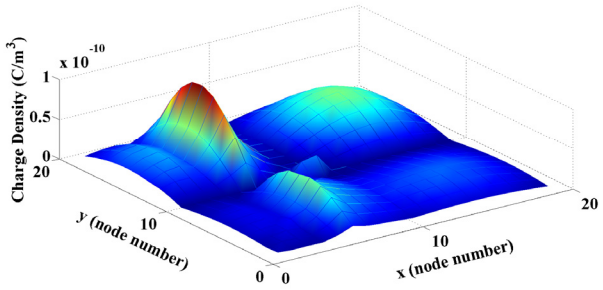

(a)

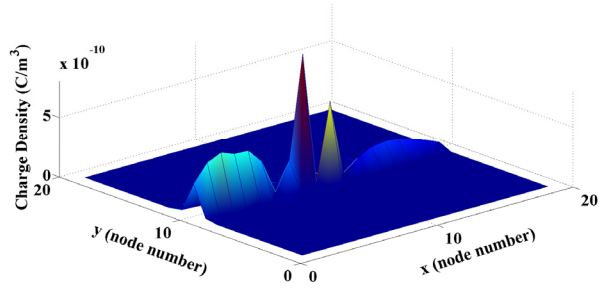

(b)

Figure 4.7 Charge density distribution obtained with the conventional RPIM (a) and the proposed method (b).

4.2. Divergence Free Meshless Method for the Wave Equation

4.2.1 Abstract

With the implementation of the vector RBF which is theoretically divergence free, we propose a meshless method for solving the transient vector wave equation. Unlike the conventional RPIM method that solves the electric field and magnetic field components separately with scalar wave equations, the proposed method solves the vector wave equation directly. Therefore, the long-existing technical challenge of the source and boundary implementation in the traditional RPIM method is alleviated due to the direct solution of the vector wave equation. In addition, the stability condition of the proposed method is also presented. At last, several numerical experiments are conducted to validate the accuracy and effectiveness of the proposed solver.

4.2.2 The Proposed Meshless Method for the Vector Wave Equations

Without losing the generality, we consider the general second-order vector wave equation for the electrical field in a lossless medium:

$$\nabla \times \frac{1}{\mu_r} \nabla \times \mathbf{E}(\mathbf{r},t) + \frac{\varepsilon_r}{c_0^2} \partial_t^2 \mathbf{E}(\mathbf{r},t) = -\mu_0 \partial_t \mathbf{J}(\mathbf{r},t) \tag{4.29}$$

where **E**(**r**,t) is the electrical field, **J**(**r**,t) is the current density, ε is permittivity of the medium, μ_0 is the permeability of the medium, μ_r is the relative permeability of the medium.

To obtain the numerical solution of (4.29), a solution domain is first discretized with spatial nodes pre-defined by users. Then, electric field **E**(**r**,t) is approximated in expansion with (4.21a).

Because of the vector nature of the proposed shape function (4.11), the curl operation upon the expanded fields can easily be obtained analytically after applying the curl operator to the vector shape function. The double curl of the electrical field in the wave equation is easy to be modelled through the vector radial basis function. Then, we have the following results

$$\nabla\times\nabla\times\boldsymbol{\Psi}_j=\left(\partial_x^2+\partial_z^2+\partial_y^2\right)\begin{bmatrix}\partial_y^2+\partial_z^2 & -\partial_x\partial_y & -\partial_x\partial_z\\ -\partial_x\partial_y & \partial_x^2+\partial_z^2 & -\partial_z\partial_y\\ -\partial_x\partial_z & -\partial_z\partial_y & \partial_x^2+\partial_y^2\end{bmatrix}\phi_j. \tag{4.30}$$

where $\boldsymbol{\Psi}_j$ is the vector RBF and ϕ_j is the scalar RBF, like Gaussian RBF.

When the variables in the *z* direction remain constant, (4.30) reduces to two dimensional cases and it is significantly simplified. The formulations can be read as

$$\nabla\times\nabla\times\boldsymbol{\Psi}_j=\left(\partial_x^2+\partial_y^2\right)\begin{bmatrix}\partial_y^2 & -\partial_x\partial_y & 0\\ -\partial_x\partial_y & \partial_x^2 & 0\\ 0 & 0 & \partial_x^2+\partial_y^2\end{bmatrix}\phi_j. \tag{4.31}$$

With the appropriate definition of the vector shape function and spatial placement of the nodes in the solution domain, we can solve the vector wave equation (4.29) with the proposed vector-based meshless method. By substituting (4.21a) into (4.29), we get the discretized vector wave equation

$$\nabla\times\frac{1}{\mu_r}\nabla\times\sum_i^N\boldsymbol{\Phi}_i\mathbf{E}_i+\frac{\varepsilon_r}{c_0^2}\partial_t^2\sum_i^N\boldsymbol{\Phi}_i\mathbf{E}_i=-\mu_0\partial_t\mathbf{J}. \tag{4.32}$$

To make (4.32) practical for computation, the collocation approach is applied to (4.32), which means that we test (4.32) with Dirac Delta function at node *i*. Due to the Kroneckor's delta property of the shape function, we obtain the semi-discretized formulation

$$\left(\nabla\times\frac{1}{\mu_r}\nabla\times\sum_j^N\boldsymbol{\Phi}_j\mathbf{E}_j\right)\Bigg|_{node_i}+\frac{\varepsilon_r}{c_0^2}\partial_t^2\mathbf{E}_i=-\mu_0\partial_t\mathbf{J}\Big|_{node_i}. \tag{4.33}$$

By applying the central finite difference in the time domain to (4.34), we reach the final time-marching formulation:

$$\mathbf{E}_i^{n+1}=2\mathbf{E}_i^n-\mathbf{E}_i^{n-1}-\frac{c_0^2\Delta t^2}{\varepsilon_r}\left(\nabla\times\frac{1}{\mu_r}\nabla\times\sum_j^N\boldsymbol{\Phi}_j\mathbf{E}_j^n\right)\Bigg|_{node_i}-\frac{\Delta t^2}{\varepsilon}\partial_t\mathbf{J}\Bigg|_{node_i}^n. \tag{4.34}$$

To make (4.34) more efficient for computation, we split and compute (4.34) in two steps

$$\mathbf{Q}_i^{n+1} = \mathbf{Q}_i^n - \frac{\Delta t^2}{\mu_0 \varepsilon}\left(\nabla \times \frac{1}{\mu_r} \nabla \times \sum_j^N \mathbf{\Phi}_j \mathbf{E}_j^n \right)\Bigg|_{node_i} - \frac{\Delta t^2}{\varepsilon} \partial_t \mathbf{J}\Big|_{node_i}^n , \tag{4.35a}$$

$$\mathbf{E}_i^{n+1} = \mathbf{Q}_i^{n+1} + \mathbf{E}_i^n , \tag{4.35b}$$

where **Q** is the intermediate vector introduced to speed up the computation.

(4.35) is a vector form that can be directly solved without the need to expand the Maxwell's equations into six scalar partial derivative equations for six field components as done with the conventional methods. In other words, with the conventional RPIM method based on the scalar RBFs and the FDTD method, the vector field equations need to be expanded into separate scalar wave equations and then numerical methods are adapted and applied to solve each of the scalar equations. This poses a technical challenge when the current source or charges are encountered; there, field components may be coupled at source points or charge locations. However, with the proposed meshless method based on the divergence-free vector RBFs, the issue will no longer exist since a source term is incorporated into the formulations and the wave equations are solved in a coupled vector manner.

Compared with the conventional time-domain FEM, the proposed meshless method is a node-based solver where only the spatial location of the nodes that discretize the solution domain is needed; in other words, the node-based property of the meshless methods is preserved including its capability of conforming and multi-scale modeling.

4.2.3 Stability Condition

Since the proposed meshless method employs explicit time-marching scheme, it is conditionally stable. We can obtain its stability condition based on the result presented in [67] for the proposed vector meshless method:

$$\Delta t \le \frac{\sqrt{\left|\lambda\right|_{\max}}}{c_0 \sqrt{\rho(\mathbf{T})}} \tag{4.36}$$

where λ is the eigenvalue of matrix $-\frac{\Delta t^2}{\mu_0 \varepsilon}\mathbf{T}$, $\rho(\mathbf{T})$ is the spectral radius of $\mathbf{T}$ whose element is $T_{ij} = \left(\nabla \times \frac{1}{\mu_r} \nabla \times \sum_j^N \mathbf{\Phi}_j \right)\Big|_{node_i}$. The node location and material information are embodied into $\mathbf{T}$. For homogeneous media, $|\lambda|_{\max} = 4$ can be obtained. Therefore, all temporal steps in the proposed meshless method should satisfy the following condition:

$$\Delta t \le \frac{2\varepsilon_r}{c_0 \sqrt{\rho(\mathbf{T})}}. \tag{4.37}$$

4.2.4 Numerical Examples and Discussion

In this section, we choose several numerical experiments to validate the accuracy and convergence properties of the proposed meshless method for the vector wave equations.

A. One dimensional Structure

Due to the existence of the analytical solutions of the one dimension cavity with PEC, we select it for the initial verification of the proposed method. The length of the cavity is 1 meter. The initial condition of the electric field is given as $E_z = \sin(k\pi x / L)$ and the region is source free. The theoretical field distribution is given as:

$$E_z = \cos(k\pi ct / L) \cdot \sin(k\pi x / L) \tag{4.38}$$

where k is the mode number and L is the length of the cavity.

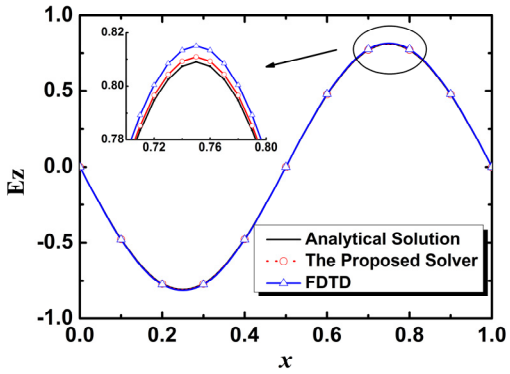

Figure 4.8 The E_z field value at 10 *ns*.

The nodes are selected uniformly distributed in the cavity with the distance between two neighboring nodes being 1 mm. The shape parameter p is selected as 10 and the average node number in each local support domain is 7. For comparison, the cavity was also

simulated with the FDTD with the uniform cell size of 1 *mm*. To reduce the effect of the time step on the accuracy, the time steps for the proposed meshless method and the FDTD method are selected small such that *CFLN* = 0.1, where *CFLN* is the ratio of the time step to the maximum time step allowable with the FDTD method.

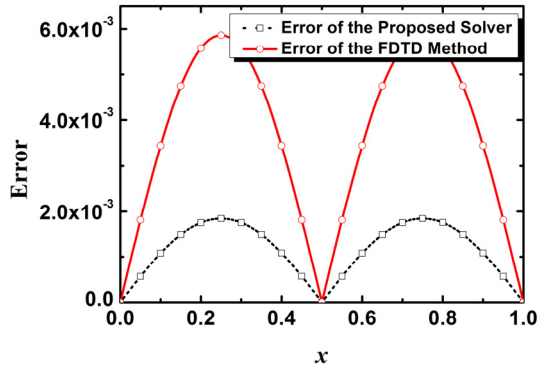

Figure 4.9 The absolute solution difference between the proposed method and the FDTD method.

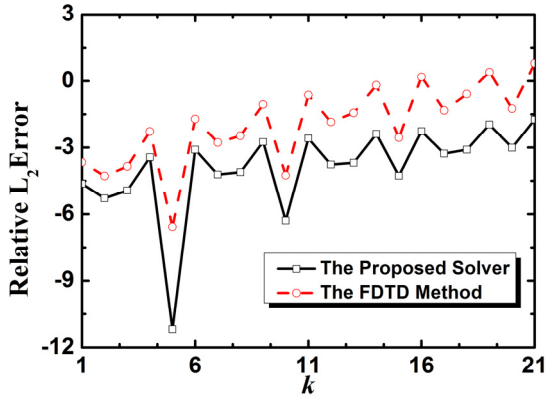

Figure 4.10 The relative L_2 error of the proposed solver and the FDTD method.

Figure 4.8 shows the field value obtained with the FDTD method and the proposed solver at 10 *ns*. Visible good agreements between the results obtained with the proposed method, the FDTD method and the analytical solution are observed. However, we can find that at the peak the proposed method achieves more accurate solution than that of the FDTD method. Figure 4.9 presents the absolute error between the numerical solutions and the analytical results. It confirms that the proposed method can obtain more accurate results than the FDTD method. At the peak the error of the proposed method is three times smaller than that of the FDTD method. Figure 4.10 illustrates the relative L_2 error; the L_2 error is computed with the equation below:

$$L = \log_{10}\left(\frac{\left\|\mathbf{E}^N - \mathbf{E}^A\right\|_2}{\left\|\mathbf{E}^A\right\|_2}\right) \tag{4.39}$$

where $\mathbf{E}^N$ is the numerical electrical field obtained with the FDTD method or the proposed method and $\mathbf{E}^A$ is the analytical field solution. The error of the two methods goes up as k increases. This is because the dispersion errors increase with mode number k when the spatial discretization remains unchanged. However, the accuracy of the proposed method is about two order higher than that of the FDTD method. The reason is that the meshless method is essentially a high order method and more nodes are involved in the support domain than that of the FDTD method for field-updating at each time step.

B. Two dimensional structure

We also considered an air-filled perfect electric conducting cavity with PEC boundary conditions. The cavity is a good structure for numerical validation since it embodies multiple incidences and reflections of electromagnetic waves that can really test effectiveness of a numerical method. The dimensions of the cavity under consideration are 1 m × 1 m with uniform discretization of cell size of 2 cm. The initial condition is given as

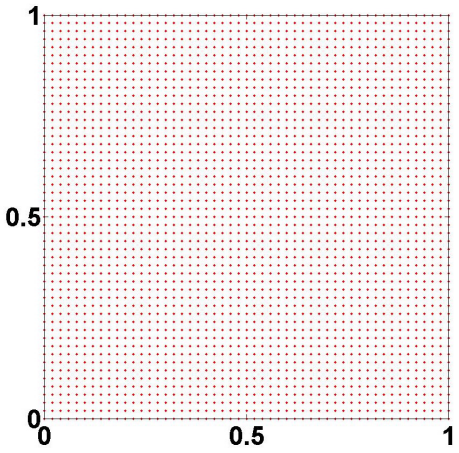

Figure 4.11 The node distribution of the proposed method for the two dimensional cavity.

$$E_z = \sin(m\pi x)\sin(n\pi y) \tag{4.40}$$

where m, n are the mode number in the x and y direction, respectively. The theoretical electric field inside the cavity can be expressed as:

$$E_z = \sin(m\pi x)\sin(n\pi y)\cos(\omega t) \tag{4.41}$$

where $\omega = c_0\pi\sqrt{m^2+n^2}$.

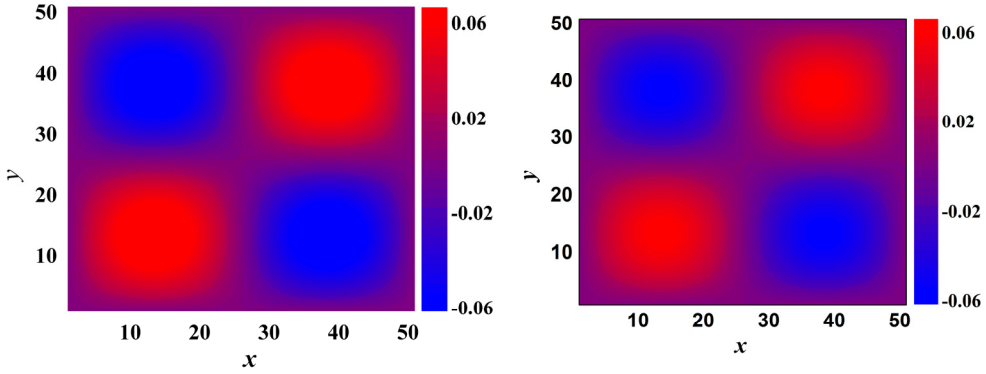

Figure 4.12 The analytical field (a) and numerical value obtained from the method (b) at 10 *ns*.

A small time step, $CFLN = 0.1$ again, is selected for the FDTD method and the proposed method to decrease the numerical error. The average number of the nodes considered in the local support domain is 9 and the shape parameter is selected to be 5 for Gaussian RBF. Figure 4.11 shows the node distribution of the proposed method. The distance between two nearest nodes is 0.02 *m*. The cell size is also 0.02 m for the FDTD method.

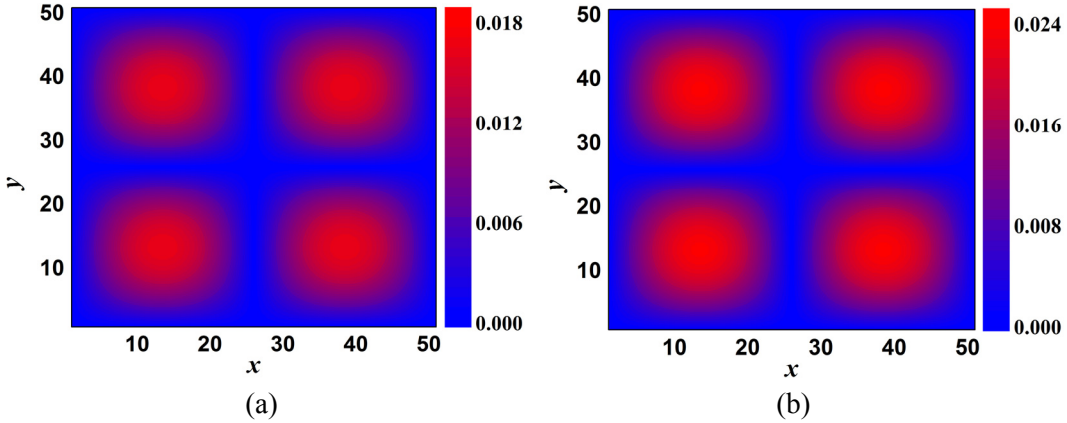

Figure 4.13 The absolute error for the proposed method (a) and the FDTD method (b) at 10 *ns*.

Figure 4.12 shows E_z field obtained with the proposed method at 10 ns with $m = 2$, and $n = 2$ for TM_{22}. Figure 4.13 presents the absolute error of the results obtained with the two

methods at 10 *ns*. The error distribution pattern of the proposed method is the same as that of the FDTD method. However, the magnitude is smaller than that of the FDTD method. It means that the proposed method can obtain more accurate results than the FDTD method. Again, this is because the proposed meshless method is essentially a higher-order method.

Figure 4.14 illustrates the relative L_2 error verse m with specific n. It can be found that the error of the proposed method is smaller than that of the FDTD method for all the m modes with $n = 1$ and $n = 3$. Another interesting observation is that as m increases, the L_2 errors of the two methods level off to the same value. This is because the spatial sampling density of the numerical methods is not sufficient to capture highly-varied field distributions of the higher modes any more with large m and n. The resonant frequency obtained from the FDTD method and the meshless method is 445.2 MHz for TM_{22}. It implies that both the methods can get the same accurate resonant frequency.

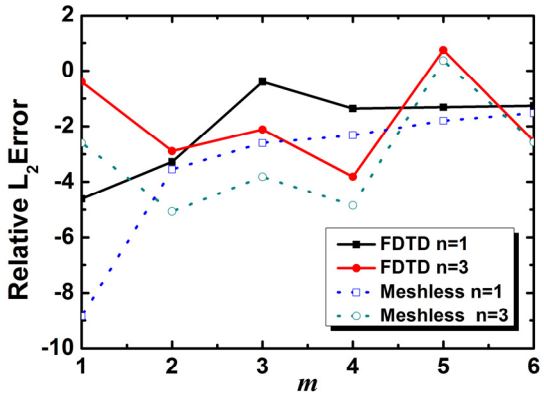

Figure 4.14 The L_2 error of the proposed method and the FDTD method verse m with $n = 1$ and $n = 3$ at 10 *ns*.

C. Three dimensional structure

In a three dimensional case, an air-filled PEC cavity with PEC boundary condition and dimensions of 1 $m \times 1$ $m \times 1$ m is considered. The cavity is discretized with the uniform cell size of 10 *cm*. The same initial condition for the two dimensional case is chosen. Again, we choose a quite small time step ($CFLN = 0.1$) for the FDTD method and the proposed method in order to decrease the numerical error. Average number of the nodes in the local support domain is 16 and the shape parameter is 0.5.

Figure 4.15 presents E_z field obtained from the proposed solver at 10.5 *ns* with $m = 2$,

and $n = 2$. The field distribution is TM_{22} mode. As shown in Figure 4.16, the error pattern of the proposed method is exactly the same as that of the FDTD method. However, its magnitude is smaller than that of the FDTD method, which means that the proposed method can obtain more accurate results than the FDTD method. This is because the proposed meshless method is a high order method.

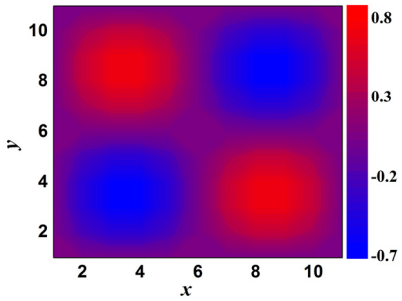

Figure 4.15 The field value obtained from the proposed method at 10.5 *ns*.

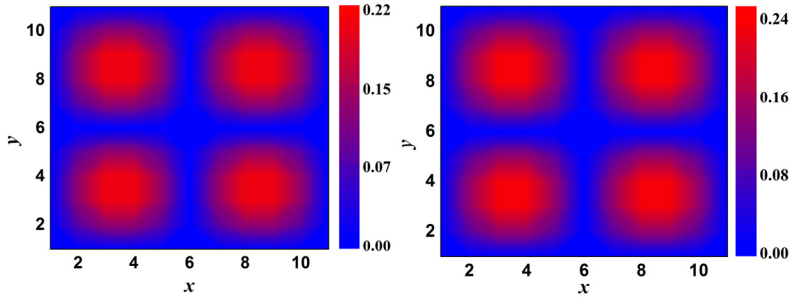

(a) (b)

Figure 4.16 The absolute error for the proposed method (a) and the FDTD method (b) at 10.5 *ns*.

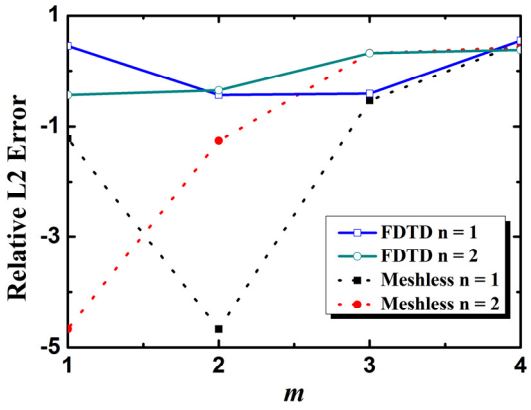

Figure 4.17 The L_2 error of the proposed solver and the FDTD method verse m with $n = 1$ and $n = 2$ at 10.5 *ns*.

Figure 4.17 presents the relative L_2 error verse m. It can be found that the error of the proposed method is smaller than that of the FDTD method for all the m modes with $n = 1$

and $n = 2$. The relative L_2 errors of the two methods increase as m goes up. To obtain more accurate results for higher-order modes, denser nodes are required for the two methods. Another interesting observation is that for the FDTD method, the error of TM_{11} is larger than that of TM_{12} at 10. 5 *ns*; so is for the proposed method.

Figure 4.18 shows the charge density in dB, at $z = 0.4$ m, obtained from the proposed method with $m = 2$ and $n = 2$ at 10.5 *ns*. The charge density level is about -15 *dB* which is at the level of numerical noise. In other words, we can safely consider the proposed method produces no artificial charge accumulation like other divergence-free methods, such as the FDTD method.

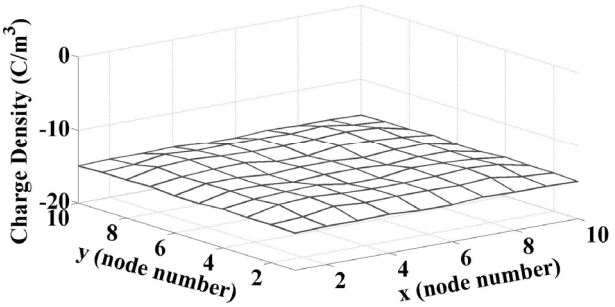

Figure 4.18 The charge density at $z = 0.4$ m plane of the proposed solver with $n = 2$ and $m = 2$ at 10.5 *ns*.

4.3 Conclusion

A new vector RBF based meshless method, which is theoretically proven to be divergence free, is proposed for the transient electromagnetic analysis. Its divergence properties are investigated and compared with those of the original scalar RBF meshless method. It is found that the scalar RBFs cannot always retain divergence free in source free regions while the proposed vector RBF based meshless method does. Numerical examples are presented to verify the accuracy and divergence properties of the proposed method for the Maxwell's equations and wave equation.

Chapter 5 Stable Meshless Method Based on the RBF-QR Method

This chapter is mainly based on our published paper [47], which is Shunchuan Yang, Zhizhang (David) Chen, Yiqiang Yu, and Sergey Ponomarenko, "A Robust Meshless Method with QR-Decomposed Radial Basis Functions," published in IEEE International Microwave Symposium, 2015, pp. 1-3.

5.1 Abstract

Ill-condition of the interpolation matrix has presented a hurdle in applying a node-based meshless method to practical modeling and simulation of electromagnetic structures. In this chapter, a robust meshless method is proposed that does not have the problem. It employs the QR method to decompose the Gaussian RBF; as a result, the matrix ill-condition that persists with a meshless method having a small shape parameter is theoretically removed. In other words, unlike the conventional meshless method, the proposed method is insensitive to the shape parameters and can work well even when the RBF becomes extremely flat.

5.2 Introduction

Recently, meshless methods have attracted attention for solving electromagnetic problems due to their intrinsic properties such as conformal and multi-scale modelling capability [28, 61, 62]. For most of these meshless methods, only spatial node information is needed to formulate electromagnetic problems. No connection information among nodes is required. Consequently, no re-arrangements of grid lines are required when a structure is modified partially.

In general, meshless methods are based on the point interpolation process. Inversion of the associated interpolation matrix is required. However, this inversion becomes problematic when the shape parameter becomes very small and the matrix becomes seriously ill-conditioned; it leads to failure of practical simulations. On the other hand, the smaller the shape parameter is, the more accurate results can be obtained [37, 38]. Therefore, tradeoff between the accuracy and the matrix condition needs to be made for the meshless methods. Special care needs to be taken to choose reasonable values of the

shape parameters. Several strategies such as those described in [39] have been proposed to search for the optimal shape parameters. Unfortunately, these so-called optimal values are often problem-dependent and we have to perform a search for every different problem structure or partial change of a structure. Even worse, such an optimal value may not exist in a problem.

To resolve the issue of the ill-conditioning matrix associated with expansion basis functions, a method to modify radial basis function is proposed in computational mathematical community for non-electrical applications [37, 38]; in it, Gaussian RBF, which is more preferred when partial differential is involved [65], is expanded with the QR decomposition method and the shape parameter can be theoretically factored out from the original basis functions. In this chapter, we propose to extend the same technique to the meshless method for solving electromagnetic problems; as a result, a robust meshless method without the ill-condition issue is developed for solving Maxwell's equations. To the best of our knowledge, there have been no reports of such a robust method before in computational electromagnetics.

5.3 The Proposed Stable Meshless Method

Consider Maxwell's equations in a linear, lossless, isotropic and non-dispersive medium without sources, which are expressed as

$$\frac{\partial \mathbf{E}}{\partial t} = \frac{1}{\varepsilon} \nabla \times \mathbf{H} \tag{5.1a}$$

$$\frac{\partial \mathbf{H}}{\partial t} = -\frac{1}{\mu} \nabla \times \mathbf{E} \tag{5.1b}$$

where $\mathbf{E} = \left[E_x \; E_y \; E_z \right]^T$,. $\mathbf{H} = \left[H_x \; H_y \; H_z \right]^T$, ε and μ are permittivity and permeability of the medium, respectively.

The above vector equations can be expanded into six scalar component formulations. Spatially, the field quantities to be solved are expanded in terms of the shape functions that are derived from the RBF. Temporally, the derivative in time is approximated with its central finite-difference correspondence. The result is the following march-in-time

recursive equations of a meshless method [28]:

$$H_{x,i}^{n+1/2} = H_{x,i}^{n-1/2} - \frac{\Delta t}{\mu} \times \sum_j E_{z,j}^n \partial y \Phi_j \tag{5.2b}$$

$$E_{z,i}^{n+1} = E_{z,i}^n - \frac{\Delta t}{\varepsilon} \times \sum_j H_{x,j}^{n+1/2} \partial y \Phi_j \tag{5.2d}$$

However, when implemented with the traditional RBFs, (5.2) can become ill-conditioned and unstable when the shape parameter of RBFs is small. In the following paragraphs, we will find another set of basis functions that circumvent this problem and make the method stable when the shape parameter is small and even approaches to zero.

Consider Gaussian RBF $\varphi(x, x_i) = e^{-p(x-x_i)^2}$. We now expand it first with another two basis functions, say, κ and υ. We can have:

$$\varphi(x, x_i) = e^{-p(x-x_i)^2} = \sum_{n=1}^{\infty} \lambda_n \kappa_n(x) \upsilon_n(x_i) \tag{5.3}$$

where λ_n is the expansion coefficient which is associated with the shape parameter *p*. When $\kappa = \upsilon$, λ_n is the eigenvalue and κ is the eigenfunction of the associated compact integral operator [38]. More specifically, λ_n and κ_n can be expressed as

$$\lambda_n = \sqrt{\frac{\alpha^2}{\alpha^2 + \delta^2 + p^2}} \left(\frac{p^2}{\alpha^2 + \delta^2 + p^2} \right)^{n-1}, \quad n = 1, 2, \ldots \tag{5.4a}$$

$$\kappa_n = \gamma_n e^{-\delta^2 x^2} H_{n-1}(\alpha \beta x), \qquad n = 1, 2, \ldots \tag{5.4b}$$

where $\beta = \left(1 + \left(\frac{2p}{\alpha} \right)^2 \right)^{\frac{1}{4}}$, $\delta^2 = \frac{\alpha^2}{2}(\beta^2 - 1)$, $\gamma_n = \sqrt{\frac{\beta}{2^{n-1}\Gamma(n)}}$ and H_{n-1} is the classical Hermite polynomials of degree n - 1.

Suppose that we only retain the first *M* order of both ϕ and υ. Then (5.3) can be rewritten in the compact matrix form as

$$\mathbf{A} = \boldsymbol{\kappa}\boldsymbol{\Lambda}\boldsymbol{\upsilon} \tag{5.5}$$

where

$$\boldsymbol{\kappa} = \begin{bmatrix} \kappa_1(x_1) & \cdots & \kappa_M(x_1) \\ \vdots & & \vdots \\ \kappa_1(x_n) & \cdots & \kappa_M(x_n) \end{bmatrix}, \quad \boldsymbol{\Lambda} = \begin{bmatrix} \lambda_1 & & \\ & \ddots & \\ & & \lambda_M \end{bmatrix} \text{ and } \quad \boldsymbol{\upsilon} = \begin{bmatrix} \upsilon_1(x_1) & \cdots & \upsilon_1(x_n) \\ \vdots & & \vdots \\ \upsilon_M(x_1) & \cdots & \upsilon_M(x_n) \end{bmatrix}.$$

Here we can choose $M > N$, where N is the number of the nodes in a support domain.

Now the QR decomposition method is applied to find the optimal basis function υ for the expansion. After applying the QR method to matrix $\boldsymbol{\upsilon}^T$, we obtain the following equation

$$\begin{aligned} \boldsymbol{\upsilon}^T &= \begin{bmatrix} \upsilon_1(x_1) & \cdots & \upsilon_N(x_1) & | & \upsilon_{N+1}(x_1) & \cdots & \upsilon_M(x_1) \\ \vdots & & \vdots & | & \vdots & & \vdots \\ \upsilon_1(x_N) & \cdots & \upsilon_N(x_N) & | & \upsilon_{N+1}(x_N) & \cdots & \upsilon_M(x_N) \end{bmatrix} \\ &= \mathbf{QR} = \mathbf{Q}\begin{pmatrix} \mathbf{R}_1 & | & \mathbf{R}_2 \end{pmatrix}, \end{aligned} \tag{5.6}$$

where the $\mathbf{R_1}$ block is a square matrix of size N and $\mathbf{R}_2$ is $N\times(M\text{-}N)$.

Substituting (5.6) into (5.5), we can find that

$$\mathbf{A} = \boldsymbol{\Phi}\boldsymbol{\Lambda}\mathbf{R}^T\mathbf{Q}^T \tag{5.7}$$

By decomposing the same block structure of Λ which was imposed on $\mathbf{R}$, we obtain the full system in blocks as

$$\mathbf{A} = \boldsymbol{\kappa}\begin{bmatrix} \mathbf{I} \\ \Lambda_2\mathbf{R}_2^T\mathbf{R}_1^{-T}\Lambda_1^{-1} \end{bmatrix}\Lambda_1\mathbf{R}_1^T\mathbf{Q}^T. \tag{5.8}$$

In (5.8), the two terms, $\Lambda_2\mathbf{R}_2^T\mathbf{R}_1^{-T}\Lambda_1^{-1}$ and $\Lambda_1\mathbf{R}_1^T\mathbf{Q}^T$, are associated to the expansion coefficients. By further mathematical manipulations, the new basis function is found to be:

$$\begin{aligned}\boldsymbol{\psi} &= \mathbf{A}\mathbf{X}^{-1} \\ &= \left[\boldsymbol{\kappa}\begin{pmatrix}\mathbf{I} \\ \Lambda_2\mathbf{R}_2^T\mathbf{R}_1^{-T}\Lambda_1^{-1}\end{pmatrix}\Lambda_1\mathbf{R}_1^T\mathbf{Q}^T\right]\left[\Lambda_1\mathbf{R}_1^T\mathbf{Q}^T\right]^{-1} \\ &= \boldsymbol{\kappa}\begin{pmatrix}\mathbf{I} \\ \Lambda_2\mathbf{R}_2^T\mathbf{R}_1^{-T}\Lambda_1^{-1}\end{pmatrix}\end{aligned} \tag{5.9}$$

where $\mathbf{X} = \Lambda_1\mathbf{R}_1^T\mathbf{Q}^T$.

Notice now that expansion coefficient $\lambda_n \to 0$ as $n \to \infty$ which means that the expansion coefficient in Λ_2 is smaller than those in Λ_1. Therefore, the entries of $\mathbf{R}_2^T\mathbf{R}_1^{-T}$ will not be magnified when the term $\Lambda_2\mathbf{R}_2^T\mathbf{R}_1^{-T}\Lambda_1^{-1}$ is formed and it can be regarded as the correction terms on the basis of $\boldsymbol{\Phi}$.

5.4 Numerical Results and Discussion

One dimensional resonator with the perfect electrical conductor (PEC) walls at both ends was used for our numerical verification of the proposed method. The length of the one dimensional cavity is 1 meter. It is discretized with 50 nodes and the average number of nodes in a local support domain is 8. The equispaced node distribution is considered. The current source is located at the center and is specified as

$$J_z = \cos(2\pi ft)\exp\left(-\left(\frac{t_c - t}{t_w}\right)^2\right) \tag{5.10}$$

where $f = 0.5$ *GHz*, $t_w = 2.0$ *ns* and $t_c = 6.0$ *ns*. For comparison purpose, the results obtained from the conventional meshless method based on Gaussian function are also presented.

Figure 5.1 shows the recorded electrical field verse time with different shape parameters. For the conventional method, when shape parameter $p = 10^{-3}$, the solution becomes divergent. However, for the proposed method, even when $p = 10^{-15}$, the solution is still stable and agree well with each other.

Figure 5.2 shows the condition number of interpolation matrix of the proposed method and the conventional meshless method at location $z = 0.81$. It is easy to see that the condition number of the conventional method increases dramatically as the shape

parameter decreases. When $p < 0.001$, the condition number exceeds 10^{17} and direct inversion of the interpolation matrix cannot give stable and accurate results; instability and simulation failure occurs. In other words, the shape parameter cannot be too small with the conventional meshless method. However, with the proposed method, the condition number is almost independent of the shape parameter. Although the condition number of the proposed method is larger than that of the conventional method when $p > 0.008$, it remains almost constant and presents good results.

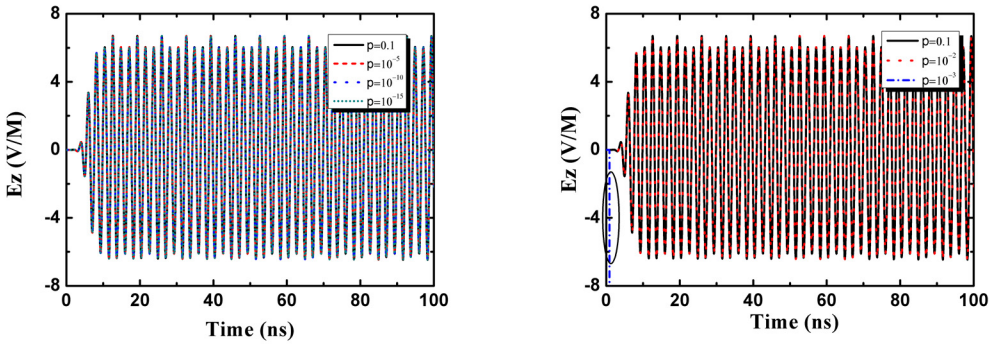

(a) (b)

Figure 5.1 The field solution obtained with the proposed method (a) and the conventional meshless method (b) with different shape parameters.

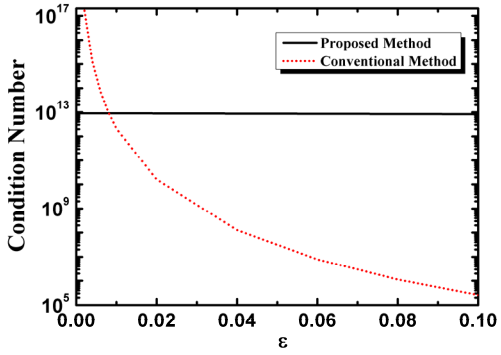

Figure 5.2 Condition number of the proposed method and the conventional method.

5.5 Conclusion

The ill-condition of the interpolation matrix has presented a challenge for a meshless method to be used for practical modeling and simulation of electromagnetic structures. In this chapter, a robust meshless method is proposed to address the issue. By applying the QR decomposition to expand the radial basis functions, dependence of the shape

parameters that cause the ill-condition of the interpolation matrix has been removed. Numerical example verifies the effectiveness of the proposed method. The preliminary results show that the root source of the ill-condition has been removed.

Chapter 6 On the Numerical Dispersion of the Radial Point Interpolation Meshless Method

This chapter is based on our published paper [45], which is Shunchuan Yang, Zhizhang (David) Chen, Yiqiang Yu, and Sergey Ponomarenko, "On the Numerical Dispersion of the Radial Point Interpolation Meshless Method," published in IEEE Microwave and Wireless Components Letters, vol. 24, pp. 653 - 655, 2014..

6.1 Abstract

The numerical dispersion of the time-domain RPIM method is investigated in this chapter. It is found that numerical dispersion relationship of the RPIM method shares the same form as that of a second-order center FDTD method but with the additional factors introduced by the RBFs, when the two methods deploy the same nodal distribution for problem-domain discretization and the local support domain of the RPIM method encloses only four adjacent nodes. Such an observation indicates that the RPIM method is a more general method and can be reduced to the conventional FDTD method under certain conditions. In addition, comparisons between the meshless method and the FDTD method are shown under different conditions.

6.2 Introduction

Unlike the conventional grid-based methods such as the FDTD method [6], the FEM [74] and the MOM [75], meshless methods interpolate fields to be solved with the field values at predefined nodes that scatter around in a support domain. A set of algebraic equations based on positions of the scattering nodes in a solution domain is then established and solved by linear solvers. That means that unlike grid-based methods, connection information between nodes is not required, which leads to easy implementation and high flexibility in modeling complex structures. As a result, the number of the published reports on the meshless methods for solving electromagnetic problems has increased dramatically. In particular, the smoothed particle electromagnetic method [29] and the RPIM method [27] have been proposed. Other forms of the meshless methods including the leapfrog and alternatively-direction-implicit RPIM methods in the time-domain are summarized in [32]. However, to the best of authors' knowledge, no numerical dispersion of the meshless

methods has been reported so far. In addition, no direct relationship between the FDTD method and RPIM method have been shown although it is mentioned in [28] that the RPIM method may reduce to the FDTD method under certain condition (but no theoretical proof was given there).

In this chapter, we will fill in the void by investigating the numerical dispersion of the RPIM method and the relationship between the RPIM method and the FDTD method in terms of the numerical dispersion relationship. In addition, we will discuss the relationship between the shape parameter and the numerical dispersion of RPIM method. Due to limit of space, we restrict our studies to the leapfrog time-domain meshless method.

6.3 Dispersion Analysis

To obtain analytical expressions of the numerical dispersion of the RPIM method, the spectral Fourier transform is applied, similar to that for the FDTD method presented in [16]. For arbitrary numbers and positioning of nodes, numerical dispersion formulations of the RPIM method may not be practically meaningful due to their varieties used by different users, in addition to the difficulty in finding the associated formulations. Therefore, in this chapter, we consider the case where the nodes are positioned in the same grid placement as that in the Yee's grid for the conventional FDTD method. In other words, in a support domain of a node, we consider one field component at one node, four H-nodes associated with one E-node and four E-nodes associated with one H-node, in a three dimensional setting. For the time domain discretization, we consider a second-order central finite-difference scheme for RPIM method. That means we can obtain the so-called leap-frog scheme for the time-marching equations [31].

By applying the spatial Fourier transformation to the meshless time domain formulations [31], we can obtain the time-marching equations in the spectral domain. For example, take E_z component for the illustration purpose. The time-marching equation for E_z in the spectral domain is then

$$E_{\mathrm{z},i}^{n+1/2} = E_{\mathrm{z},i}^{n+1/2} + \frac{\Delta t}{\varepsilon}\left(\sum H_{\mathrm{y},j}^{n+1/2}\partial_x \Phi_j - \sum H_{\mathrm{x},j}^{n+1/2}\partial_y \Phi_j\right) \tag{6.1}$$

where Φ_j is the shape function corresponding to node *j* in the local support domain. We can express the shape function in the vector form for all nodes as $\mathbf{\Phi} = [\Phi_1 \quad \Phi_2 \quad \cdots \quad \Phi_N]$, where $\mathbf{\Phi} = \mathbf{B}\mathbf{G}^{-1}$ with the RBF vector **B** and interpolation matrix **G**. **G** can be expressed as

$$\mathbf{G} = \begin{bmatrix} 1 & e^{-p(r/r_{\max})^2} \\ e^{-p(r/r_{\max})^2} & 1 \end{bmatrix} \tag{6.2}$$

r_{max} is the maximum radius of the local support domain, which is taken in such a way that only four nodes are located in the support domain [31]; r is the distance between the two nodes in the local support domain. Thus, the first order partial derivative of the RBF vector **B** can be stated as

$$\partial_\xi \mathbf{B} = e^{-p\left(\frac{r}{2r_{\max}}\right)^2} \frac{p\Delta\xi}{r_{\max}^2}[-1 \quad 1] \tag{6.3}$$

where $\xi = x, y \text{ and } z$ and p is named as the shape parameter which can be found in [31]. Thus, the partial derivative of the shape function with respect to ξ can be obtained as:

$$\partial_\xi \mathbf{\Phi} = \partial_\xi \mathbf{B}\mathbf{G}^{-1} = \frac{\Delta\xi p}{r_{\max}^2} \frac{e^{-p(r/2r_{\max})^2}}{-1+e^{-p(r/r_{\max})^2}}[1 \quad -1]. \tag{6.4}$$

By substituting (6.4) into (6.1) the following equation is obtained in the spectral domain:

$$E_z^{n+1/2} = E_z^{n-1/2} + j\frac{2\Delta t}{\Delta y\varepsilon}\sin\left(\frac{k_y\Delta y}{2}\right)\Delta y M_y H_x^n - j\frac{2\Delta t}{\Delta x\varepsilon}\sin\left(\frac{k_x\Delta x}{2}\right)\Delta y M_x H_y^n. \tag{6.5}$$

Here $M_\xi = \frac{\Delta\xi p}{r_{\max}^2}\frac{e^{-p(r/2r_{\max})^2}}{-1+e^{-p(r/r_{\max})^2}}$ and k_ξ is the spatial frequency in the ξ direction. Other field components can also be obtained in the similar manner.

With the similar process as described in [13, 76], the final dispersion relationship can be obtained as

$$\left(\sin\left(\frac{w\Delta t}{2}\right)\right)^2 = \frac{\Delta t^2}{\mu\varepsilon}\left[\left(\frac{M_{xx}\sin\left(\frac{k_x\Delta x}{2}\right)}{\Delta x}\right)^2 + \left(\frac{M_{yy}\sin\left(\frac{k_y\Delta y}{2}\right)}{\Delta y}\right)^2 + \left(\frac{M_{zz}\sin\left(\frac{k_z\Delta z}{2}\right)}{\Delta z}\right)^2\right] \tag{6.6}$$

with $M_{\xi\xi} = \Delta\xi M_{\xi}$. (6.6) looks like the numerical dispersion relation of the conventional FDTD method with the addition of factors $M_{\xi\xi}$ on the right hand side.

Noticeably, we can see that when $\Delta\xi$ and p approaches zeros, respectively,

$$\lim_{\Delta\xi\to 0} M_{\xi\xi} = \lim_{\Delta\xi\to 0} \frac{\Delta\xi^2 p}{r_{\max}^2} \frac{e^{-p(r/2r_{\max})^2}}{-1+e^{-p(r/r_{\max})^2}} = -1 \tag{6.7}$$

and

$$\lim_{p\to 0} M_{\xi\xi} = \lim_{p\to 0} \frac{\Delta\xi^2 p}{r_{\max}^2} \frac{e^{-p(r/2r_{\max})^2}}{-1+e^{-p(r/r_{\max})^2}} = -1. \tag{6.8}$$

The above results means that the final numerical dispersion (6.6) becomes the analytic dispersion, $\omega^2\mu\varepsilon = k_x^2 + k_y^2 + k_z^2$, when shape parameter p, time step Δt and spatial step $\Delta\xi$ approach to zero. When shape parameter p goes to zero, (6.6) becomes identical to the dispersion of FDTD [6]. As a result, the FDTD method can be considered as a special case of RPIM method. This can also be easily seen from (6.1): when p goes to zero, (6.4) becomes $-1/\Delta\xi$ and by substituting it into (6.1), we can obtain the updating formulation for the FDTD.

6.4 Numerical Results and Discussion

The shape parameter p plays an important role in RPIM method. In [33], the relationship between stability of the time-iteration of RPIM method and the shape parameter has been shown. In this section, we discuss how the shape parameter affects the numerical dispersion.

To measure the numerical dispersion error, the numerical phase error (*NPE*) per unit length is defined and used [16]:

$$NPE = \left| \frac{k_{num} - k_0}{k_0} \right| = \left| \frac{c - c_{num}}{c_{num}} \right| \tag{6.9}$$

where k_0 is the theoretical wave number, k_{num} is numerical wave number, $c = \omega/k_o$ is the speed of light in the continuous medium and $c_{num} = \omega/k_{num}$ is the speed of numerical waves with the RPIM method. ω is the angular frequency.

In the calculations,

$$\begin{aligned} k_x &= k_{num} \sin\theta \cos\varphi \\ k_y &= k_{num} \sin\theta \sin\varphi \\ k_z &= k_{num} \cos\theta. \end{aligned} \tag{6.10}$$

Here θ and φ are the propagation angles in vertical and the horizontal planes, respectively.

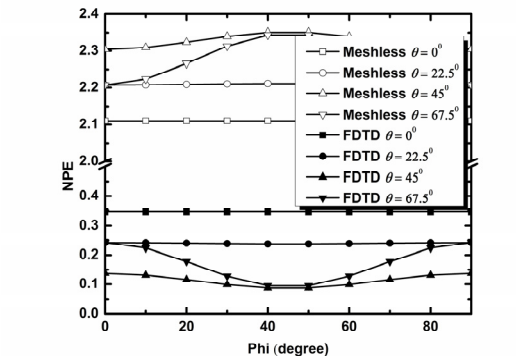

Figure 6.1 *NPE* of the meshless method with $p = 0.1$ and the FDTD method; $PPW = 20$ and $CFLN = 1$.

Figure 6.1, 6.2, 6.3 and 6.4 show *NPE* of the meshless method with different values of shape parameter p and that of the FDTD method. The spatial step is 1/20 of the wavelength, i.e., the spatial sampling is 20 points per wavelength (*PPW*). r_{max} equals to the spatial step. The time step was selected to be the same for both methods in order to make a fair comparison: it is the maximum time limit of the FDTD method, or the *CFL* number is one ($CFLN = 1$).

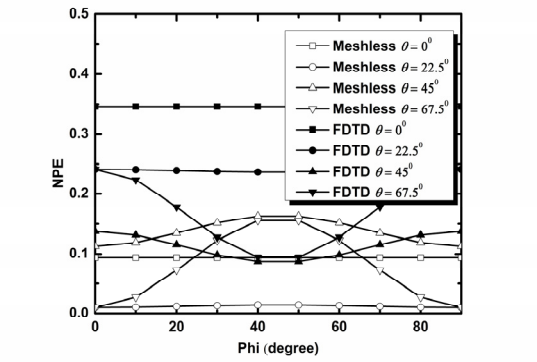

Figure 6.2 *NPE* of the meshless method with $p = 0.01$ and the FDTD method; $PPW = 20$ and $CFLN = 1$.

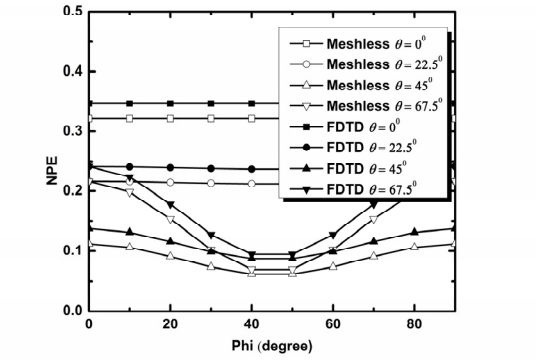

Figure 6.3 *NPE* of the meshless method with $p = 0.001$ and the FDTD method with $PPW = 20$ and $CFLN = 1$.

It is easily seen from the figures that when $p = 0.1$, *NPE* of the meshless method reaches its maximum at $\theta = 45^{o}$ and its minimum at $\theta = 0^{o}$. However, for the FDTD method, the numerical dispersion arrives at its minimum when $\theta = 45^{o}$ and maximum when $\theta = 0^{o}$. Therefore, numerical dispersions of the two methods show totally different properties but this difference become smaller when shape controlling parameter p becomes smaller.

When $p = 0.1$, the maximum numerical dispersion errors of the meshless method is about as 7 times of that of the FDTD method. However, when $p = 0.01$, the situation reverses: the maximum numerical dispersion errors are smaller than that of the FDTD method. When $p = 0.001$, the numerical dispersion errors of the two methods becomes similar. When $p = 0.0001$, they become indistinguishable. This confirms our previous analysis that when p approaches to zero, the numerical dispersion of the meshless method and the FDTD method becomes exactly the same. This indicates that the shape parameter p plays an important role on the numerical dispersion and the convergence of the meshless

method to the FDTD method with better accuracy. Therefore, a reasonable value should be selected in the practical simulations. It should be also noted that although better convergence is achieved with small sharp parameter, it also comes with smaller stable time iterations [33]. The balance should be taken between the stability condition and the accuracy. In our study case, we chose $p = 0.018$ where the maximum numerical dispersion errors of RPM method equals to that of FDTD method. However, the optimized shape parameters are on a case-by-case basis; in [39], the authors proposed an automatic approach to search for the reasonable value with respect to a specific case.

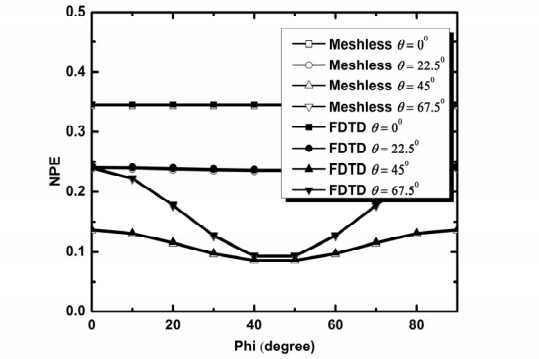

Figure 6.4 *NPE* of the meshless method with $p = 0.0001$ and the FDTD method with $PPW = 20$

6.5 Conclusion

In this chapter, numerical dispersion of the RPIM method is shown and its comparisons with that of the FDTD method are presented. Analytical derivations show that the numerical dispersion of the RPIM method is exactly the same as that of the FDTD method when the shape parameter p approaches zero. It indicates that the method is a general method which can include the conventional FDTD method as its special case. Different numerical dispersion results based on various shape parameters are illustrated. The analysis shows that shape parameter should be selected carefully in the practical simulations to obtain small numerical dispersion errors and good stability.

Chapter 7 Conclusion Remarks and Recommendations

7.1 Conclusion Remarks

This thesis have studied several properties of the newly developed divergence preserved ADI-FDTD method and the meshless method. Especially, emphasis is placed on the divergence issue and efficiency of both methods.

Although the traditional ADI-FDTD methods are unconditionally stable, they are not divergence preserved, as stated in [22, 23]. That means that artificial charges would be introduced into the simulations and make solutions inaccurate when charges are considered which may lead to failure of simulations. In this thesis, attention is paid to studying the newly developed divergence preserved ADI-FDTD method, which can preserve the divergence property of the electrical and magnetic field. Proof of stability and numerical dispersion are systematically presented using von Neumann method and efficiency are carefully studied in terms of floating-point count. In addition, based on the fundamental formulations, a new efficiency-improved version is proposed. Its divergence property and efficiency are then studied.

For the meshless method, the traditional implementation based on the local Gaussian function requires two coupled fields (E- and H-field). Based on the mathematical equivalence of the Maxwell's equations and wave equations, efficiency can be improved through solving wave equations due to decoupling nature of E- and H-field. Besides efficiency issue, the divergence problem also exists in the meshless method. To overcome this problem, a new vector-based RBF is proposed for the meshless method, which is theoretically divergence free. In addition, the notorious ill-condition problem in the meshless method is addressed through the QR decomposition method. At last, the relationship between the FDTD method and the meshless method is theoretically investigated in terms of their numerical dispersion relationship.

A summary of each study and its main findings is given in following.

(1) Studying the unconditionally stable divergence preserved ADI-FDTD method and its efficiency improved version.

The detailed implementations of the divergence preserved ADI-FDTD method are investigated in this thesis. Based on von Neumann analysis, the magnitudes of all the

eigenvalues of the magnification matrix are found to equal to one, which means that this method is unconditionally stable. Further investigation shows that the numerical dispersion relationship of the divergence preserved ADI-FDTD method is the same as that of the ADI-FDTD method, the LOD-FDTD method and the leapfrog ADI-FDTD method. However, the last three methods are not divergence free and artificial charges will be introduced into the simulations.

To improve the efficiency of the divergence preserved ADI-FDTD method, an efficient updating method is proposed based on its fundamental formulations. With the proposed method, the right hand side of time-marching equations are matrix free. Almost 41.7% less count of floating-point operations than the original divergence-preserved ADI-FDTD method is obtained without scarifying accuracy. At the same time, the proposed method preserve the divergence property of the electrical and magnetic fields like the original divergence preserved ADI-FDTD method.

(2) Developing the meshless method based on the local Gaussian RBF for the wave equation

It is well-known that the Maxwell's equations and the wave equations are mathematically equivalent. Therefore, numerical methods for the wave equations can get the same numerical results as those for the Maxwell's equations. Since usually only one set of field (either E or H field) is involved with the wave equation, we can expect higher computational efficiency of numerical methods for the wave equations than those for the Maxwell's equations. A meshless method based on local RBF is applied to solving the wave equations. Two numerical examples computing the resonant frequencies of an H-shaped cavity and ring resonator verify the efficiency improvement and the conformal and multi-scale capability of the proposed method. The results show that the proposed method can indeed largely improve the efficiency without loss any accuracy.

(3) Exploring the divergence issue of the meshless method

The traditional meshless methods based on the local Gaussian RBF for Maxwell's equations are not always divergence free since the divergence condition is not explicitly applied and the Gaussian RBF is not divergence free. In this thesis, a vector-based RBF is proposed to overcome this problem. Systematical investigation finds that this vector-based RBF is theoretically divergence free. Then, it is applied to solve Maxwell's equations and

the wave equation. As expected, the resultant meshless methods are divergence free. On the contrary, the conventional meshless methods based on the scalar RBF are found not divergence free because the divergence of the scalar RBF is location dependent. As a result, for random node distribution, the divergence of the scalar RBF cannot be guaranteed to be zero. However, for the vector RBF, it is always true.

(4) Investigating the meshless method based on QR method

Another issue for the meshless method is the ill-condition of the interpolation matrix. Since inversion of the interpolation matrix is inevitable, the ill-condition problem may lead to failure of the simulations. In this thesis, a new meshless method based on the QR decomposition is proposed to address the issue. By applying the QR decomposition to expand the Gaussian RBF, the shape parameter which causes the ill-condition of the interpolation matrix is separated from the Gaussian RBF and a new stable RBF is obtained for the meshless method. Numerical example shows that the condition number of the interpolation matrix is independent of the shape parameter and the new RBF always works even when the shape parameter is extremely small.

(5) Studying the relationship between the meshless method and the FDTD method.

Relationship between the meshless method and the FDTD method is investigated in terms of numerical dispersion. Based on the same node distribution and field component distribution, a numerical dispersion formulation is derived for the meshless method. It is found that the numerical dispersion of the meshless method becomes exactly the same as that of the FDTD method when the shape parameter goes to zero. That means that the meshless method is a general method which can include the conventional FDTD method as its special case.

7.2 Recommendations for Future Work

Recommendations for future work mainly focus on applying the meshless method based on QR method and divergence-free meshless method to solving electromagnetic problems in the two and three dimensional cases and development of the PML techniques to solve the practical engineering structures.

The first recommendation is that investigation of the meshless method based on QR method for the two- and three-dimensional cases in the time domain and frequency domain.

For these cases, the RBF can be easily obtained using the tensor product form of the Gaussian kernel. For the d (d = 2, 3) dimensional Gausses function, we have

$$\varphi(\mathbf{x},\mathbf{x_i}) = e^{-\left(p^2(x-x_1)^2+\cdots+p^2(x-x_d)^2\right)} = \sum \lambda_n \phi_n(x)\phi_n(x_i) \tag{7.1}$$

where $\lambda_{\mathbf{n}} = \prod_{j=1}^{d} \lambda_{n_j} = \prod_{j=1}^{d} \sqrt{\frac{\alpha_j^{\,2}}{\alpha_j^{\,2}+\delta_j^{\,2}+p_j^{\,2}}} \left(\frac{p_j^{\,2}}{\alpha_j^{\,2}+\delta_j^{\,2}+p_j^{\,2}}\right)^{n_j-1}$, $\varphi_{\mathbf{n}} = \prod_{j=1}^{d} \varphi_{n_j} = \prod_{j=1}^{d} \gamma_{n_j} e^{-\delta^2 x_j^{\,2}} H_{n_j-1}(\alpha_j \beta_j x_j)$

and $\mathbf{x} = (x_1, \cdots, x_d)^T$. Further work along the line need to be explored numerically.

The second recommendation is applying the QR method to the vector RBF. Although the vector RBF is divergence free, it still suffer from the ill-condition problem. When small shape parameter is selected or the count of the scattering node in the support domain is large, simulation may break down due to the extremely ill-conditioned interpolation matrix. Therefore, applying the QR method to vector RBF is an efficient way to avoid the ill-condition problem.

The third recommendation is development of the PML for the meshless method based on the vector RBF to solve the open structures. Since the PML is required to truncate the infinite computational domain to model the open radiation problems, to make the meshless method applicable for the practical engineering problems, future work will focus on applying the PML to the meshless method.

Bibliography

[1] G. B. Arfken, *Mathematical Methods for Physicists*: Academic Press, 2013.

[2] B. Ronald, *The Fourier Transform and Its Applications*: McGraw-Hill Science/Engineering/Math, 1965.

[3] R. F. Harrington, *Time-Harmonic Electromagnetic Fields*: Wiley-IEEE Press, 1961.

[4] T. R. Taha and M. I. Ablowitz, "Analytical and numerical aspects of certain nonlinear evolution equations. II. Numerical, nonlinear Schrödinger equation," *Journal of Computational Physics,* vol. 55, pp. 203-230, 1984.

[5] O. V. Sinkin, R. Holzlöhner, J. Zweck, and C. R. Menyuk, "Optimization of the split-step Fourier method in modeling optical-fiber communications systems," *Journal of Lightwave Technology,* vol. 21, pp. 61-68, 2003.

[6] A. Taflove and S. C. Hagness, *Computational Electrodynamics: The Finite-Difference Time-Domain Method*: Artech house Boston, 1995.

[7] T. Namiki, "3-D ADI-FDTD method-unconditionally stable time-domain algorithm for solving full vector Maxwell's equations," *IEEE Transactions on Microwave Theory and Techniques,* vol. 48, pp. 1743-1748, 2000.

[8] T. Namiki, "A new FDTD algorithm based on alternating-direction implicit method," *IEEE Transactions on Microwave Theory and Techniques,* vol. 47, pp. 2003-2007, 1999.

[9] S. Wang, F. L. Teixeira, and J. Chen, "An iterative ADI-FDTD with reduced splitting error," *IEEE Microwave and Wireless Components Letters,* vol. 15, pp. 92-94, 2005.

[10] F. Zhen, Z. Chen, and J. Zhang, "Toward the development of a three-dimensional unconditionally stable finite-difference time-domain method," *IEEE Transactions on Microwave Theory and Techniques,* vol. 48, pp. 1550-1558, 2000.

[11] E. L. Tan, "Unconditionally Stable LOD–FDTD Method for 3-D Maxwell's Equations," *IEEE Microwave and Wireless Components Letters,* vol. 17, pp. 85-87, 2007.

[12] I. Ahmed, E.-K. Chua, E.-P. Li, and Z. Chen, "Development of the three-dimensional unconditionally stable LOD-FDTD method," *IEEE Transactions on Antennas and Propagation,* vol. 56, pp. 3596-3600, 2008.

[13] Q.-F. Liu, Z. Chen, and W.-Y. Yin, "An arbitrary-order LOD-FDTD method and its stability and numerical dispersion," *IEEE Transactions on Antennas and Propagation,* vol. 57, pp. 2409-2417, 2009.

[14] Y.-D. Kong and Q.-X. Chu, "Development of the nearly PML for four-stages split-step unconditionally-stable FDTD method," in *Microwave Conference Proceedings (APMC)*, 2010, pp. 2168-2171.

[15] D. Y. Heh and E. L. Tan, "Further Reinterpretation of Multi-Stage Implicit FDTD Schemes," *IEEE Transactions on Antennas and Propagation,* vol. 62, pp. 4407 - 4411, 2014.

[16] S.-C. Yang, Z. Chen, Y. Yu, and W.-Y. Yin, "An unconditionally stable one-step arbitrary-order leapfrog ADI-FDTD method and its numerical properties," *IEEE Transactions on Antennas and Propagation,* vol. 60, pp. 1995-2003, 2012.

[17] G. Sun and C. Trueman, "Unconditionally stable Crank-Nicolson scheme for solving two-dimensional Maxwell's equations," *Electronics Letters,* vol. 39, pp. 595-597, 2003.

[18] K. Xu, Z. Fan, D.-Z. Ding, and R.-S. Chen, "GPU accelerated unconditionally stable Crank-Nicolson FDTD method for the analysis of three-dimensional microwave circuits," *Progress In Electromagnetics Research,* vol. 102, pp. 381-395, 2010.

[19] G. Sun and C. W. Trueman, "Efficient implementations of the Crank-Nicolson scheme for the finite-difference time-domain method," *IEEE Transactions on Microwave Theory and Techniques,* vol. 54, pp. 2275-2284, 2006.

[20] G. Sun and C. Trueman, "Unconditionally-stable FDTD method based on Crank-Nicolson scheme for solving three-dimensional Maxwell equations," *Electronics Letters,* vol. 40, pp. 589-590, 2004.

[21] S. G. Garcia, R. G. Rubio, A. R. Bretones, and R. G. Martín, "On the dispersion relation of ADI-FDTD," *IEEE Microwave and Wireless Components Letters,* vol. 16, pp. 354-356, 2006.

[22] T. Gan and E. Tan, "Analysis of the Divergence Properties for the Three-Dimensional Leapfrog ADI-FDTD Method," *IEEE Transactions on Antennas and Propagation,* vol. 60, pp. 5801 - 5808, 2012.

[23] T. H. Gan and E. L. Tan, "Divergence of electric field or the two-dimensional (2-D) leapfrog ADI-FDTD method," in *IEEE Antennas and Propagation Society International Symposium (APSURSI)*, 2012, pp. 1-2.

[24] B.-N. Jiang, J. Wu, and L. A. Povinelli, "The origin of spurious solutions in computational electromagnetics," *Journal of Computational Physics,* vol. 125, pp. 104-123, 1996.

[25] D. N. Smithe, J. R. Cary, and J. A. Carlsson, "Divergence preservation in the ADI algorithms for electromagnetics," *Journal of Computational Physics,* vol. 228, pp. 7289-7299, 2009.

[26] T. Huat Gan and E. Leong Tan, "Unconditionally stable fundamental LOD-FDTD method with second-order temporal accuracy and complying divergence," *IEEE Transactions on Antennas and Propagation,* vol. 61, pp. 2630-2638, 2013.

[27] S. Lai, B. Wang, and Y. Duan, "Meshless radial basis function method for transient electromagnetic computations," *IEEE Transactions on Magnetics,* vol. 44, pp. 2288-2295, 2008.

[28] T. Kaufmann, C. Fumeaux, and R. Vahldieck, "The meshless radial point interpolation method for time-domain electromagnetics," in *IEEE International Microwave Symposium*, 2008, pp. 61-64.

[29] G. Ala, E. Francomano, A. Tortorici, E. Toscano, and F. Viola, "Smoothed particle electromagnetics: A mesh-free solver for transients," *Journal of Computational and Applied Mathematics,* vol. 191, pp. 194-205, 2006.

[30] D. Soares, "Time-domain electromagnetic wave propagation analysis by edge-based smoothed point interpolation methods," *Journal of Computational Physics,* vol. 234, pp. 472-486, 2013.

[31] Y. Yu and Z. Chen, "A 3-D radial point interpolation method for meshless time-domain modeling," *IEEE Transactions on Microwave Theory and Techniques,* vol. 57, pp. 2015-2020, 2009.

[32] Y. Yu and Z. Chen, "Towards the development of an unconditionally stable time-domain meshless method," *IEEE Transactions on Microwave Theory and Techniques,* vol. 58, pp. 578-586, 2010.

[33] T. Kaufmann, C. Engstrom, C. Fumeaux, and R. Vahldieck, "Eigenvalue analysis and longtime stability of resonant structures for the meshless radial point interpolation method in time domain," *IEEE Transactions on Microwave Theory and Techniques,* vol. 58, pp. 3399-3408, 2010.

[34] S. Lowitzsch, "Matrix-valued radial basis functions: stability estimates and applications," *Advances in Computational Mathematics,* vol. 23, pp. 299-315, 2005.

[35] S. Lowitzsch, "A density theorem for matrix-valued radial basis functions," *Numerical Algorithms,* vol. 39, pp. 253-256, 2005.

[36] B. Fornberg and C. Piret, "A stable algorithm for flat radial basis functions on a sphere," *SIAM Journal on Scientific Computing,* vol. 30, pp. 60-80, 2007.

[37] B. Fornberg, E. Larsson, and N. Flyer, "Stable computations with Gaussian radial basis functions," *SIAM Journal on Scientific Computing,* vol. 33, pp. 869-892, 2011.

[38] G. E. Fasshauer and M. J. McCourt, "Stable evaluation of Gaussian radial basis function interpolants," *SIAM Journal on Scientific Computing,* vol. 34, pp. A737-A762, 2012.

[39] P. L. Machado, R. Oliveira, W. C. Souza, R. C. Araújo, M. E. Tostes, and C. Gonçalves, "An automatic methodology for obtaining optimum shape factors for the radial point interpolation method," *Journal of Microwaves, Optoelectronics and Electromagnetic Applications,* vol. 10, pp. 389-401, 2011.

[40] S. Yang, Z. D. Chen, Y. J. Yu, and S. Ponomarenkno, "Efficient implementation of the divergence-preserved ADI-FDTD method," *IEEE Antennas and Wireless Propagation Letters,* vol. 11, pp. 1560-1563, 2012.

[41] S. Yang, Z. D. Chen, Y. Yu, and S. Ponomarenko, "On the divergence properties of the new efficiency-improved divergence preserved ADI-FDTD method," in *IEEE International Microwave Symposium*, 2013, pp. 1-3.

[42] S. Yang, Y. Yu, Z. Chen, and S. Ponomarenko, "A Time-Domain Collocation Meshless Method with Local Radial Basis Functions for Transient Analysis," *IEEE Transactions on Antennas and Propagation,* vol. 62, pp. 5334 - 5338, 2014.

[43] Z. D. Chen, S. Yang, and Y. Yu, "How can we unify numerical methods with a single mathematic framework?," in *Antennas and Propagation (APCAP), 2014 3rd Asia-Pacific Conference on*, 2014, pp. 1392-1395.

[44] S. Yang, Z. Chen, Y. Yu, and S. Ponomarenko, "A divergence-free meshless method based on the vector basis function for transient electromagnetic analysis," *IEEE Transactions on Microwave Theory and Techniques,* vol. 62, pp. 1409 - 1416, 2014.

[45] S. Yang, Z. Chen, Y. Yu, and S. Ponomarenko, "On the Numerical Dispersion of the Radial Point Interpolation Meshless Method," *IEEE Microwave and Wireless Components Letters,* vol. 24, pp. 653 - 655, 2014.

[46] S. Yang, Z. David Chen, Y. J. Yu, and S. Ponomarenko, "A vector-based divergence-free meshless method," in *Antenna Technology and Applied Electromagnetics (ANTEM), 2014 16th International Symposium on*, 2014, pp. 1-2.

[47] S. Yang, Z. Chen, Y. Yu, and S. Ponomarenko, "A Robust Meshless Method with QR-Decomposed Radial Basis Functions," in *IEEE International Microwave Symposium*, 2015, pp. 1-3.

[48] J. Shibayama, M. Muraki, J. Yamauchi, and H. Nakano, "Efficient implicit FDTD algorithm based on locally one-dimensional scheme," *Electronics Letters,* vol. 41, pp. 1046-1047, 2005.

[49] P. Mardahl and J. Verboncoeur, "Charge conservation in electromagnetic PIC codes; spectral comparison of Boris/DADI and Langdon-Marder methods," *Computer Physics Communications,* vol. 106, pp. 219-229, 1997.

[50] C. Kraus, A. Adelmann, and P. Arbenz, "Perfectly matched layers in a divergence preserving ADI scheme for electromagnetics," *Journal of Computational Physics,* vol. 231, pp. 39-44, 2011.

[51] M. Pusa and J. Leppänen, "Computing the matrix exponential in burnup calculations," *Nuclear science and engineering,* vol. 164, pp. 140-150, 2010.

[52] W. Fu and E. L. Tan, "Stability and dispersion analysis for higher order 3-D ADI-FDTD method," *IEEE Transactions on Antennas and Propagation,* vol. 53, pp. 3691-3696, 2005.

[53] W. Lee, *Tridiagonal matrices: Thomas algorithm*. http://www3.ul.ie/wlee/ms6021_thomas.pdf, Scientific Computation, University of Limerick.

[54] A. Pereda, L. A. Vielva, A. Vegas, and A. Prieto, "Analyzing the stability of the FDTD technique by combining the von Neumann method with the Routh-Hurwitz criterion," *IEEE Transactions on Microwave Theory and Techniques,* vol. 49, pp. 377-381, 2001.

[55] T. Gan and E. Tan, "Stability and dispersion analysis for three-dimensional (3-D) leapfrog ADI-FDTD method," *Progress In Electromagnetics Research M,* vol. 23, pp. 1-12, 2012.

[56] B. Donderici and F. L. Teixeira, "Symmetric source implementation for the ADI-FDTD method," *IEEE Transactions on Antennas and Propagation,* vol. 53, pp. 1562-1565, 2005.

[57] E. L. Tan, "Fundamental schemes for efficient unconditionally stable implicit finite-difference time-domain methods," *IEEE Transactions on Antennas and Propagation,* vol. 56, pp. 170-177, 2008.

[58] S. C. Yang, Z. Chen, Y. Yu, and W. Y. Yin, "The unconditionally stable one-step leapfrog ADI-FDTD method and its comparisons with other FDTD methods," *IEEE Microwave and Wireless Components Letters,* vol. 21, pp. 640-642, 2011.

[59] J.-F. Lee, R. Lee, and A. Cangellaris, "Time-domain finite-element methods," *IEEE Transactions on Antennas and Propagation,* vol. 45, pp. 430-442, 1997.

[60] J. M. Rius, E. Ubeda, and J. Parrón, "On the testing of the magnetic field integral equation with RWG basis functions in method of moments," *IEEE Transactions on Antennas and Propagation,* vol. 49, pp. 1550-1553, 2001.

[61] V. Cingoski, N. Miyamoto, and H. Yamashita, "Element-free Galerkin method for electromagnetic field computations," *IEEE Transactions on Magnetics,* vol. 34, pp. 3236-3239, 1998.

[62] S. A. Viana and R. C. Mesquita, "Moving least square reproducing kernel method for electromagnetic field computation," *IEEE Transactions on Magnetics,* vol. 35, pp. 1372-1375, 1999.

[63] T. Kaufmann, Y. Yu, C. Engström, Z. Chen, and C. Fumeaux, "Recent developments of the meshless radial point interpolation method for time‐domain electromagnetics," *International Journal of Numerical Modelling: Electronic Networks, Devices and Fields,* vol. 25, pp. 468-489, 2012.

[64] A. Cangellaris, C.-C. Lin, and K. Mei, "Point-matched time domain finite element methods for electromagnetic radiation and scattering," *IEEE Transactions on Antennas and Propagation,* vol. 35, pp. 1160-1173, 1987.

[65] J. Wang and G. Liu, "A point interpolation meshless method based on radial basis functions," *International Journal for Numerical Methods in Engineering,* vol. 54, pp. 1623-1648, 2002.

[66] Y. Yu and Z. Chen, "Implementation of material interface conditions in the radial point interpolation meshless method," *IEEE Transactions on Antennas and Propagation,* vol. 59, pp. 2916-2923, 2011.

[67] D. Jiao and J.-M. Jin, "A general approach for the stability analysis of the time-domain finite-element method for electromagnetic simulations," *IEEE Transactions on Antennas and Propagation,* vol. 50, pp. 1624-1632, 2002.

[68] S. Lowitzsch, "Approximation and Interpolation Employing Divergence-free Radial Basis Functions with Applications," Ph. D. dissertation, Texas A&M University, 2002.

[69] C. P. McNally, "Divergence‐free interpolation of vector fields from point values–exact $\nabla \cdot B = 0$ in numerical simulations," *Monthly Notices of the Royal Astronomical Society: Letters,* vol. 413, pp. L76-L80, 2011.

[70] E. J. Kansa, "Multiquadrics—a scattered data approximation scheme with applications to computational fluid-dynamics—I surface approximations and partial derivative estimates," *Computers & Mathematics with applications,* vol. 19, pp. 127-145, 1990.

[71] E. J. Kansa, "Multiquadrics—A scattered data approximation scheme with applications to computational fluid-dynamics—II solutions to parabolic, hyperbolic and elliptic partial differential equations," *Computers & Mathematics with Applications,* vol. 19, pp. 147-161, 1990.

[72] I. J. Schoenberg, "Metric spaces and completely monotone functions," *The Annals of Mathematics,* vol. 39, pp. 811-841, 1938.

[73] Z. Chen and M. M. Ney, "The method of weighted residuals: A general approach to deriving time-and frequency-domain numerical methods," *IEEE Antennas and Propagation Magazine,* vol. 51, pp. 51-70, 2009.

[74] J.-M. Jin, *The finite element method in electromagnetics*: Wiley New York, 2002.

[75] R. F. Harrington and J. L. Harrington, *Field computation by moment methods*: Oxford University Press, 1996.

[76] Z. Chen and S. Luo, "Generalization of the finite-difference-based time-domain methods using the method of moments," *IEEE Transactions on Antennas and Propagation,* vol. 54, pp. 2515-2524, 2006.

Appendix A: Derivation and Full Formulations for the Divergence Preserved ADI-FDTD Method

For the *n*th to *n+1/2*th time step for the divergence preserved ADI-FDTD method, we can have the following fomulations.

Extension of (2.9a) and (2.9b) reads as

$$Q_{ex}^{n+1/2} = E_x^n - \frac{c\Delta t}{2}\partial z Q_{hy}^{n+1/2} \tag{A1a}$$

$$Q_{ey}^{n+1/2} = E_y^n - \frac{c\Delta t}{2}\partial x Q_{hz}^{n+1/2} \tag{A1b}$$

$$Q_{ez}^{n+1/2} = E_z^n - \frac{c\Delta t}{2}\partial y Q_{hx}^{n+1/2} \tag{A1c}$$

$$Q_{hx}^{n+1/2} = \mathrm{Z}_0 H_x^n - \frac{c\Delta t}{2}\partial y Q_{ez}^{n+1/2} \tag{A1d}$$

$$Q_{hy}^{n+1/2} = \mathrm{Z}_0 H_y^n - \frac{c\Delta t}{2}\partial z Q_{ex}^{n+1/2} \tag{A1e}$$

$$Q_{hz}^{n+1/2} = \mathrm{Z}_0 H_z^n - \frac{c\Delta t}{2}\partial x Q_{ey}^{n+1/2}, \tag{A1f}$$

$$E_x^{n+1/2} = Q_{ex}^{n+1/2} + \frac{c\Delta t}{2}\partial y Q_{hz}^{n+1/2} \tag{A2a}$$

$$E_y^{n+1/2} = Q_{ey}^{n+1/2} + \frac{c\Delta t}{2}\partial z Q_{hx}^{n+1/2} \tag{A2d}$$

$$E_z^{n+1/2} = Q_{ez}^{n+1/2} + \frac{c\Delta t}{2}\partial x Q_{hy}^{n+1/2} \tag{A2e}$$

$$H_x^{n+1/2} = \frac{1}{\mathrm{Z}_0} Q_{hx}^{n+1/2} + \frac{c\Delta t}{2\mathrm{Z}_0}\partial z Q_{ey}^{n+1/2} \tag{A2f}$$

$$H_y^{n+1/2} = \frac{1}{\mathrm{Z}_0} Q_{hy}^{n+1/2} + \frac{c\Delta t}{2\mathrm{Z}_0}\partial x Q_{ez}^{n+1/2} \tag{A2e}$$

$$H_z^{n+1/2} = \frac{1}{\mathrm{Z}_0} Q_{hz}^{n+1/2} + \frac{c\Delta t}{2\mathrm{Z}_0}\partial y Q_{ex}^{n+1/2}, \tag{A2f}$$

$$H_z^{n+1} = \frac{1}{\mathrm{Z}_0} Q_{hz}^{n+1} - \frac{c\Delta t}{2\mathrm{Z}_0}\partial x Q_{ey}^{n+1}. \tag{A4f}$$

By replacing the spatial partial operators in (A1) – (A2) with the second order central finite-

difference, we can get the final time-marching formulations as

$$\left[1+\frac{\Delta t^2}{2\mu\varepsilon\Delta z^2}\right]Q_{ex(i+1/2,j,k)}^{n+1/2}-\frac{\Delta t^2}{4\mu\varepsilon\Delta z^2}Q_{ex(i+1/2,j,k+1)}^{n+1/2}-\frac{\Delta t^2}{4\mu\varepsilon\Delta z^2}Q_{ex(i+1/2,j,k-1)}^{n+1/2}=E_{x(i+1/2,j,k)}^{n}$$
$$-\frac{\Delta t}{2\varepsilon\Delta z}\left(H_{y(i+1/2,j,k+1/2)}^{n}-H_{y(i+1/2,j,k-1/2)}^{n}\right) \tag{A3a}$$

$$\left[1+\frac{\Delta t^2}{2\mu\varepsilon\Delta x^2}\right]Q_{ey(i,j+1/2,k)}^{n+1/2}-\frac{\Delta t^2}{4\mu\varepsilon\Delta x^2}Q_{ey(i+1,j+1/2,k)}^{n+1/2}-\frac{\Delta t^2}{4\mu\varepsilon\Delta x^2}Q_{ey(i-1,j+1/2,k)}^{n+1/2}=E_{y(i,j+1/2,k)}^{n}$$
$$-\frac{\Delta t}{2\varepsilon\Delta x}\left(H_{z(i+1/2,j+1/2,k)}^{n}-H_{z(i-1/2,j+1/2,k)}^{n}\right) \tag{A3b}$$

$$\left[1+\frac{\Delta t^2}{2\mu\varepsilon\Delta y^2}\right]Q_{ez(i,j,k+1/2)}^{n+1/2}-\frac{\Delta t^2}{4\mu\varepsilon\Delta y^2}Q_{ez(i,j+1,k+1/2)}^{n+1/2}-\frac{\Delta t^2}{4\mu\varepsilon\Delta y^2}Q_{ez(i,j-1,k+1/2)}^{n+1/2}=E_{z(i,j,k+1/2)}^{n}$$
$$-\frac{\Delta t}{2\varepsilon\Delta y}\left(H_{x(i,j+1/2,k+1/2)}^{n}-H_{x(i,j-1/2,k+1/2)}^{n}\right) \tag{A3c}$$

$$Q_{hx(i,j+1/2,k+1/2)}^{n+1/2}=Z_0H_{x(i,j+1/2,k+1/2)}^{n}-\frac{c\Delta t}{2\Delta y}\left(Q_{ez(i,j+1,k+1/2)}^{n+1/2}-Q_{ez(i,j,k+1/2)}^{n+1/2}\right) \tag{A3d}$$

$$Q_{hy(i+1/2,j,k+1/2)}^{n+1/2}=Z_0H_{y(i+1/2,j,k+1/2)}^{n}-\frac{c\Delta t}{2\Delta z}\left(Q_{ex(i+1/2,j,k+1)}^{n+1/2}-Q_{ex(i+1/2,j,k)}^{n+1/2}\right) \tag{A3e}$$

$$Q_{hz(i+1/2,j+1/2,k)}^{n+1/2}=Z_0H_{z(i+1/2,j+1/2,k)}^{n}-\frac{c\Delta t}{2\Delta x}\left(Q_{ey(i+1,j+1/2,k)}^{n+1/2}-Q_{ey(i,j+1/2,k)}^{n+1/2}\right), \tag{A3f}$$

$$E_{x(i+1/2,j,k)}^{n+1/2}=Q_{ex(i+1/2,j,k)}^{n+1/2}+\frac{c\Delta t}{2\Delta y}\left(Q_{hz(i+1/2,j+1/2,k)}^{n+1/2}-Q_{hz(i+1/2,j-1/2,k)}^{n+1/2}\right) \tag{A4a}$$

$$E_{y(i,j+1/2,k)}^{n+1/2}=Q_{ey(i,j+1/2,k)}^{n+1/2}+\frac{c\Delta t}{2\Delta z}\left(Q_{hx(i,j+1/2,k+1/2)}^{n+1/2}-Q_{hx(i,j+1/2,k-1/2)}^{n+1/2}\right) \tag{A4b}$$

$$E_{z(i,j,k+1/2)}^{n+1/2}=Q_{ez(i,j,k+1/2)}^{n+1/2}+\frac{c\Delta t}{2\Delta x}\left(Q_{hy(i+1/2,j,k+1/2)}^{n+1/2}-Q_{hy(i-1/2,j,k+1/2)}^{n+1/2}\right) \tag{A4c}$$

$$H_{x(i,j+1/2,k+1/2)}^{n+1/2}=\frac{1}{Z_0}Q_{hx(i,j+1/2,k+1/2)}^{n+1/2}+\frac{\Delta t}{2\mu\Delta z}\left(Q_{ey(i,j+1/2,k+1)}^{n+1/2}-Q_{ey(i,j+1/2,k)}^{n+1/2}\right) \tag{A4d}$$

$$H_{y(i+1/2,j,k+1/2)}^{n+1/2}=\frac{1}{Z_0}Q_{hy(i+1/2,j,k+1/2)}^{n+1/2}+\frac{\Delta t}{2\mu\Delta x}\left(Q_{ez(i+1,j,k+1/2)}^{n+1/2}-Q_{ez(i,j,k+1/2)}^{n+1/2}\right) \tag{A4e}$$

$$H_{z(i+1/2,j+1/2,k)}^{n+1/2}=\frac{1}{Z_0}Q_{hz(i+1/2,j+1/2,k)}^{n+1/2}+\frac{\Delta t}{2\mu\Delta y}\left(Q_{ex(i+1/2,j+1,k)}^{n+1/2}-Q_{ex(i+1/2,j,k)}^{n+1/2}\right), \tag{A4f}$$

For the n+1/2th to n+1 time step, with similar manner above we can have the following updating formulations for (2.10a) and (2.10b).

$$Q_{ex}^{n+1}=E_x^{n+1/2}+\frac{c\Delta t}{2}\partial yQ_{hz}^{n+1} \tag{A5a}$$

$$Q_{ey}^{n+1}=E_y^{n+1/2}+\frac{c\Delta t}{2}\partial zQ_{hx}^{n+1} \tag{A5b}$$

$$Q_{ez}^{n+1} = E_z^{n+1/2} + \frac{c\Delta t}{2}\partial x Q_{hy}^{n+1} \tag{A5c}$$

$$Q_{hx}^{n+1} = \mathrm{Z}_0 H_x^{n+1/2} + \frac{c\Delta t}{2}\partial z Q_{ey}^{n+1} \tag{A5d}$$

$$Q_{hy}^{n+1} = \mathrm{Z}_0 H_y^{n+1/2} + \frac{c\Delta t}{2}\partial x Q_{ez}^{n+1} \tag{A5e}$$

$$Q_{hz}^{n+1} = \mathrm{Z}_0 H_z^{n+1/2} + \frac{c\Delta t}{2}\partial y Q_{ex}^{n+1}, \tag{A5f}$$

and

$$E_x^{n+1} = Q_{ex}^{n+1} - \frac{c\Delta t}{2}\partial z Q_{hy}^{n+1} \tag{A6a}$$

$$E_y^{n+1} = Q_{ey}^{n+1} - \frac{c\Delta t}{2}\partial x Q_{hz}^{n+1} \tag{A6b}$$

$$E_z^{n+1} = Q_{ez}^{n+1} - \frac{c\Delta t}{2}\partial y Q_{hx}^{n+1} \tag{A6c}$$

$$H_x^{n+1} = \frac{1}{\mathrm{Z}_0} Q_{hx}^{n+1} - \frac{c\Delta t}{2\mathrm{Z}_0}\partial y Q_{ez}^{n+1} \tag{A6d}$$

$$H_y^{n+1} = \frac{1}{\mathrm{Z}_0} Q_{hy}^{n+1} - \frac{c\Delta t}{2\mathrm{Z}_0}\partial z Q_{ex}^{n+1} \tag{A6e}$$

Then, the final updating equations for the second sub-time step can be achieved as

$$\left[1+\frac{\Delta t^2}{2\mu\varepsilon\Delta y^2}\right]Q_{ex(i+1/2,j,k)}^{n+1} - \frac{\Delta t^2}{4\mu\varepsilon\Delta y^2}Q_{ex(i+1/2,j+1,k)}^{n+1} - \frac{\Delta t^2}{4\mu\varepsilon\Delta y^2}Q_{ex(i+1/2,j-1,k)}^{n+1} = E_{x(i+1/2,j,k)}^{n+1/2} + \frac{\Delta t}{2\varepsilon\Delta y}\left(H_{z(i+1/2,j+1/2,k)}^{n+1/2} - H_{z(i+1/2,j-1/2,k)}^{n+1/2}\right) \tag{A7a}$$

$$\left[1+\frac{\Delta t^2}{2\mu\varepsilon\Delta z^2}\right]Q_{ey(i,j+1/2,k)}^{n+1} - \frac{\Delta t^2}{4\mu\varepsilon\Delta z^2}Q_{ey(i,j+1/2,k+1)}^{n+1} - \frac{\Delta t^2}{4\mu\varepsilon\Delta z^2}Q_{ey(i,j+1/2,k-1)}^{n+1} = E_{y(i,j+1/2,k)}^{n+1/2} + \frac{\Delta t}{2\varepsilon\Delta z}\left(H_{x(i,j+1/2,k+1/2)}^{n+1/2} - H_{x(i,j+1/2,k-1/2)}^{n+1/2}\right) \tag{A7b}$$

$$\left[1+\frac{\Delta t^2}{2\mu\varepsilon\Delta x^2}\right]Q_{ez(i,j,k+1/2)}^{n+1/2} - \frac{\Delta t^2}{4\mu\varepsilon\Delta x^2}Q_{ez(i+1,j,k+1/2)}^{n+1/2} - \frac{\Delta t^2}{4\mu\varepsilon\Delta x^2}Q_{ez(i-1,j,k+1/2)}^{n+1/2} = E_{z(i,j,k+1/2)}^{n+1/2} + \frac{\Delta t}{2\varepsilon\Delta x}\left(H_{y(i+1/2,j,k+1/2)}^{n+1/2} - H_{y(i-1/2,j,k+1/2)}^{n+1/2}\right) \tag{A7c}$$

$$Q_{hx(i,j+1/2,k+1/2)}^{n+1} = \mathrm{Z}_0 H_{x(i,j+1/2,k+1/2)}^{n+1/2} + \frac{c\Delta t}{2\Delta z}\left(Q_{ey(i,j+1/2,k+1)}^{n+1} - Q_{ey(i,j+1/2,k)}^{n+1}\right) \tag{A7d}$$

$$Q_{hy(i+1/2,j,k+1/2)}^{n+1} = \mathrm{Z}_0 H_{y(i+1/2,j,k+1/2)}^{n+1/2} + \frac{c\Delta t}{2\Delta x}\left(Q_{ez(i+1,j,k+1/2)}^{n+1} - Q_{ez(i,j,k+1/2)}^{n+1}\right) \tag{A7e}$$

$$Q_{hz(i+1/2,j+1/2,k)}^{n+1} = Z_0 H_{z(i+1/2,j+1/2,k)}^{n+1/2} + \frac{c\Delta t}{2\Delta y}\left(Q_{ex(i+1/2,j+1,k)}^{n+1} - Q_{ex(i+1/2,j,k)}^{n+1}\right). \tag{A7f}$$

Then, with replacement the second-order spatial finite-difference, the final marching formulations can be read as

$$E_{x(i+1/2,j,k)}^{n+1} = Q_{ex(i+1/2,j,k)}^{n+1} - \frac{c\Delta t}{2\Delta z}\left(Q_{hy(i+1/2,j,k+1/2)}^{n+1} - Q_{hy(i+1/2,j,k-1/2)}^{n+1}\right) \tag{A8a}$$

$$E_{y(i,j+1/2,k)}^{n+1} = Q_{ey(i,j+1/2,k)}^{n+1} - \frac{c\Delta t}{2\Delta x}\left(Q_{hz(i+1/2,j+1/2,k)}^{n+1} - Q_{hz(i-1/2,j+1/2,k)}^{n+1}\right) \tag{A8b}$$

$$E_{z(i,j,k+1/2)}^{n+1} = Q_{ez(i,j,k+1/2)}^{n+1} - \frac{c\Delta t}{2\Delta y}\left(Q_{hx(i,j+1/2,k+1/2)}^{n+1} - Q_{hx(i,j-1/2,k+1/2)}^{n+1}\right) \tag{A8c}$$

$$H_{x(i,j+1/2,k+1/2)}^{n+1} = \frac{1}{Z_0} Q_{hx(i,j+1/2,k+1/2)}^{n+1} - \frac{\Delta t}{2\mu\Delta y}\left(Q_{ez(i,j+1,k+1/2)}^{n+1} - Q_{ez(i,j,k+1/2)}^{n+1}\right) \tag{A8d}$$

$$H_{y(i+1/2,j,k+1/2)}^{n+1} = \frac{1}{Z_0} Q_{hy(i+1/2,j,k+1/2)}^{n+1} - \frac{\Delta t}{2\mu\Delta z}\left(Q_{ex(i+1/2,j,k+1)}^{n+1} - Q_{ex(i+1/2,j,k)}^{n+1}\right) \tag{A8e}$$

$$H_{z(i+1/2,j+1/2,k)}^{n+1} = \frac{1}{Z_0} Q_{hz(i+1/2,j+1/2,k)}^{n+1} - \frac{\Delta t}{2\mu\Delta x}\left(Q_{ey(i+1,j+1/2,k)}^{n+1} - Q_{ex(i,j+1/2,k)}^{n+1}\right) \tag{A8f}$$

Appendix B: Copyright Permissions

B.1 Permission from IEEE TAP

From: Shunchuan Yang
Sent: Tuesday, May 12, 2015 10:17 AM
To: pubs-permissions@ieee.org
Subject: Copyright Permission

Dear IEEE,

I am the first author of the following papers while I was working toward my PhD degree. Now, I am preparing my PhD thesis for submission to the Faculty of Graduate Studies at Dalhousie University, Halifax, Nova Scotia, Canada. I am seeking your permission to include a manuscript version of the following papers in the thesis:

1. S. Yang, Y. Yu, Z. Chen, S. Ponomarenko, "A Time-Domain Collocation Meshless Method with Local Radial Basis Functions for Transient Analysis", *IEEE Transactions on Antennas and Propagation*, vol. 62, pp. 5334-5338, Oct. 2014.
2. S. Yang, Z. Chen, Y. Yu, S. Ponomarenkno, "Efficient implementation of the divergence-preserved ADI-FDTD method", *IEEE Antennas and Wireless Propagation Letters*, vol. 11, pp. 1560-1563, Dec. 2012.

Full publication details and a copy of this permission letter will be included in my thesis. Thank you for your kind reply!

Sincerely,
Shunchuan Yang

From: Pubs Permissions <pubs-permissions+noreply@ieee.org>
Sent: Tuesday, May 12, 2015 10:17 AM
To: Shunchuan Yang

Subject: Re: Copyright Permission

Permission to reuse IEEE content, including use in a thesis or dissertation must be done through the Copyright Clearance Center's RightsLink service, using IEEE Xplore.

1. Please locate the content beginning at http://ieeexplore.ieee.org/Xplore/home.jsp
2. Once on the abstract page of the article, please locate the "Request Permission" link in the left navigation panel
3. You can also find the copyright symbol directly on the article Table of Content
4. If you find there are none of these links, you should open the free front pages of the content to determine if there is another rights holder, as this is an indication IEEE is not the intellectual property rights holder, and we cannot grant permission for reuse
5. If the links are there, please do choose one of them and this will take you to the permission application page

If you do experience difficulty. please contact customer service at customercare@copyright.com or M.E. Brennan atme.brennan@ieee.org.

From: M.E. Brennan <me.brennan@ieee.org>
Sent: Tuesday, May 12, 2015 3:00 PM
To: Shunchuan Yang
Cc: M.E. Brennan; Frank Pepe
Subject: Re: Copyright Permission

Dear Shunchuan Yang,

The IEEE does not require individuals working on a thesis to obtain a formal reuse license however, you must follow the requirements listed below:

Textual Material

Using short quotes or referring to the work within these papers) users must give full credit

to the original source (author, paper, publication) followed by the IEEE copyright line © 2011 IEEE.

In the case of illustrations or tabular material, we require that the copyright line © [Year of original publication] IEEE appear prominently with each reprinted figure and/or table.
If a substantial portion of the original paper is to be used, and if you are not the senior author, also obtain the senior author's approval.

Full-Text Article

If you are using the entire IEEE copyright owned article, the following IEEE copyright/ credit notice should be placed prominently in the references: © [year of original publication] IEEE. Reprinted, with permission, from [author names, paper title, IEEE publication title, and month/year of publication]

Only the **accepted** version of an IEEE copyrighted paper can be used in your dissertation or when posting the paper or your thesis on-line. You may not use the **final published** version. In placing the thesis on the author's university website, please display the following message in a prominent place on the website: In reference to IEEE copyrighted material which is used with permission in this thesis, the IEEE does not endorse any of [university/educational entity's name goes here]'s products or services. Internal or personal use of this material is permitted. If interested in reprinting/republishing IEEE copyrighted material for advertising or promotional purposes or for creating new collective works for resale or redistribution, please go to http://www.ieee.org/publications_standards /publications/rights/rights_link.html to learn how to obtain a License from RightsLink.

If applicable, University Microfilms and/or ProQuest Library, or the Archives of Canada may supply single copies of the dissertation.

The above message also appears if you go to RightsLink from your paper in Xplore and choose reuse in dissertation from the drop down menu.

Good luck with your thesis.
Kind regards,

M.E. Brennan

Ms M.E. Brennan
IEEE
501 Hoes Lane
Piscataway, NJ 08854-4141 USA
me.brennan@ieee.org

+1 (732) 562-2660

B.2 Permission from IEEE TMTT

From: Shunchuan Yang
Sent: Monday, May 11, 2015 4:54 PM
To: e.niehenke@ieee.org
Subject: Copyright Permission

Dear IEEE Microwave Theory and Techniques Society,

I am the first author of the following papers while I was working toward my PhD degree. Now, I am preparing my PhD thesis for submission to the Faculty of Graduate Studies at Dalhousie University, Halifax, Nova Scotia, Canada. I am seeking your permission to include a manuscript version of the following papers in the thesis:

1. S. Yang, Z. Chen, Y. Yu, S. Ponomarenko, "A Divergence-Free Meshless Method Based on the Vector Basis Function for Transient Electromagnetic Analysis", *IEEE Transactions on Microwave Theory and Techniques*, vol. 62, pp. 1409-1416, 2014.
2. S. Yang, Z. Chen, Y. Yu, S. Ponomarenko, "On the Numerical Dispersion of the Radial Point Interpolation Meshless Method", *IEEE Microwave and Wireless Components Letters,* vol. 24, no. 10, pp. 653-655, Oct. 2014.
3. S. Yang, Z. Chen, Y. Yu, S. Ponomarenko, "A Robust Meshless Method with QR-Decomposed Radial Basis Functions", *IEEE International Microwave Symposium (IMS)*, May 2015.
4. S. Yang, Z. Chen, Y. Yu, S. Ponomarenko, "On the divergence properties of the new efficiency-improved divergence preserved ADI-FDTD method", *IEEE International Microwave Symposium (IMS)*, June, 2013.

Full publication details and a copy of this permission letter will be included in my thesis. Thank you for your kind reply!

Sincerely,

Shunchuan Yang

From: Eniehenke@aol.com <Eniehenke@aol.com>
Sent: Tuesday, May 12, 2015 3:16 PM
To: Shunchuan Yang
Cc: george.ponchak@ieee.org
Subject: Note from Ed Niehenke Re: Copyright Permission

Dear Shunchuan Yang,

Thanks so much for your inquiry about using your IEEE published papers in your thesis that you are preparing.

I called up IEEE and you most certainly use previous IEEE papers that you wrote in your thesis.

The IEEE does not require individuals working on a thesis to obtain a formal reuse license. Please go to www.ieee.org then IEEEE Digital library, Now enter one of your papers in the search box. After it come up click it and when appears click on "Request permission" on the left hand side

Answer the question

Select use in thesis. Now the form comes up which gives you permission. Print it out and scan in to your theses for proof that it is OK to use.
Follow the procedure below as required by IEEE

Best regards,

MTT-S Ombuds Officer

Title: On the divergence properties of the new efficiency-improved divergence preserved ADI-FDTD method

Conference Proceedings: Microwave Symposium Digest (IMS), 2013 IEEE MTT-S International

Author: Shunchuan Yang; Chen, Z.D.; Yiqiang Yu; Ponomarenko, S.

Publisher: IEEE

Date: 2-7 June 2013

Thesis / Dissertation Reuse

The IEEE does not require individuals working on a thesis to obtain a formal reuse license, however, you may print out this statement to be used as a permission grant:

Requirements to be followed when using any portion (e.g., figure, graph, table, or textual material) of an IEEE copyrighted paper in a thesis:

1) In the case of textual material (e.g., using short quotes or referring to the work within these papers) users must give full credit to the original source (author, paper, publication) followed by the IEEE copyright line © 2011 IEEE.
2) In the case of illustrations or tabular material, we require that the copyright line © [Year of original publication] IEEE appear prominently with each reprinted figure and/or table.
3) If a substantial portion of the original paper is to be used, and if you are not the senior author, also obtain the senior author's approval.

Requirements to be followed when using an entire IEEE copyrighted paper in a thesis:

1) The following IEEE copyright/ credit notice should be placed prominently in the references: © [year of original publication] IEEE. Reprinted, with permission, from [author names, paper title, IEEE publication title, and month/year of publication]
2) Only the accepted version of an IEEE copyrighted paper can be used when posting the paper or your thesis on-line.
3) In placing the thesis on the author's university website, please display the following message in a prominent place on the website: In reference to IEEE copyrighted material which is used with permission in this thesis, the IEEE does not endorse any of [university/educational entity's name goes here]'s products or services. Internal or personal use of this material is permitted. If interested in reprinting/republishing IEEE copyrighted material for advertising or promotional purposes or for creating new collective works for resale or redistribution, please go to http://www.ieee.org/publications_standards/publications/rights/rights_link.html to learn how to obtain a License from RightsLink.

If applicable, University Microfilms and/or ProQuest Library, or the Archives of Canada may supply single copies of the dissertation.

Title: On the Numerical Dispersion of the Radial Point Interpolation Meshless Method

Author: Shunchuan Yang; Zhizhang Chen; Yiqiang Yu; Ponomarenko, S.

Publication: IEEE Microwave and Wireless Components Letters

Publisher: IEEE

Date: Oct. 2014

Thesis / Dissertation Reuse

The IEEE does not require individuals working on a thesis to obtain a formal reuse license, however, you may print out this statement to be used as a permission grant:

Requirements to be followed when using any portion (e.g., figure, graph, table, or textual material) of an IEEE copyrighted paper in a thesis:

1) In the case of textual material (e.g., using short quotes or referring to the work within these papers) users must give full credit to the original source (author, paper, publication) followed by the IEEE copyright line © 2011 IEEE.
2) In the case of illustrations or tabular material, we require that the copyright line © [Year of original publication] IEEE appear prominently with each reprinted figure and/or table.
3) If a substantial portion of the original paper is to be used, and if you are not the senior author, also obtain the senior author's approval.

Requirements to be followed when using an entire IEEE copyrighted paper in a thesis:

1) The following IEEE copyright/ credit notice should be placed prominently in the references: © [year of original publication] IEEE. Reprinted, with permission, from [author names, paper title, IEEE publication title, and month/year of publication]
2) Only the accepted version of an IEEE copyrighted paper can be used when posting the paper or your thesis on-line.
3) In placing the thesis on the author's university website, please display the following message in a prominent place on the website: In reference to IEEE copyrighted material which is used with permission in this thesis, the IEEE does not endorse any of [university/educational entity's name goes here]'s products or services. Internal or personal use of this material is permitted. If interested in reprinting/republishing IEEE copyrighted material for advertising or promotional purposes or for creating new collective works for resale or redistribution, please go to http://www.ieee.org/publications_standards/publications/rights/rights_link.html to learn how to obtain a License from RightsLink.

If applicable, University Microfilms and/or ProQuest Library, or the Archives of Canada may supply single copies of the dissertation.